Diplomarbeit

Suitability of Water as a Blood Model for the Quantitative Determination of the CO_2 Separation Rate of Membrane Oxygenators

ausgeführt zum Zwecke der Erlangung des akademischen Grades eines

Diplom-Ingenieurs

unter der Leitung von

Ao.Univ.Prof. Dipl.-Ing. Dr.techn. Michael Harasek

(E166 - Inst. f. Verfahrenstechnik, Umwelttechnik und Techn. Biowissenschaften, TU Wien)

Dipl.-Ing. Benjamin Lukitsch

(E166 - Inst. f. Verfahrenstechnik, Umwelttechnik und Techn. Biowissenschaften, TU Wien)

eingereicht an der Technischen Universität Wien

Fakultät für Technische Chemie

von

Raffael Koller

01354154 (066473)

Florianigasse 14/14

1080 Wien

Wien, im März 2021

Raffael Koller

Ich habe zur Kenntnis genommen, dass ich zur Drucklegung meiner Arbeit unter der Bezeichnung

Diplomarbeit

Nur mit Bewilligung der Prüfungskommission berechtigt bin.

Ich erkläre weiteren Eides statt, dass ich meine Diplomarbeit nach den anerkannten Grundsätzen für wissenschaftliche Abhandlungen selbstständig ausgeführt habe und alle verwendeten Hilfsmittel, insbesondere die zugrunde gelegte Literatur, genannt habe.

Weiters erkläre ich, dass ich dieses Diplomarbeitsthema bisher weder im In- noch im Ausland (einer Beurteilerin/einem Beurteiler zur Begutachtung) in irgendeiner Form als Prüfungsarbeit vorgelegt habe und dass diese Arbeit mit der vom Begutachter beurteilten Arbeit übereinstimmt.

Wien, im März 2021

Raffael Koller

Kurzfassung

Wasser ist aufgrund seiner einfachen Handhabung ein gängiger Blutersatz zur Bestimmung der CO_2 Abtrennleistung von künstlichen Lungen, sogenannten Oxygenatoren.

Im Rahmen dieser Masterarbeit wurden in vivo Tests mit Schweineblut in Form von in vitro Tests mit Wasser wiederholt. In beiden Versuchskampagnen wurde die CO_2 Abtrennleistung eines Oxygenatorprototypen bestimmt. Es konnte gezeigt werden, dass Wasser trotz einer geringeren CO_2 Bindungskapazität und einer niedrigeren Viskosität ähnliche CO_2 Abfuhrraten wie Blut aufweist.

Um den Einfluss der Bindungskapazität sowie der Viskosität auf die Konzentrationspolarisation in der Grenzschicht zu untersuchen wurden numerische Strömungssimulationen (engl.: Computational Fluid Dynamics (CFD) Simualtions) durchgeführt. Die Konzentrationspolarisation welche blutseitig an der Membranoberfläche auftritt ist dabei von besonderem Interesse. Sie kann als der dominierende Widerstand für die CO_2 Abtransport angesehen werden. Die CFD Simulationen welche mit dem Open-Source Programm OpenFOAM® und dem hausintern entwickelten Solver membraneFOAM durchgeführt wurden, erlauben dabei eine Bestimmung der Dicke der Konzentrationspolarisation sowie der CO_2 Abfuhrrate.

Die CO_2 Abfuhrrate lässt sich darüber hinaus auch durch Sherwood-Korrelationen bestimmen. In Zuge dieser Arbeit wurden die empirischen Parameter einer Sherwood-Korrelation bestimmt. Hierfür wurde die in vitro mit Wasser bestimmte CO_2 Abtrennleistung des Oxygenatorprototypen herangezogen. Des Weiteren wird eine Methode evaluiert, welche die Umrechnung des Transportwiderstandes und somit der CO_2 Abtrennleistung mit Wasser zu jener mit Blut erlaubt. Die Umrechnung wird durch eine geeignete Anpassung der Materialparameter in der Reynolds- und Schmidtzahl, welche in der Sherwood-Korrelation enthalten sind, vorgenommen.

Abstract

In the context of this master thesis in vivo tests with porcine blood were repeated in the form of in vitro tests with water. In both test campaigns the CO_2 separation efficiency of an oxygenator prototype was determined. It could be shown that water has similar CO_2 removal rates as blood despite lower CO_2 binding capacity and lower viscosity.

Computational Fluid Dynamics (CFD) simulations were performed to investigate the influence of the binding capacity and viscosity on the concentration polarization in the boundary layer. The concentration polarization which occurs on the blood side of the membrane surface is of particular interest. It is the limiting factor and dominant resistance for the CO_2 separation rate. The CFD simulations performed with the open-source program OpenFOAM® and the in-house developed solver membraneFOAM allow to determine the thickness of the concentration polarization and the CO_2 removal rate.

The CO_2 removal rate can also be determined by Sherwood correlations. In this work the empirical parameters of a Sherwood correlation were determined. For this purpose, the CO_2 removal rate of the oxygenator prototype determined in vitro with water was used. Furthermore, a method is evaluated which allows the conversion of the transport resistance and thus the CO_2 removal rate with water to that with blood. The conversion is performed by a suitable adjustment of the material parameters in the Reynolds and Schmidt numbers, which are contained in the Sherwood correlation.

Table of contents

List of symbols

Some units used in this thesis are typical for medical equipment technology and are not SI units. They were chosen for easier comparability between this work and literature.

Symbol	Description	Unit
A_{inlet}	boundary area of reduced geometry inlet	[m]
A_M	membrane surface area	[m]
$A_{membrane,complete\ geoemtry}$	membrane surface area of the complete geometry	[m]

$A_{membrane,reduced\ geoemtry}$	membrane surface area of the reduced geometry	[m]
$A_{spacing}$	cross section between two fibers	[m]
a	geometry parameter for the Sherwood model	[-]
a_b	geometry parameter of blood	[-]
a_w	geometry parameter of water	[-]
a_v	surface area per volume of the prototype	[m²/m³]
b	geometry parameter for the Sherwood model	[-]
b_b	geometry parameter of blood	[-]
b_w	geometry parameter of water	[-]
C_{CO_2}	concentration of carbon dioxide	[vol%]
C_{HCO_3}	concentration of bicarbonate	[vol%]
$C_{i,M}$	concentration of the specie i in the membrane	[vol%]
D_{CO_2}	diffusion coefficient of CO_2 in blood	[m²/s]
$D_{CO_2,total}$	total diffusion coefficient of CO_2 in blood	[m²/s]
$D_{CO_2\_W}$	diffusion coefficient of CO_2 in water	[m²/s]
$D_{eff\_CO_2}$	effective diffusion coefficient of CO_2 in blood	[m²/s]
D_f	facilitated diffusion coefficient of CO_2 in blood	[m²/s]

D_{HCO_3}	dissolved bicarbonate diffusion coefficient in blood	[m^2/s]
$D_{i,M}$	diffusion coefficient of specie i in the membrane	[m^2/s]
d_h	hydraulic diameter	[m]
J_{CO_2}	transmembrane transport of CO_2	[ml/min]
$J_{CO_2,complete\ geometry}$	transmembrane transport of CO_2 in the complete geometry	[ml/min]
$J_{CO_2,reduced\ geometry}$	transmembrane transport of CO_2 in the reduced geometry	[ml/min]
J_i	transmembrane transport of specie i	[ml/min]
K_c	Carman-Kozeny constant	[-]
k_B	mass transfer coefficient in blood	[m/s/mmHg]
$k_{Exp,w}$	experimental mass transfer coefficient in water	[m/s/mmHg]
k_W	mass transfer coefficient in water	[m/s/mmHg]
$k^*{}_B$	coefficient for the Sherwood model prediction	[m/s/mmHg]
L	length of a fiber in the module	[m]
ΔL	thickness of the membrane	[m]
n	power law model coefficient	[-]
P	membrane permeance	[GPU]
p_{CO_2}	partial pressure of CO_2	[mmHg]
p_{CO2in}	inlet CO_2 partial pressure	[mmHg]
p_{CO2out}	outlet CO_2 partial pressure	[mmHg]

Δp_{CO_2}	CO_2 partial pressure difference between inlet and outlet	[mmHg]
$\Delta_{log} p_{CO_2}$	logarithmic mean partial pressure difference of CO_2	[mmHg]
q	regression parameter of the CO_2 dissociation curve in blood	[-]
r_p	pore radius	[m]
t	regression parameter of the CO_2 dissociation curve in blood	[-]
u	velocity	[m/s]
u_{inlet}	reduced geometry inlet velocity	[m/s]
u_{max}	maximal velocity between two fibers	[m/s]
u_s	superficial velocity	[m/s]
$\bar{u}$	average velocity between two fibers	[m/s]
V_W	volume of water	[m^3]
$\dot{V}_{CO_2}$	CO_2 removal rate	[$ml/min/m^2$]
Sc	Schmidt number	[-]
Sc_B	Schmidt number of blood	[-]
Sc_W	Schmidt number of water	[-]
Sh	Sherwood number	[-]
Sh_B	Sherwood number of blood	[-]
Sh_W	Sherwood number of water	[-]
Re	Reynolds number	[-]
Re_B	Reynolds number of blood	[-]
Re_W	Reynolds number of water	[-]
α_{CO_2}	solubility of CO_2 in blood	[mL CO_2 STP/mL/mmHg]

$\alpha_{CO_2,W}$	Henry law constant for CO_2 in water	[mL CO_2 STP/mL/mmHg]
γ	shear rate	[1/s]
ε	porosity	[-]
λ_{CO_2}	slope of the CO_2 dissociation curve in blood	[mL CO_2 STP/mL/mmHg]
μ_0	power law model coefficient	[-]
μ_B	dynamic blood viscosity	[Pa*s]
$\mu_{chem,i}$	chemical potential of species	[J/mol]
μ_{max}	maximal dynamic blood viscosity	[Pa*s]
μ_{min}	minimal dynamic blood viscosity	[Pa*s]
μ_W	dynamic water viscosity	[Pa*s]
ν_B	kinematic blood viscosity	[m^2/s]
ν_W	kinematic water viscosity	[m^2/s]
ρ	density of the fluid	[kg/m^3]
ρ_W	density of water	[kg/m^3]

1 Introduction

Blood oxygenators, also known as artificial lungs, are needed to supplement respiratory function during cardiopulmonary bypass or to support patients with respiratory failure (Federspiel and Henchir, 2008).

Due to the large gas exchange surface and close contact between blood and gas phase, hollow-fiber membrane devices are among the most widely used blood oxygenators. In these devices, the blood flows on the shell side of the oxygenator, while pure O_2 flows through the fiber lumen. The CO_2 and O_2 transfer are driven by the partial pressure difference (Federspiel and Henchir, 2008).

The parts of the device that have contact with blood influence coagulation and platelets. Therefore, the most important optimization goals are reduction of blood contact surface while improving gas transfer rates. In addition, research focuses on reducing the priming volume by developing compact para- and intracorporal devices (Jaffer et al., 2018).

Experimental methods are important for improving blood oxygenators. Ethical guidelines and unavoidable contamination of the test circuit makes working with blood complex and expensive. Water is a suitable blood model being save, easy to handle and providing comparable gas transfer rates. Most of the research done with water is about the prediction of the gas transfer rate, or less common water loss prediction (Lawson and Holt, 2007).

While most literature is focusing on prediction of O_2 transfer, there is only limited research on CO_2 removal. Hout et al. (Hout et al., 2000) investigated the dependence of the CO_2 removal rate on the sweep flow rate. Hattler et al. (Hattler et al., 2002) tested the CO_2 and O_2 removal rate of a gas exchange catheter in vitro with water and in vivo with calves. Svitek et al. (Svitek and Federspiel, 2008a) proposed a method based on the Sherwood model that allows to predict the CO_2 removal rate with blood, using experiments with water to determine the Sherwood model geometry factors. Experiments with blood and water were performed to validate the model. The results for the removal rates between blood and water are similar but not discussed. Only the suitability of water as a blood substitute was discussed in the context of the proposed method. Tabesh et al. (Tabesh et al., 2019) determined the CO_2 removal rates of oxygenators using in vitro tests with porcine blood and water. N_2 was added to the sweep flow reducing the difference in removal rates. The maximum deviation was thus reduced to 5 %. Similarity of removal rates was not discussed. Mihelc et al. (2009) and Jeffries et al. (2014) show that removal rates of CO_2 of either in vitro experiments with water and in vivo experiments with calves are comparable, the deviation being within 10 %. The experiments were performed using an intracorporeal membrane catheter. Similarity of results is explained by the difference in viscosity and CO_2 solubility. There was no detailed discussion and investigation on the comparability of blood and water. Furthermore, the authors give no recommendation for the use of water as a blood model. Various research groups use water as a suitable blood substitute for the determination of the CO_2 removal rates, however, a detailed evaluation of water as a blood model is missing (Lukitsch et al., 2021).

This thesis focuses on how in vitro water tests could predict the CO_2 transfer rates with blood in oxygenators. There are two different approaches for the prediction of CO_2 transfer rates. Either the in vitro water data is used directly, assuming a similar CO_2 removal rate of blood and water or the in vitro water data is converted into dimensionless numbers of Sherwood models allowing a prediction of the CO_2 removal rate with blood.

The first method (direct take over) is used in several studies, however the discourse on the suitability and limitations of water is lacking (Lukitsch et al., 2021). In recent literature, assessment for the suitability of in vitro water tests rather focuses on the second method (Sherwood model conversion).

In this work in vitro experiments were carried out with a prototype blood oxygenator to determine the general suitability of water as a blood substitute, These experiments were compared and discussed with previously performed in vivo porcine blood experiments (Lukitsch et al., 2020). The experimental data was used to evaluate both methods, *direct take over* and *Sherwood model conversion*.

Furthermore, differences of the CO_2 concentration polarization layer of blood and water were studied as they pose the most significant gas transport resistance in oxygenators (Federspiel and Henchir, 2008). It is possible to observe the concentration boundary layer experimentally, but the methods are usually expensive and difficult to perform (Haddadi, 2018). Simulations are in most cases cheaper and provide data for the whole geometry

(Marriott and Sørensen, 2003). Consequently, Computational Fluid Dynamics (CFD) simulations have been performed to investigate the concentration boundary layer. OpenFOAM®, an open source program with an internally developed solver called membraneFOAM was used for the simulations and allowed to obtain the boundary layer thickness in water and blood (Haddadi, 2018).

1.1 Overview

This master thesis is divided into three parts. In the first part the necessary fundamentals are explained to understand the methods used. This part consists of chapters on membranes, blood oxygenators and CFD. In the second part, the used methods are explained. This part includes the conducted experiments, the CFD models used, and the Sherwood method proposed by Federspiel (*Sherwood model conversion*). In the last part of the thesis, the results are presented. Two different approaches for the prediction of CO_2 transfer rates, *direct take over* and *Sherwood model conversion* are compared. Furthermore, the CFD CO_2 boundary layer study is discussed.

1.2 Applied software

The results presented were obtained with the help of open-source software:

The CFD simulations were carried out using *OpenFOAM®4.1*.

The post-processing of the simulation was done with *ParaView 5.8.0*.

2 Theory

The first chapter of the theory part presents the basics of CO_2 removal in a blood Oxygenator. The prototype blood oxygenator is an artificial lung and a hollow fiber module. Blood flows on the shell side of the oxygenator while pure O_2 flows through the fiber lumen. In this process, CO_2 is transported from the blood through the membrane into the sweep gas. This is a gas permeation process. Membrane processes in general are presented first. Secondly mass transport processes through membranes are explained, as well as the simplified resistance model calculating the flux through the membrane. The general structure of hollow fiber membranes, blood oxygenators and the determinants of CO_2 gas exchange in blood oxygenator are explained thereafter. The last part explains the CO_2 solubility in water and blood.

2.1 Membrane processes

A membrane can be considered as an intermediate phase separating two homogeneous phases. It is used to control the permeation rate of chemical species. The membrane offers different resistances to the components of the homogeneous phase.

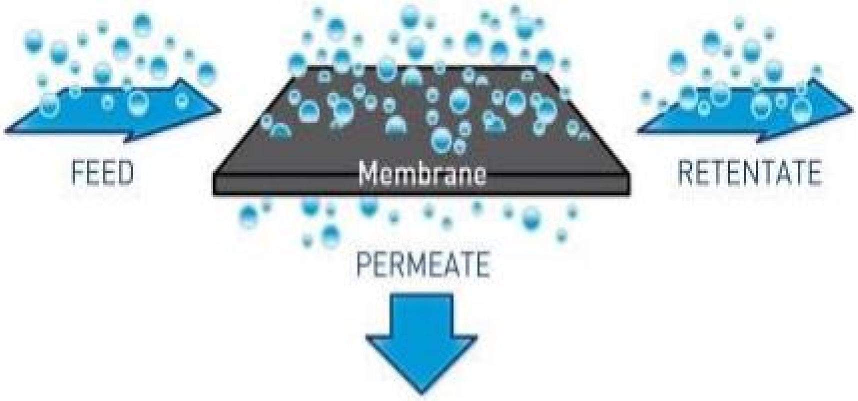

Figure 1: Basic structure of a membrane separation process. (“Pentair | X-Flow,” 2021)

The goal of a membrane separation process is to allow certain species to pass through the membrane while preventing others from doing so. The basic form of a membrane separation process is shown in Figure 1. Here, the closed unit in which the membrane is arranged is called a "module". A membrane module always requires one inlet, where the separating fluid, "feed", flows in, and two outlets, for the retained part, "retentate", and the permeate part, "permeate". Membrane separation processes are characterized according to the size of the components passed, the separation principle, the driving force and the physical state of the fluids in contact with them (Baker, 2000; Melin and Rautenbach, 2007).

While membranes are classified according to their structure, a distinction is made between porous, microporous, and non-porous. An overview of the most important separation processes is given in Table 1.

Table 1: Overview and characteristics of the most common membrane processes.

membrane process	driving force	membrane type	application area
microfiltration	partial pressure	porous	separation of suspended particles from solutions
ultrafiltration	partial pressure	micro porous	separation of dissolved macromolecules from the solvent
nanofiltration	partial pressure	micro porous	separation of dissolved substances of medium molar mass from the solvent
reverse osmosis	partial pressure	nonporous	water separation from salt or sugar solutions
dialysis	concentration	nonporous or micro porous	blood purification
electrodialysis	electric potential	nonporous or microporous	separation of ions from aqueous solutions
pervaporation	concentration	nonporous	organic solvent dewatering
gas permeation	partial pressure	nonporous	artificial lungs, exhaust air purification

Membrane processes are expected to play an important role in various fields. These include applications in environmental technology, energy-efficient separation processes, artificial organs such as lungs and kidneys, and, for example, the controlled delivery of drugs (Baker, 2000).

2.1.1 Mass transport through the membrane

To predict separation efficiency of a membrane process, knowledge about membrane and hydrodynamic properties of both separated phases are important. This is because before the component to be separated reaches the membrane surface, it must pass through the hydrodynamic boundary layer. Another hydrodynamic boundary layer must be passed after penetration of the membrane. Not only the roughness but also electrical and chemical properties have an influence on the boundary layer (Melin and Rautenbach, 2007).

Separation in membrane processes is caused by the fact that a membrane adsorbs and desorbs components differently, but these components also pass the membrane at different velocities. Therefore, components are more or less hindered by the membrane. The transport velocity depends mainly on the driving forces and the mobility in the membrane. The mobility in the membrane is called permeability and is a kinetic quantity. Driving forces can be partial pressures, temperature, concentration, or electrical forces. These forces are thermodynamic quantities and can be summarized for a component as chemical potential. The general form of the specific flux can be given:

$$J_i = P_i * grad(\mu_{chem,i}) \qquad \text{Eq. 1}$$

Where J_i is the specific flux of component i, P_i is the permeability constant, and $grad(\mu_{chem,i})$ is the grandient of the chemical potential. Depending on the medium to be separated and the density of membranes, there are different models to describe them. The gas transport process in a blood oxygenator is analogous to gas permeation. Gas molecules are separated in the process. The presented protype in this work has a composite membrane consisting of a thin outer layer and a porous support structure. The next chapter describes the solution diffusion model with a dense membrane and the pore flow model with a porous membrane. (Melin and Rautenbach, 2007).

2.1.1.1 Solution-diffusion-model

For a dense membrane, the solution diffusion model is used. It is assumed that the components to be separated, dissolve as in a liquid and then move by diffusion through the membrane. The permeability of such a membrane is determined by its diffusion coefficient in the membrane, the concentration in the membrane and the driving forces. The equation is:

$$J_i = C_{i,M} * D_{i,M} * grad(\mu_{chem,i}) \qquad \text{Eq. 2}$$

$C_{i,M}$ is the concentration in the membrane and $D_{i,M}$ is the diffusion coefficient in the membrane (Melin and Rautenbach, 2007).

2.1.1.2 Pore-flow-model

When investigating mass transport through a porous membrane, it can be assumed that it behaves like a flow through a porous bed. The pore flow model assumes that the liquid flows in pores that are closed off from each other like laminar flow in several cylinder tubes. With the help of the Hagen-Poiseuille equation, the specific flow can then be formed:

$$J = \frac{n*\rho*\pi*r^4{}_p*\Delta p}{8*\mu*\Delta L} \qquad \text{Eq. 3}$$

Here r_p is the pore radius, n the specific number of pores, μ the dynamic viscosity, ρ the fluid density and ΔL the membrane thickness. Analogously, the flow equation for a porous packing can be derived according to Carman-Kozeny:

$$J = \frac{\varepsilon^3*\rho*\Delta p}{K_C*\mu*a_v{}^2*(1-\varepsilon)^2*\Delta L} \qquad \text{Eq. 4}$$

Here ε is the porosity, a the inner surface and K_C is the Carman-Kozeny constant (Melin and Rautenbach, 2007)

2.1.1.3 Resistance-model

As many parameters such as permeability, concentration in the membrane and diffusion coefficients in the membrane are difficult to determine, a simplified resistance model proved to be practical. k represents the total mass transfer resistance. k_1 to k_n represent the partial resistances. The partial resistances represent different parts of the membrane system. Using the resistance model as a whole membrane model, i.e., from feed to permeate, the resulting mass transfer coefficient regards the whole system. To calculate the flux the driving force gradient from feed to permeate is used and assuming partial pressure is the driving force, the resistance model can be described as (Ho and Sirkar, 1992):

$$\frac{1}{k} = \frac{1}{k_1} + \cdots + \frac{1}{k_n} \qquad \text{Eq. 5}$$

$$J = k * \Delta p_i \qquad \text{Eq. 6}$$

2.1.2 Hollow fiber membrane

Hollow fiber modules consist of thin tubes or fibers that are bundled together in a module. The fibers are usually microporous with a solid layer, either coated on the outside or inside. The high membrane surface area is a big advantage countered by low flow rates. Fiber diameters range from 50 to 3000 µm. The most common is parallel or staggered arrangement of fibers in the bundle. Hollow fiber membranes are used in dialysis and gas permeation. Another disadvantage is that fibers tend to clog easily and are difficult to clean. A typical hollow fiber membrane module arrangement can be seen in Figure 2 (Baker, 2000; Melin and Rautenbach, 2007; Rackley, 2017).

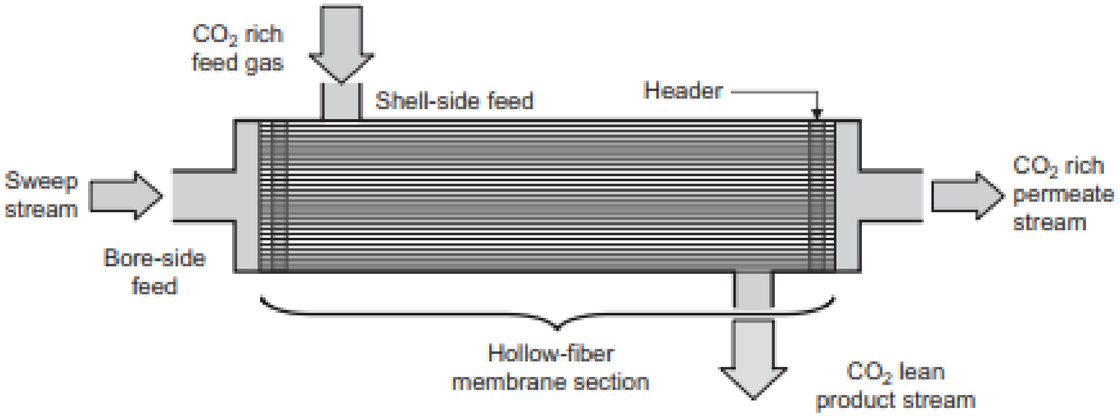

Figure 2: Hollow fiber module structure. (Rackley, 2017)

2.1.3 Blood oxygenators

Hollow fiber membrane modules form a typical artificial lung. In blood oxygenators, fibers made of hydrophobic polymers are typically used. Hydrophobic behavior is desired so that the membrane is gas filled and oxygen can easily diffuse into the blood. The fibers have typical diameters of 200-400 µm and a wall thickness (membrane thickness) of 20-50 µm. The membrane pores usually have a size of 0.1 µm and for the fiber wall a porosity of 30-50 % is common. In a typical oxygenator, oxygen flows through the lumen into the fibers. This gas flow is called "sweep gas". On the outside blood flows through the interstices of the packing. Oxygen diffuses along the descending gradient from the inside of the fiber through the wall into the blood. Carbon dioxide also follows the downward gradient, but from the outside, the blood phase, through the wall into the sweep gas. The sweep gas transports the CO_2 away. Figure 3 depicts a cross section of a fiber bundle and a zoomed-in picture of a fiber wall (Federspiel and Henchir, 2008).

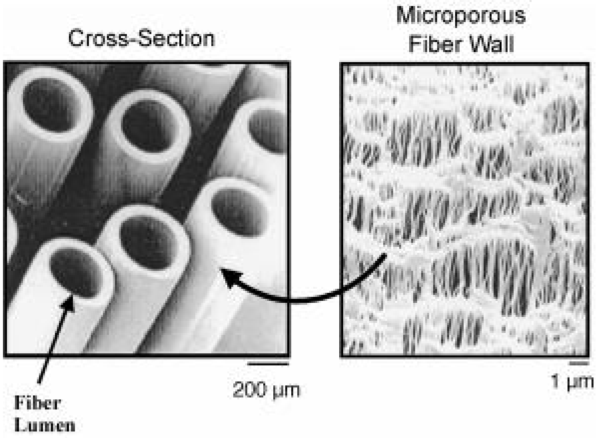

Figure 3: Cross section of a fiber bundle and zoomed in picture of a fiber wall. (Federspiel and Henchir, 2008)

2.1.4 Determinants of CO_2 gas exchange in blood oxygenators

The permeance of CO_2 in a blood oxygenator represents the mass transport coefficient. This permeance can be related to the gas exchange rate with the form:

$$J_{CO_2} = k_{CO_2} * A * \Delta p_{CO_2} \qquad \text{Eq. 7}$$

J_{CO_2} represents the CO_2 transport rate, k_{CO_2} the mass transport coefficient, A the membrane surface and Δp_{CO_2} the partial pressure difference between the sweep gas and blood. The driving force of CO_2 exchange is the partial pressure difference between blood and sweep gas. The mass transport coefficient is the resistance to the diffusing CO_2. This resistance is composed of the gas side resistance (k_g), the blood side resistance (k_b), and the membrane resistance (k_m). The gas side resistance can be neglected, since it is comparatively smaller than the blood side resistance and membrane resistance. This gives the form for the mass transport coefficient of:

$$\frac{1}{k_{CO_2}} = \frac{1}{k_m} + \frac{1}{k_b} \qquad \text{Eq. 8}$$

The greatest diffusion resistance comes from the blood side permeance, second is the membrane permeance and weakest the gas side permeance. Blood side resistance and membrane resistance dictate the CO_2 transport (Federspiel and Henchir, 2008).

2.1.5 Concentration polarization

In membrane separation processes, the feed passes through the membrane, where on the other side the permeate is enriched with one of the components of the feed. Components of the feed permeate at different rates and concentration gradients occur on both sides in the fluids. This phenomenon is called concentration polarization. Similar phenomena can be seen in heat transport processes. Mathematical models are often adapted from these. Concentration polarization may have a significant effect on the flux since it lowers the concentration gradient of the permeating component across the membrane. Good mixing on both sides of the membrane reduces polarization. Figure 4 shows the concentration polarization (Baker, 2000).

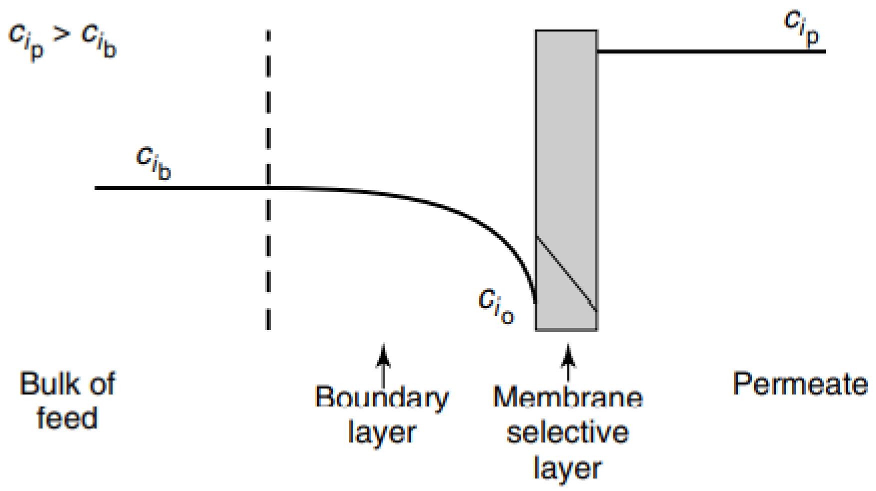

Figure 4: Concentration polarization. (Baker, 2000)

Another approach for the concentration polarization is to model the phenomenon by assuming that a thin layer of unmixed liquid exists between the membrane surface and the well-mixed main solution. This layer is called the boundary layer. The concentration gradients that control the concentration polarization form this layer. This boundary layer film model oversimplifies the fluid hydrodynamics that occur in membrane modules. The model, however, represents most experimental findings good enough (Baker, 2000).

2.1.6 CO_2 solubility and transfer

This master thesis describes the CO_2 removal rate in a blood oxygenator for blood and water. Therefore, the solubility and transport of CO_2 in blood and water are of importance. Both is explained in the following chapters.

2.1.6.1 CO_2 solubility and transport in water

99% of CO_2 is physically dissolved in water and less than 1 % remains as carbonic acid. During the CO_2 separation process via membranes, physically dissolved CO_2 is removed only (Knoche, 1980).

2.1.6.2 CO_2 solubility in blood

CO_2 is not only physically dissolved in blood (5 %), but also bound chemically as carbaminohaemoglobin (5 %) and bicarbonate (90 %). The dissociation curve (Figure 5) is the dependency of total CO_2 concentration on CO_2 partial pressure and can be expressed by:

$$C_{CO_2} = q\mathrm{p_{CO_2}}^{t} \qquad \text{Eq. 9}$$

The coefficients q and t are empirical regression parameters. With q having the value of 0.128 and t of 0.369 (Svitek and Federspiel, 2008b).

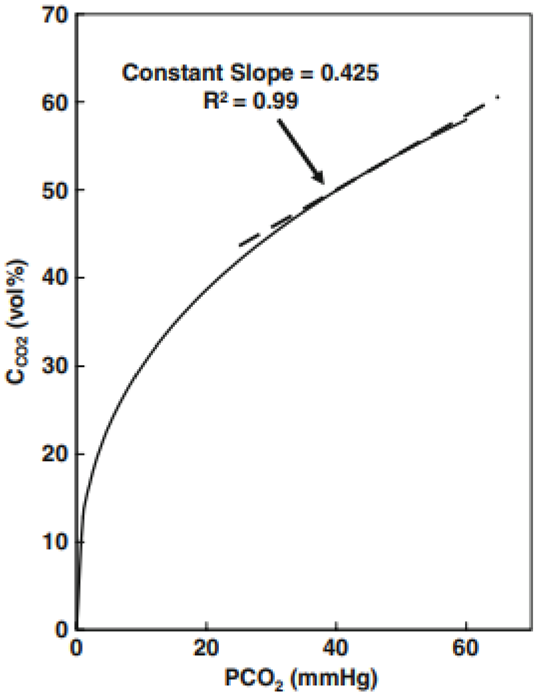

Figure 5: CO_2 dissociation curve with linear slope in the range of 25-50 mmHg. (Svitek and Federspiel, 2008a)

2.1.6.3 CO_2 transfer in blood

In the CO_2 separation process via a membrane only physically dissolved CO_2 is removed. Physically dissolved CO_2 depends on other forms of CO_2 through chemical reaction and all CO_2 components must be considered. Two reactions occur with CO_2 in red blood cells. The first reaction: CO_2 is hydrated in the presence of the enzyme carbonic anhydrase and carbonic acid arises. The second reaction: dissociation of carbonic acid into hydrogen ion and bicarbonate. The reactions are described in the following form:

$$CO_2 + H_2O \overset{Reaction\ 1}{\Longleftrightarrow} H_2CO_3 \overset{Reaction\ 2}{\Longleftrightarrow} H^+ + HCO^-{}_3 \qquad \text{Eq. 10}$$

With removal of CO_2 from plasma through the membrane, bicarbonate diffuses into the red blood cells. It is converted through reverse reactions of reaction 2 and then reaction 1 into carbon dioxide which diffuses into the plasma, from which the physically dissolved CO_2 can be further removed. It is assumed that the enzyme carbonic anhydrase is available to catalyze reaction 1 throughout the carbon dioxide removal process. (Svitek and Federspiel, 2008a).

2.2 CFD

To find out how well water models blood in the context of CO_2 transport, computational fluid dynamics (CFD) simulations were performed. This is an inexpensive and quick way to gain insight into the internal flows. In the following chapters the basics of CFD will be discussed.

CFD is the analysis of systems containing flows, heat transport, mass transport and phenomena associated with them. The analysis is carried out with the help of computer-based simulation. The next chapter deals with the basic workflow of a CFD simulation (Versteeg and Malalasekera, 2007).

2.2.1 Workflow of CFD

The workflow of a CFD simulation is structured around the numerical algorithm that solves the flow problem. The workflow is divided into three parts, the pre-processing, the solver, and the post-processing.

2.2.1.1 Pre-processing

The simulation is prepared during pre-processing. This is done in a CFD program. The geometry (computational domain) is being defined and the grid being generated. The grid consists of non-overlapping cells that fill the geometry volume. The solution of the flow problem is defined in nodes of the cells. Typically, a higher number of cells gives a higher accuracy of the simulation. However, the higher the number of cells, the higher the computational requirements. Therefore, most meshes are non-uniform and only refined where needed (Versteeg and Malalasekera, 2007).

Besides the mesh, the properties of the fluid are defined, and the physical and chemical models needed are selected. In addition, the conditions in cells at the edge of the geometry must also be determined, also called the boundary conditions (Versteeg and Malalasekera, 2007).

2.2.1.2 Solver

The 4 most common numerical solution methods are: finite differences, finite elements, spectral methods, and finite volumes. Only the finite volume method (FVM) is presented here, as it has been used for this work. Basically, the finite volume method can be divided into 3 steps (Versteeg and Malalasekera, 2007).

First, the equations of the conservation of mass, energy, and momentum (governing equations) are integrated over all sub-volumes of the geometry. This step distinguishes the FVM from all other methods because the general flow variables are conserved in each finite cell center (centroid) (Versteeg and Malalasekera, 2007).

Second is the discretization of the partial differential equations into a system of algebraic equations. Discretization must be performed in space and time for all differential terms of the equations. The discretization is an interpolation of neighboring centroid values to obtain values of the faces. If the variation in a discretization scheme between the centroids is constant, this is called a first order scheme, if the variation is linear this is called a second order scheme. For good accuracy the order of the discretization scheme should be at least the same order as the equation being discretized (Versteeg and Malalasekera, 2007; "Wolf Dynamics - Customer-driven flow solutions," 2021).

Third is the iterative solution of the system of equations. The most common algorithms used in OpenFOAM® are the pressure-implicit split-operator (PISO), the semi-implicit method for pressure-linked equations (SIMPLE), and the combined PISO and SIMPLE algorithm PIMPLE. The algorithms couple the equations for momentum and mass conservation and specify the order in which the equations must be solved (looped). The SIMPLE algorithm is used for steady state analysis, the PISO algorithm for transient simulations, and the PIMPLE algorithm for transient simulations with larger time steps (Greenshields, 2019).

2.2.1.3 Post-processing

The third step of a typical CFD workflow is post-processing. The results from the models being displayed visually. Examples of post-processing are geometry display, vector plots, particle tracking, and contour plots (Versteeg and Malalasekera, 2007).

3 Methods

This chapter explains the methods used. Based on the literature review presented in the introduction, it can be assumed that water is a widely used and good enough model for the CO_2 removal rate in blood. To verify this, water, and blood CO_2 removal rates were determined experimentally. The blood oxygenator used, and the design of the experiments is explained in chapter 3.1 and 3.2.

As there is no discourse on the comparability of water and blood in terms of CO_2 removal rate in literature. CFD simulations were performed, these were validated with the experiments. Based on the results of simulation and experiments, a boundary layer analysis was performed. The specific methods of the simulations are explained in chapter 3.3. Furthermore, the calculation methods of the boundary layer analysis are presented.

The *Sherwood model conversion* method according to Federspiel et al. (2008) is presented in chapter 3.4. With this model, the CO_2 removal rate of blood can be determined with the help of CO_2 removal rates of water.

3.1 The prototype module

The prototype module consists of a fiber mat, a module case and a baffle. The fiber mat surrounds the inlet and outlet pipe, the hollow fiber mat having the form of a hollow cylinder, the inlet and outlet pipe having a diameter of 6 mm, the fiber cylinder having an inner diameter of 6 mm and an outer diameter of 16 mm, being enclosed by the module shell. The module shell has an inner diameter of 20 mm leaving a 2 mm ring gap between packing and shell. The baffle blocks the blood flow in the inner channel and is positioned in the middle of the module. The baffle coerces the blood to flow transversely through the packing. The hollow fibers (Membrana Oxyplus 90/200 PMP, 3M) have a length of 10 cm. 500 of these are packed into the module. The fibers are radially and tangentially 200 μm apart. This results in a membrane surface of 0.06 m^2 and a porosity of 0.55. The Prototype is pictured in Figure 6 (Lukitsch et al., 2020).

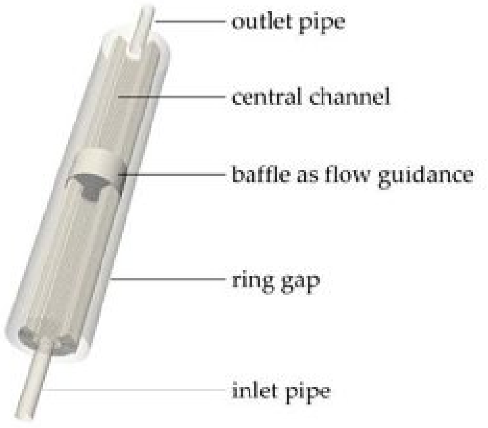

Figure 6: Blood guiding parts of the prototype oxygenator with cut through the membrane packing. (Lukitsch et al., 2020)

3.2 Experiments

To validate the capability of water as a blood substitute, data sets of various experiments were used. These experiments were conducted by staff of the Technical University of Vienna. The aim of the experiments was to determine the carbon dioxide removal performance of the prototype module at different inlet conditions. Two test series were done. The first row of experiments was done in vivo (tests outside the living animal) on pigs (Lukitsch et al., 2020) and the second set was done with water. Both test runs were conducted with the same initial conditions. Three flow rates were carried out, each with three CO_2 partial pressures resulting in 9 datapoints per run. The flow rates used were 1000, 1300 and 1600 ml/min, the partial pressures having been 50, 70 and 100 mmHg.

3.2.1 In vivo porcine blood tests

Two pigs were provided by the teaching and research farm of the University of Veterinary Medicine, Vienna. All tests were performed under the ethics proposal ZI. 8/115-97/98 (Lukitsch et al., 2020). The pigs were sedated and mechanically ventilated, this provided stable experiment conditions. Ventilation was obtained using an endotracheal tube. The ventilator (Servo 900C, Siemens) controlled the oxygen saturation and the CO_2 partial pressure. A Ringer Solution was applied to help maintain the physiological blood pressure. Furthermore, heparin was administered preventing blood coagulation and thus clotting of the hollow fiber bundle. The pigs blood pressure, cardiac output, body temperature, and heart rate were kept track of (PiCCO plus, Pulsion Medical System). The pumped blood (BPX-80, Medtronic) from the femoral vein flows from the pig's body to the oxygenator prototype. After the CO_2 was removed in the prototype, the blood flows back via the vena jugularis into the pig. Flow rate of the blood was measured with an ultrasonic flow probe (SONOFLOW CO.55/080). The blood was analyzed before and after the prototype by analyzing 3 samples in a blood gas analyzer (ABL500 FLEX, Radiometer Medical A/S). Parameters measured by the blood gas analyzer include haematocrit, partial pressure of CO_2 and O_2, as well as various other blood parameters. Pure O_2 was used as sweep gas flowing (1 L STP/min) through the fiber lumen. The gas flow was controlled by a mass flow controller (GF40, Brooks). Furthermore, the outgoing gas flow was analyzed with a volumetric measurement device (Defender 510, Bios DryCal) and a CO_2 concentration measurement device (BINOS 100M, Emerson). Using the volumetric and concentration measurements, the CO_2 removal rate was determined. The experimental set-up is pictured in Figure 7(Lukitsch et al., 2020).

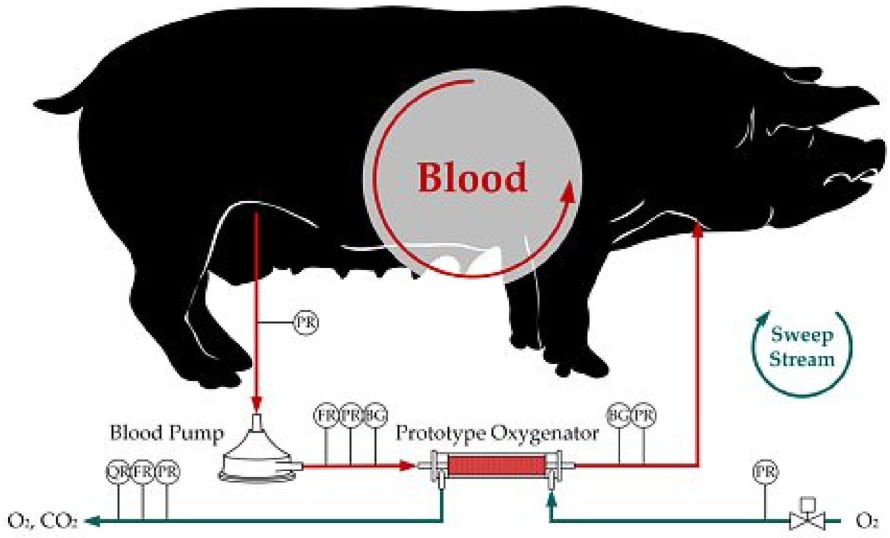

Figure 7: Scheme of the in vivo loop with pig, prototype oxygenator, blood pump, pressure sensors (PR), flow rate sensors (FR), and CO_2 concentration sensors (QR). (Lukitsch et al., 2020)

3.2.2 In vitro water tests

The CO_2 removal rate for water in the prototype was examined in an in vitro recirculation loop. This loop consists of three flows, the main water circulation (the loop), the pure O_2 sweep stream, and the CO_2 saturation stream. Deionized water at 37 °C was used in the main loop and was pumped (centrifugal pump, BPX, Medtronic) through the shell side of an extracorporeal membrane oxygenator (ECMO Adult, Eurosets). After having been saturated with CO_2 in the ECMO, water flows through the prototype, and CO_2 and O_2 are exchanged in the prototype. A clamp-on ultrasonic flow probe (SONOFLOW CO.55/080) surveyed the water flow rate. The flow rate of the sweep (1 L/min) and the saturation stream were regulated by three mass flow controllers (GF40, Brooks). The CO_2 levels of the water were measured before and after the protype with a gas analyzer (ABL500 FLEX, Radiometer Medical A/S). Furthermore, to determine the gas exchange performance, CO_2 concentration measurements of the outgoing sweep stream were conducted. Combining the volumetric and concentration measurements, the CO_2 removal rate was determined. The experiment set-up is the same as the in vitro bovine blood experiments published by Harasek et. al. (2020) and is described in Figure 8.

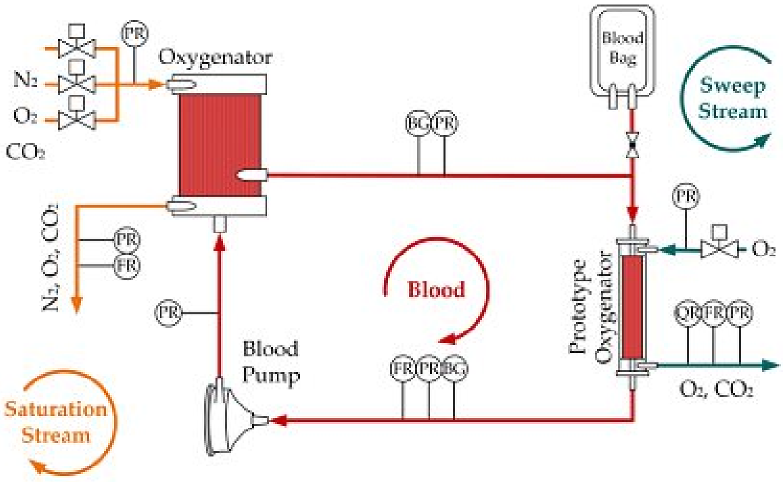

Figure 8: Scheme of the in vitro recirculation loop.

3.3 CFD

The transmembrane flow is predicted using an up-scaling method proposed by Lukitsch et al. (2020). This method allows the use of a smaller geometry for determining the CO_2 mass transport. Two types of CFD simulations are needed for this method. First the flow simulation of the whole geometry and second the mass transport simulation of the reduced geometry. The simulation of the entire geometry is used to determine the general flow properties. The reduced geometry is derived from the results of the whole geometry simulation. Inlet velocities of the reduced geometry were calculated based on the velocity distribution of the flow simulations. With mass transfer simulations of the small geometry, the CO_2 removal can be predicted representatively for the entire geometry. The workflow of the scale-up method is shown in Figure 9 (Lukitsch et al., 2020).

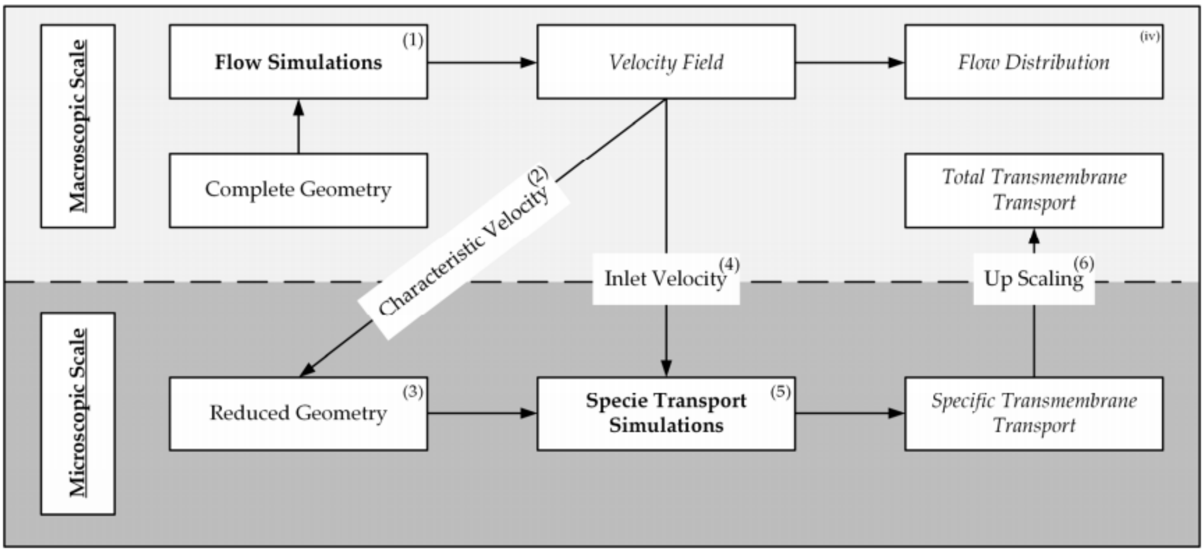

Figure 9: Workflow of the scale up method. (Lukitsch et al., 2020)

A boundary layer analysis was performed on the reduced geometry. The scaled down geometry was used as it is able to model the complete flow distribution. The accuracy of the scale up method with respect to the boundary layer has not yet been validated, however, the results of blood and water can be compared, and qualitative statements can be made.

3.3.1 Flow simulation set up of the complete membrane module

The flow distribution in the module must be known to use the upscaling method. Flow simulations of the blood/water side of the whole geometry (membrane module of the prototype) were conducted. The incompressible Navier-Stokes equations in all three dimensions were solved using a SIMPLE (Semi-Implicit Method for Pressure Linked equations) algorithm (Caretto et al., 1973). Simulations were performed for blood and water at 1000 to 1600 mL/min with increments of 100 mL/min to obtain the characteristic velocity. Both species were modelled as a single-phase fluid. Water can be represented using a constant viscosity. For blood the shear thinning effects must be accounted for. Hence, a power law viscosity model (Johnston et al., 2004) with an upper and lower limit was utilized. Additionally, experimental data was applied to have a better fitting power law model for porcine blood (Lukitsch et al., 2020). For porcine blood the power law coefficients equal μ_0= 8.81 mPa and n=0.792. Maximum viscosity (μ_{max}) being 19.4 mPa and the minimal (μ_{min}) 2.38 mPa. The model for the simulation has the form:

$$\mu_B = \max\left(\mu_{min}, min\left(\mu_{max}, \mu_0 * \gamma^{\dot{n}-1}\right)\right) \qquad \text{Eq. 11}$$

The maximum viscosity limit is necessary for the first solver iterations in order to improve numerical stability. To find out whether the flow is turbulent or laminar the Reynolds number in the packing and the inlet pipe was calculated as presented:

$$Re = \frac{u * L}{\nu} \qquad \text{Eq. 12}$$

The characteristic length in the packing is the distance between the fibers (200 µm). The inlet pipe diameter is 4 mm. Reynolds numbers in the packing (average velocity in the fiber packing at maximum blood flowrate) are around 8.7 and therefore a laminar flow can be assumed. As a result, the Reynolds numbers at the inlet were increased (maximum flowrates), the Reynolds number is about 3650. Thus, further studies were necessary. Turbulent simulations were performed using the k-ω turbulence model. It was found no significant difference of the calculated inlet velocities between the laminar and turbulent simulation. Furthermore, flow profiles and pressure loss were comparable. Therefore laminar simulations were preferred to reduce computational costs (Lukitsch et al., 2020). The Navier Stokes equations, were discretized by a second order scheme. The boundary condition for the inlet is an uniform velocity representing the average flow distribution in the prototype. For the outlet, the pressure was set to 0 Pa relative pressure. No-slip velocity boundary condition was applied to all walls and the membrane. The remaining velocity and pressure boundary condition were set to the zero gradient (Lukitsch et al., 2020). The computational mesh was created using Gambit 2.4.6; Ansys (a commercial meshing software). It was refined lengthwise with OpenFOAM®. The final mesh has 32 million hexahedrally shaped cells. The geometry of the flow simulation is depicted in Figure 10 and Figure 11. Figure 11 zooms-in to the red dotted area in Figure 10. In the direction from inlet to outlet the cell size was constant 0.35 mm. The cell size in the tangential and radial direction in Figure 11 was variable. The cell size within the packing was adjusted to match the reduced geometry refinement. Whereby outside the packed segment, much larger cells have been used to reduce computational cost. The cell size in the inlet and outlet has a minimum of 0.087 mm near the wall and a maximum of 0.175 mm in the main stream (Lukitsch et al., 2020).

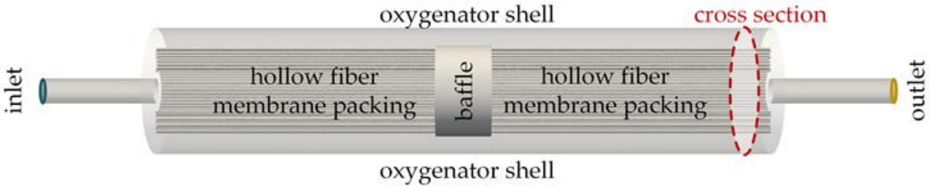

Figure 10: Geometry of CFD flow simulations: Cross section of the prototype oxygenator. (Lukitsch et al., 2021)

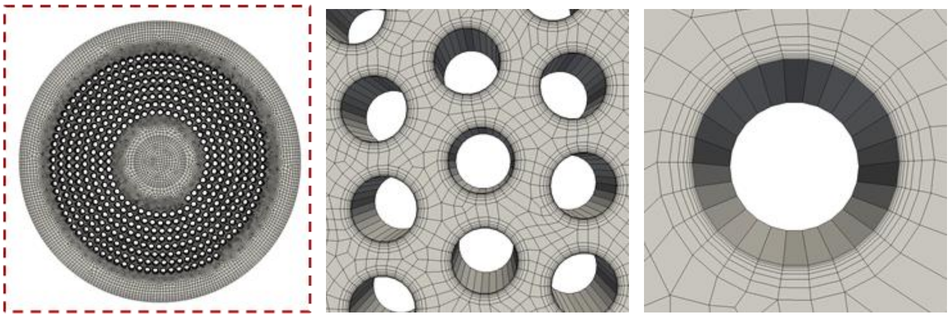

Figure 11: Geometry of CFD flow simulations: Cross section of the fiber packing, with a close up on the boundary layer. (Lukitsch et al., 2021)

3.3.2 Derivation of the reduced geometry

The reduced geometry depends on the results of the flow simulation of the whole geometry. It should reflect the flow properties of the whole geometry as closely as possible. The results of the full geometry simulation can be seen in Figure 13. They show that the packing is generally positioned in a cross flow. The fibers coming after the first row are in the slipstream of the ones before them. They are approached tangentially at their sides. This leads to the simplification of a non-staggered arrangement. The neighbors in angular direction (Figure 12, left) of the individual fibers have no significant influence on the flow behavior. This results in a single line and a non-staggered arrangement of 8 fibers for the reduced geometry of the packing. The distance angularly (200 µm) and in flow direction (radially, 200 µm) between the fibers is analogous to the fiber mats used. The flow in longitudinal direction in the packing is negligible. Since no mass transfer takes place in the module shell, inlet, and outlet these can be neglected. Therefore, the mass transport simulations of the protype finally result in a reduced geometry, consisting of a single line and a non-staggered arrangement of 8 fibers, with idealized, quasi-2-dimensional crossflow. The crossflow is modelled by the inlet velocity boundary conditions. A cross section of the blood guiding parts of the protype (complete geometry) can be seen in Figure 12. The reduced geometry can be seen in Figure 12 (right side). Due to comparable macroscopic flow distribution, the same reduced geometry was used for water and porcine blood (Lukitsch et al., 2020).

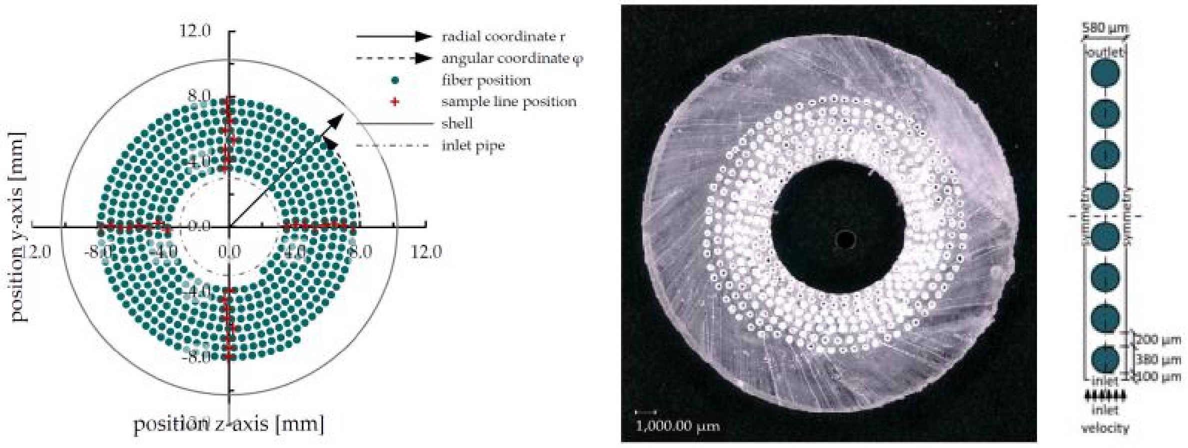

Figure 12: From left to right: Scheme of fiber positions, Cross section of the prototype packing, reduced geometry. (Lukitsch et al., 2020)

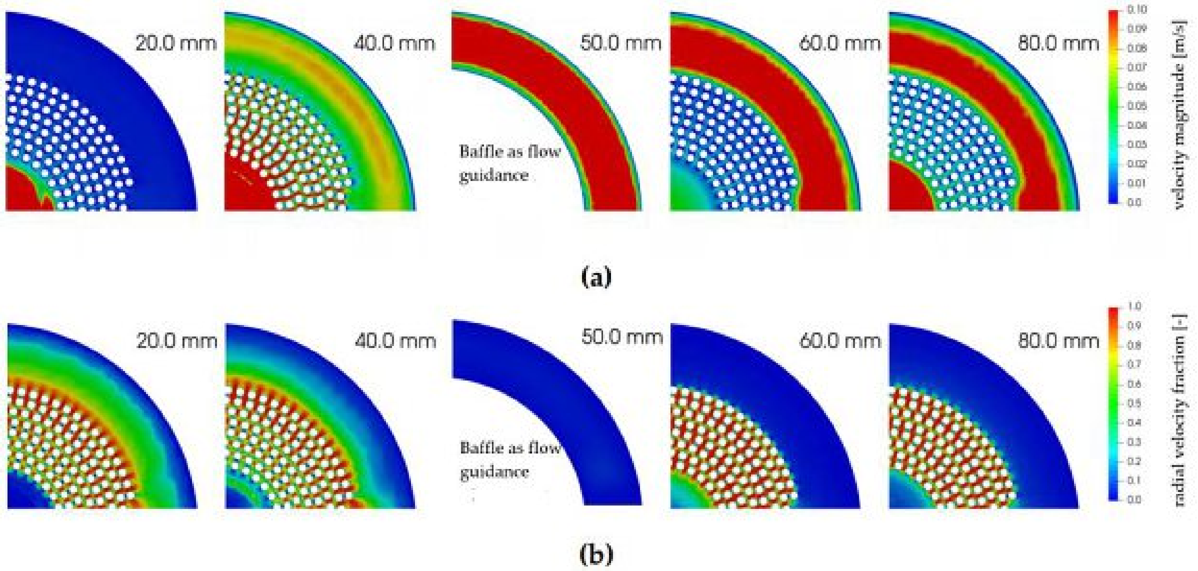

Figure 13: Contour plots at five different longitudinal positions of the complete geometry (a) Velocity magnitude; (b) Fraction of radial velocity component and velocity magnitude. (Lukitsch et al., 2020)

3.3.3 Computation of the inlet velocities

To calculate the inlet velocities of the reduced geometry, it is first necessary to find out which velocity components are representative. Detailed analysis of the flow distribution in the prototype gave that the radial velocity fraction (fraction of radial velocity component and velocity magnitude) is close to one making the radial velocity the characteristic velocity within the packing. The radial velocity fraction distribution is described in Figure 13b (Lukitsch et al., 2020).

An averaged radial velocity must be determined to give an inlet velocity for the reduced geometry representative for the flow distribution in the complete geometry. The radial velocities were recorded on lines parallel to the longitudinal axis and located exactly between two fibers. Sampling lines were positioned at four angles (0 °, 90 °, 180 °, 270 °) and at all eight layers (Figure 12 and Figure 14). The lines were split into 200 points in longitudinal direction resulting in 6400 samples, from which the averaged radial velocity was calculated. The sampled velocities represented the maximum velocity between two fibers.

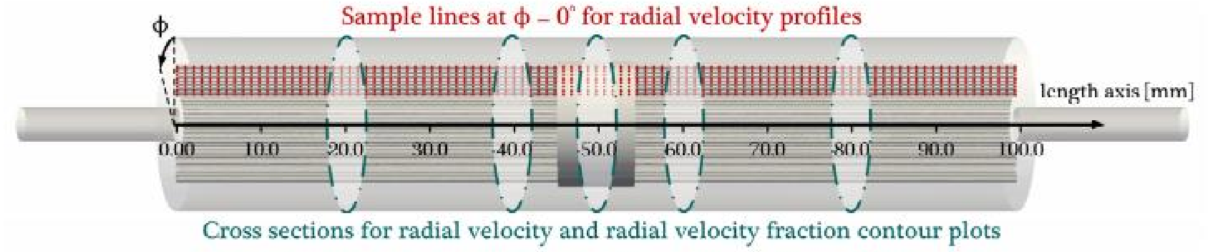

Figure 14: Blood/Water guiding parts of the prototype oxygenator (complete geometry) with a cut through the membrane packing. Red dotted lines: line sources at the angular position ϕ=0° used for sampling of radial velocity profiles. (Lukitsch et al., 2020)

Based on the average of the maximum radial velocity an inlet condition can be calculated. It was found that the following correlation describes the dependency between radial max velocity (u_{max}) and average radial velocity ($\bar{u}$) between two fibers.

$$\bar{u} = \frac{u_{max}}{2^{0.5}} \qquad \text{Eq. 13}$$

The correlation corresponded with the CFD simulation results of the reduced geometry (for blood and water) and a uniform inlet velocity could be formed with the help of the mean velocity and the continuity equation:

$$u_{inlet} = \bar{u} * \frac{A_{spacing}}{A_{inlet}} \qquad \text{Eq. 14}$$

with $A_{spacing}$ being the cross section between two fibers and A_{inlet} being the inlet boundary Area. The flow velocity distribution for water and blood behaved nearly the same, hence the method was used for both species. But blood has a higher average maximum radial velocity magnitude which is discussed in the results. The calculated inlet velocities are depicted in Table 2 (Lukitsch et al., 2020).

Table 2: Inlet velocities of reduced geometry for blood and water.

flowrate [ml/min]	inlet velocity blood [m/s]	inlet velocity water [m/s]
1000	0.015	0.0148
1300	0.024	0.0192
1600	0.031	0.0237

3.3.4 Simulations of the reduced geometry

The mesh of the reduced geometry was created with the OpenFOAM® utility blockmesh and was quasi 2 dimensional. It consisted of 32356 hexahedra and has been adequately improved to map the boundary layer. 36 cell layers were created. The thickness of the cells decreased the smaller the distance to the membrane, with a reduction ratio of 5. The thickness of the cell which is located directly at the membrane is 0.7 µm. The geometry and grid are depicted in Figure 15. The grid convergence index (GCI) , determined for the used mesh, predicts an error due to discretization of about 3 % (Lukitsch et al., 2020).

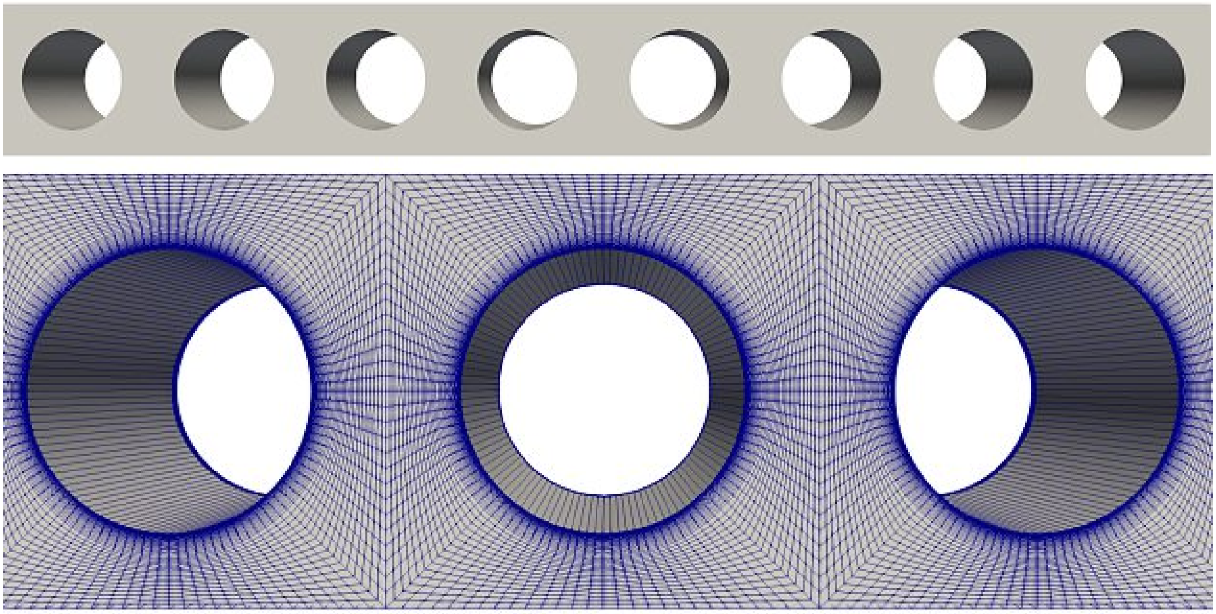

Figure 15: From top to bottom: reduced geometry, close-up of the computational grid.

An in-house multi-region solver called membraneFoam was used to simulate mass transport (Haddadi, 2018). The solver was developed for the CFD toolbox OpenFOAM®. It calculates the transport equations of both regions separately. The regions were separated by the membrane but coupled by transmembrane transport (Ji). The coupling via transmembrane flux was applied as a volumetric source term in all solved transport equations for all cells located at the membrane. The transmembrane transport was calculated using the membrane permeance (P), membrane area (A), and the driving force, the partial pressure difference (Δp_i). The CO_2 partial pressure difference from the computational cell was calculated from its partial pressure and the partial pressure of the cell on the other side of the membrane. If no neighboring cell occurred, the partial pressure difference was interpolated with close by values. The equation of the CO_2 transmembrane transport had the form (Lukitsch et al., 2020):

$$J_{CO_2} = P * A * \Delta p_{CO_2} \qquad \text{Eq. 15}$$

In general, all regions (blood/water, membrane and lumen) could be computed simultaneously by the solver, but previous studies indicated that the main partial pressure drop of CO_2 was on the blood/water side (Harasek et al., 2020). Therefore, the sweep gas side (lumen) has been neglected. Instead, the membrane was considered by utilizing the pure gas permeance. Partial pressure of CO_2 on the gas side was uniformly set to 0 mmHg as the measured outlet CO_2 concentration was low (Harasek et al., 2020). Thus, the multi region solver was used as a single region solver. The specified gas side conditions Eq. 15 reduced to:

$$J_{CO_2} = P * A * \left(p_{CO_2} - 0\right) \qquad \text{Eq. 16}$$

To model CO_2 transport in the blood, all CO_2 associated species were summarized as one total CO_2 specie. The CO_2 transport in blood was described in detail in Section 2.1.6.3. In the simulation, the total CO_2 partial pressure(p_{CO2}) was calculated based on the concentration ($c_{CO2,\,total}$) using the dissociation curve, see Eq. 9 (Lukitsch et al., 2020).

A diffusion coefficient was derived by simplifying the diffusion of total CO_2 to the diffusion of dissolved CO_2 plus the diffusion of bicarbonate. The total CO_2 diffusion coefficient ($D_{CO2,\,total}$) can then be formed as a function of the slope of the dissociation curve (λ_{CO2}), solubility of CO_2 in blood (α_{CO2}), and the diffusion coefficient of dissolved CO_2 (D_{CO2}) and bicarbonate (D_{HCO3^-}). Slope of the dissociation curve can be assumed to be constant for CO_2 partial pressures higher than 50 mmHg (clinically relevant range). It has the form (Lukitsch et al., 2020):

$$D_{CO_2,total} = D_{HCO_3^-} + \left(D_{CO_2} - D_{HCO_3^-}\right) * \frac{\alpha_{CO_2}}{\lambda_{CO_2}} \qquad \text{Eq. 17}$$

A summary of important blood simulation constants can be seen in Table 3.

Table 3 Summary of blood model constants. Values were adapted from Svitek and Federspiel et al. (2008)

notation	description	units	value
α_{CO2}	solubility of CO_2 in blood	mL CO_2 STP/mL/mmHg	6.62 E-04
D_{CO2}	diffusivity of CO_2 in blood	$m^2/2$	4.62 E-10
D_{HCO3^-}	diffusivity of HCO_3^- in blood	$m^2/2$	7.39 E-10
λ_{CO2}	slope of CO_2 dissociation curve	mL CO_2 STP/mL/mmHg	4.25 E-03

The CO_2 transport in water was modelled using a Henry´s law constant and a constant diffusion coefficient. It was simplified that CO_2 is only physically dissolved in water and that the viscosity is constant. Table 4 shows the utilized water values.

Table 4 Summary of water model constants: values were taken from various authors.

notation	description	units	value
α_{CO2_W}	Henry´s law constant for CO_2 in water	mL CO_2 /mL/mmHg	8.27 E-4 (Sander, 2015)
D_{CO2_W}	diffusivity of CO_2 in water	$m^2/2$	2.38 E-9 (Himmelblau, 1964)
ρ_W	density of water	kg/m^3	993.33 (Kestin et al., 1984)
μ_W	dynamic viscosity of water	Pa*s	6.91 E-04 (Wagner and Pruss, 2002)

The Pimple algorithm was used to solve the finite volume formulation of the transient, laminar, and incompressible Navier-Stokes's equations. Discretization schemes and viscosity models were applied in the same way as for the simulation of the entire geometry. The inlet velocity was calculated as explained in chapter 3.3.3 and uniformly set on the inlet patch. To simulate the influence of the adjacent fibers, symmetry boundary conditions were defined at the sides. The missing boundary conditions were defined analogously to the simulation of the entire geometry. For the blood simulations the mass fractions of the individual species were set according to the CO_2 partial pressures of the in vivo tests. Mass fractions of the water simulation were adapted to the in vitro test conditions.

The results for the CO_2 removal rate ($J_{CO2,\text{ reduced geometry}}$) of the reduced geometry can easily be scaled up using the membrane area of the reduced ($A_{\text{membrane, reduced geometry}}$) and entire ($A_{\text{membrane, complete geometry}}$) geometry:

$$J_{CO_2,complete\ geometry} = J_{CO_2,reduced\ geometry} * \frac{A_{membrane,complete\ geometry}}{A_{membrane,reduced\ geometry}} \qquad \text{Eq. 18}$$

For the parameter study, nine simulations were performed for each liquid. To allow validation based on experimental data, 50, 70 and 100 mmHg inlet pCO_2 were simulated at 1000, 1300 and 1600 ml/min flow rate respectively. (Lukitsch et al., 2020).

3.3.5 Concentration polarization layer analysis

The boundary layer analysis was performed for 50, 70, and 100 mmHg CO_2 partial pressure inlet condition at variable inlet velocities (0.005-0.1 m/s). The simulations were carried out in the same way as the parameter study. Using Paraview 5.8.0 post-processing was carried out. The boundary layer was calculated on lines perpendicular to the main flow direction, from the outermost point of a fiber to the wall. In Figure 16 the black lines represent the location for the calculations. The average value over all eight fibers was assumed to be representative for a selected velocity. As criterion for the end of the partial pressure boundary layer 99 % of bulk CO_2 partial pressure was chosen (*Wärme- und Stoffübertragung*, 2009). The focus of this study was the comparison between water and blood at same velocities. Therefore, calculation included the velocity, shear rate, partial pressure profiles. Furthermore, to ease the comparison, dimensionless profiles were computed. All dimensionless profiles were calculated with the help of a reference value. This reference value was obtained at the farthest point away from the fiber on the black lines, see Figure 16. For each line one reference value of each parameter was taken. The data obtained from Paraview was processed with Excel (Microsoft).

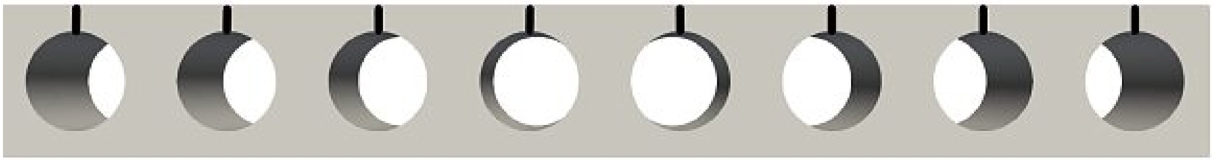

Figure 16: Sample lines for the boundary layer profiles.

3.4 Sherwood correlation

A common method to predict the CO_2 removal rate in blood oxygenators was using mass transport correlation. The *Sherwood model conversion* adapted from Svitek and Federspiel et al. (2008) is presented in the following chapters.

3.4.1 Mass transfer correlation

The mass transfer coefficient for the hollow fiber module was determined by using a Sherwood/Reynold/Schmidt correlation, which is analogous to a heat transfer correlation of a flow perpendicular to a tube bundle (Svitek and Federspiel, 2008a). It has the form:

$$Sh = aRe^{b}Sc^{\frac{1}{3}} \qquad \text{Eq. 19}$$

With Sh being the Sherwood number, Re the Reynolds number and Sc the Schmidt number. a and b are geometry coefficients which were determined experimentally. The Sherwood number represents the ratio of convective to diffusive mass transfer. The Schmidt number is the ratio of momentum to mass diffusivity. The Reynolds number is the ratio of inertial to viscous forces. The dimensionless numbers must be appropriate defined for blood and water (Svitek and Federspiel, 2008a).

3.4.1.1 Dimensionless numbers for water

The Sherwood number for water is defined as:

$$Sh_W = \frac{k_W d_h}{\alpha_W D_W} \qquad \text{Eq. 20}$$

with k_W being the mass transfer coefficient, d_h the hydraulic diameter, α_W and D_W the solubility and diffusivity of the dissolved gas. The hydraulic diameter for the examined hollow fiber membrane module is defined as:

$$d_h = \frac{4V_W}{A_M} \qquad \text{Eq. 21}$$

V_W is the water volume and A_M the membrane surface.

The Reynolds number is defined as:

$$Re_W = \frac{ud_h}{v_W} \qquad \text{Eq. 22}$$

with u being the velocity, which was calculated as the average superficial velocity in radial direction. The kinematic viscosity is denoted as v.

The Schmidt Number is defined as:

$$Sc_W = \frac{v_w}{D_w} \qquad \text{Eq. 23}$$

(Svitek and Federspiel, 2008a)

3.4.1.2 Dimensionless numbers for blood

The Sherwood and Schmidt number has to account for the dissolved and chemically bound CO_2. It will be assumed that the bound forms of CO_2 are always in equilibrium with the dissolved CO_2. The Sherwood number must represent the diffusion of bicarbonate and of the dissolved CO_2. This leads to a facilitated diffusivity in the Sherwood number defined as:

$$Sh_B = \frac{k_B d_h}{\alpha_B D_f} \qquad \text{Eq. 24}$$

$$D_f = D_{CO_2} + \frac{D_{HCO_3}}{\alpha_{CO_2}} \frac{\partial C_{HCO_3}}{\partial p_{CO_2}} \qquad \text{Eq. 25}$$

with $\frac{\partial C_{HCO_3}}{\partial p_{CO_2}}$ being the change in bicarbonate ion concentration dependent on the change in pCO_2. Because there is a lot of HCO_3 relative to the total CO_2 in blood, it can be approximated that $\frac{\partial C_{HCO_3}}{\partial p_{CO_2}}$ is the slope of the CO_2 dissociation curve (J.A. et al., 1983). Therefore, the facilitated diffusivity becomes:

$$\frac{\partial C_{HCO_3}}{\partial p_{CO_2}} \approx \frac{\partial C_{CO_2}}{\partial p_{CO_2}} \approx qtp^{t-1}{}_{CO_2} \equiv \lambda_{CO_2} \qquad \text{Eq. 26}$$

$$D_f = D_{CO_2} + \frac{D_{HCO_3}}{\alpha_{CO_2}} \lambda_{CO_2} \qquad \text{Eq. 27}$$

As the Schmidt number accounts for all chemically bound forms of CO_2, and also needs to include the convection of CO_2 carried as bicarbonate and bound to haemoglobin, the effective diffusivity is defined as:

$$D_{eff\_CO_2} = \frac{D_f}{1+\frac{1}{\alpha_{CO_2}}\lambda_{CO_2}} \qquad \text{Eq. 28}$$

and inserted into the the Schmidt number:

$$Sc_B = \frac{\nu_B}{D_{eff\_CO_2}} \qquad \text{Eq. 29}$$

The Reynolds number for blood is analogous to that of water:

$$Re_B = \frac{u d_h}{\nu_B} \qquad \text{Eq. 30}$$

(Svitek and Federspiel, 2008a).

3.4.2 Predicting the CO₂ removal rate

One method of predicting the Carbon Dioxide removal rate in blood was proposed by Svitek and Federspiel (2008). First the geometry factors a, b (Eq. 19) in the Sherwood correlation are determined experimentally in in vitro tests with water. To do so Sh, Sc, and Re are calculated based on the experimental data and material properties (D, ν, ρ) of water. The Sherwood number contains the mass transfer coefficient which can be calculated like:

$$k_{Exp.W} = \frac{\dot{V}_{CO_2}}{\Delta_{log} p_{CO_2} A} \qquad \text{Eq. 31}$$

with $\Delta_{log} P_{CO_2}$ being the logarithmic mean partial pressure difference between fiber and water. The carbon dioxide removal rate is $\dot{V}_{CO_2}$ and can be calculated with the concentration before and after the membrane module. The velocity in the Reynolds number is the superficial velocity and has the form:

$$u_s = \frac{\dot{Q}_W}{\left(\frac{A_{out}+A_{in}}{2}\right)} \qquad \text{Eq. 32}$$

all other values in the mass transfer correlation for water are constants.

The geometry factors $a \text{ and } b$ can then be obtained by plotting $\frac{Sh}{Sc^{\frac{1}{3}}}$ over the Reynolds number double logarithmically and then using a nonlinear regression of the different experimental data points. Using a and b determined with water, Sh, Sc and Re can be calculated for blood using its material properties. The mass transfer coefficient for blood can be calculated via Sh for different blood flow rates (Re).

$$k^*_B = \frac{a_W * Re_B^{\,b_W} * Sc_B^{\frac{1}{3}} * \alpha_{CO2} * D_f}{d_h} \qquad \text{Eq. 33}$$

Mass transfer can be calculated using:

$$Q\frac{\partial C_{CO_2}}{\partial r} = 2\pi r L k a_v \Delta p_{CO_2} \qquad \text{Eq. 34}$$

With a_v being the surface area per volume of the fiber bundle and Δp_{CO_2} the difference in partial pressure of carbon dioxide between sweep gas and blood. With the empirical fit of the dissociation curve, we obtain:

$$\frac{\partial p_{CO_2}}{\partial r} = \frac{-2\pi r k^*_B a_v L}{Q\lambda_{CO_2}} \Delta p_{CO_2} \qquad \text{Eq. 35}$$

The gas partial pressure is assumed to be zero, Δp_{CO_2} becomes p_{CO_2},the effective solubility is assumed to be constant. With these assumptions the formula can be integrated:

$$p_{CO2out} = p_{CO2in} * e^{\frac{-2\pi k^* a_v L}{Q\lambda} * \left(\frac{{r_{out}}^{2-b} - {r_{in}}^{2-b}}{2-b}\right)} \qquad \text{Eq. 36}$$

The removal rate can then be calculated with:

$$\dot{V}_{CO_2} = \frac{Q * \left(q{p_{CO2out}}^{t} - q{p_{CO2in}}^{t}\right)}{A_{Membrane}} \qquad \text{Eq. 37}$$

(Svitek and Federspiel, 2008a)

4 Results

In this chapter, the results obtained are presented and discussed. The data from the experiments are reported first. Water CO_2 removal rates were compared with those of blood and a first discussion on the comparability of water and blood is given.

Secondly the CFD results of the CO_2 removal rates are presented. These were validated with the data from the experiments. Based on a reasonable match between numerical and experimental results a boundary layer analysis was performed.

For better understanding contour plots were calculated for one inlet velocity and one inlet CO_2 partial pressure. The velocity and pCO_2 distribution of blood and water were discussed.

In the boundary layer analysis velocity, shear rate, and pCO_2 profiles were compared, CO_2 removal rate and boundary layer thickness dependence on blood parameters were investigated.

Another common option to predict gas removal rates in blood oxygenators is with a *Sherwood model conversion* method. Svitek and Federspiel et al (2008) proposed a method to predict the removal rate of CO_2. This method was fitted and adapted to the presented blood oxygenator. The results of these CO_2 removal rate predictions are presented, discussed and compared to the *direct take over* results.

4.1 Experimental results

The tests for water and blood were performed at three different CO_2 partial pressure levels and three different flow rates. The results are shown in Figure 17. The y-axis shows the CO_2 removal rate, the x-axis the flow rate. The blue circles are the results for water and the red rectangles are the results for blood. The inlet partial pressure is indicated by the color of the marker fill, no fill is 50 mmHg, grey fill is 70 mmHg and black fill is 100 mmHg. The dotted lines represent the linear regression of the tests. Transmembrane flow of CO_2 increased with increasing blood and water flow rate. For blood, this dependence increased with the partial pressure of CO_2. This can be seen by the increasing slope of the linear regression (Table 6). The trend line approximated the dependence of the removal rate on the flow rate. It was evident that the oxygenator showed a better CO_2 removal rate for blood than for water. The average deviation is 9.6 %. For 70 and

100 mmHg the deviation is almost constant. The deviation between water and blood decreases at 50 mmHg with increasing flow rate, see Table 5. Experiments for blood show a dependence of CO_2 removal rate on flow rate at 70 and 100 mmHg. The same dependence is seen for water at all partial pressure levels. Experimentally determined CO_2 removal rate for porcine blood shows low dependency of blood flow rate at inlet CO_2 partial pressures of 50 mmHg, i.e. CO_2 removal rate remains almost constant. The slopes of water and blood at 70 and 100 mmHg behave similarly. The deviations of the CO_2 removal rates are sketched in Table 5. Furthermore, the gradients are described in Table 6.

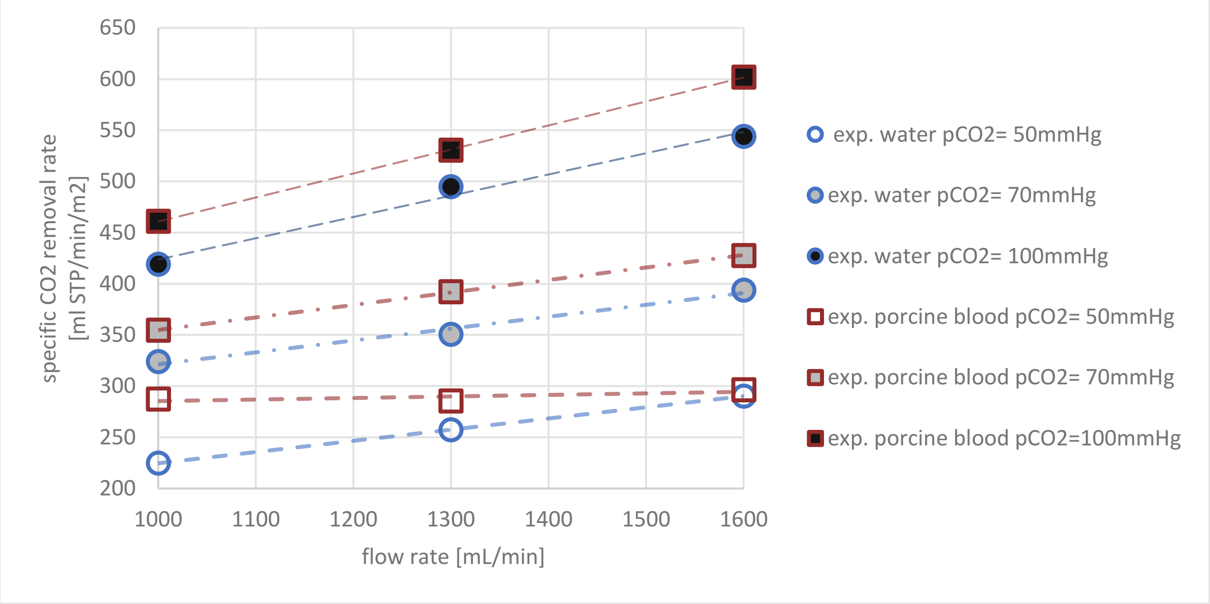

Figure 17: CO_2 removal rate determined experimentally with blood and water.

Table 5: Deviation of blood tests to water tests.

deviation water to blood	**pCO_2 before module [mmHg]**		
Q blood mean [ml/min]	50	70	100
1000	21.81 %	8.58 %	9.08 %
1300	9.94 %	10.6 %	6.71 %
1600	2.1 %	7.93 %	9.64 %

Table 6: Gradients of the linear regressions of the experimental CO_2 removal rate results.

gradients of the linear regression in Figure 17		
pCO_2 inlet [mmHg]	**water**	**blood**
50	0.11	0.015
70	0.12	0.12
100	0.21	0.23

The permeances were measured before and after the experiments (Figure 18). During the test, the permeances decreased strongly. This could have been due to the pores of the membrane filling with water or blood plasma or blood residues forming on the membrane. It can therefore be assumed that there was a reduced permeance during the tests. However, this cannot be measured exactly because the pores dried during the measurements due to the sample gas. The drying of the fibers increased the permeance successively. Permeances in the range of 50 to 400 GPU were measured, see Figure 18. The obtained permeances were compared to the fitted permeances of the simulations.

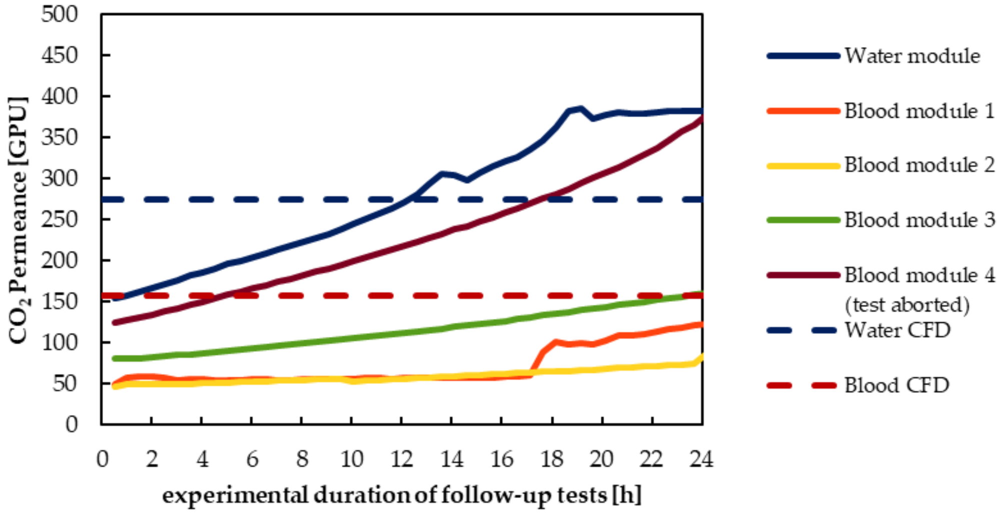

Figure 18: Increase of CO_2 permeance during the follow up gas permeation measurements.(Lukitsch et al., 2021)

4.2 Experimental results discussion

As mentioned in the introduction various research groups have concluded that water is a suitable blood substitute to determine CO_2 removal rates. Our CO_2 removal measurements including variations of CO_2 partial pressure levels and blood/water flow rate showed similar results. The fluids CO_2 removal rate differed by an average of 9.6 %, which is acceptable. For higher CO_2 partial pressures (70 and 100 mmHg), the dependency of the CO_2 removal rate from the flow rate agrees reasonable. Higher deviations were observed only at 50 mmHg and 1000 ml/min. This data point should only be used with caution. It has a higher CO_2 removal rate than the 50 mmHg, 1300 ml/min datapoint. This can be considered unphysical. The Sherwood models presented (chapter 4.9), the performed simulations (chapter 4.3.1), and the results of the experiments of Svitek and Federspiel et al. (2008) all show an increase of CO_2 removal rate with an increase of blood/water flow rate. It can therefore be derived that the experimental data point 50 mmHg 1000 ml/min is incorrect.

In this master thesis only one type of module configuration was used. Further work should compare the water and blood CO_2 removal rates with other module geometries to confirm the results. As the results are similar to those found in the literature, which use different modules, it can be assumed that the geometry has a negligible effect on the comparability of water and blood.

4.3 Validation CFD simulation

CFD simulations were performed for water and blood. The previously presented scale-up method was used to predict the CO_2 mass transport. This parameter study was carried out with the same combination of 3 partial pressures and 3 flow rates as in the experiments. Therefore, the simulation results were directly validated with the experimental results. Simulations were made for CO_2 inlet partial pressures of 50, 70 and 100 mmHg. For each of these levels the flow rate was varied (1000, 1300 and 1600 mL/min).

4.3.1 Blood

The results for blood can be seen in Figure 19. The rectangles connected with a red continuous line represent the simulation results. The rectangles which are not connected are the experimental results presented in chapter 4.1. The dashed lines are the linear regressions of the experimental results. Initial partial pressure is indicated by the filling of the marker, 50 mmHg without, 70 mmHg with grey, and 100 mmHg with black filling.

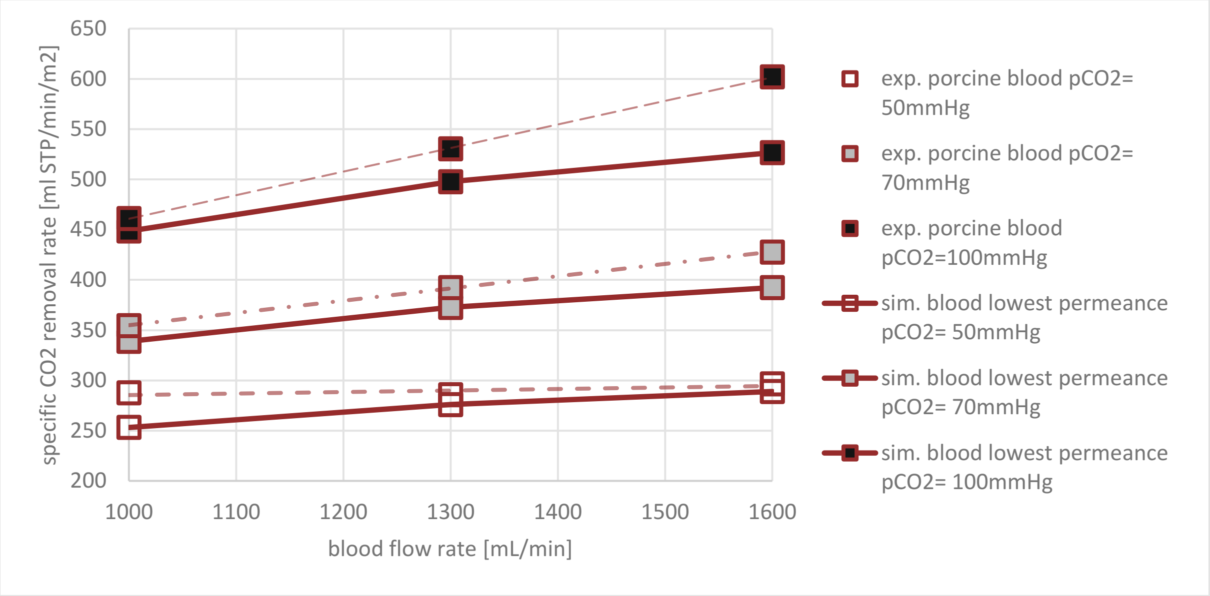

Figure 19: Comparison of the CO_2 removal rate of blood simulations to porcine blood experiments.

A fitted permeance (157 GPU), provided by Lukitsch, et al. (2020), was used. The fitted permeance is in the range of the measured experimental pure gas permeance. The transmembrane flow of CO_2 was predicted with a mean deviation of 6.3 %. The mean deviation is below 10 % this was found to be sufficiently accurate and the permeance was not adjusted further. The highest deviation is found at the point 100 mmHg 1600 ml/min with 12.5 % and the lowest deviation is found at the point 50 mmHg 1600 ml/min with 2.5 %. The simulation best predicts the partial pressure level 70 mmHg. This is as assumed because the permeance was fitted at the point 70 mmHg 1300 ml/min (see chapter 3.3.4). Generally, the blood model under predicts the CO_2 transport. The deviations from simulations to experiments can be seen in Table 7.

Table 7: Deviations of the porcine blood CFD results compared to the experimental results.

deviation sim blood to porcine blood exp	**pCO₂ before module [mmHg]**		
Q blood mean [ml/min]	50	70	100
1000	11.96 %	4.43 %	2.73 %
1300	3.39 %	4.95 %	6.17 %
1600	2.57 %	8.28 %	12.51 %

Table 8 shows the gradients of the linear regression of the simulations and its deviation from the experiments. The slope of the partial pressure at the 70 mmHg is best modelled. For 50 mmHg the gradient is predicted too high and for 100 mmHg it is too low.

Table 8: Gradients of the blood simulation results and deviations of these, compared to the experimental results.

	gradients of the blood simulations	
pCO_2 inlet [mmHg]	blood simulation	deviation
50	0.06	-300.00 %
70	0.089	25.83 %
100	0.13	43.48 %

4.3.2 Water

The first results for water derived of using the same permeance as for blood are posted in Figure 20.

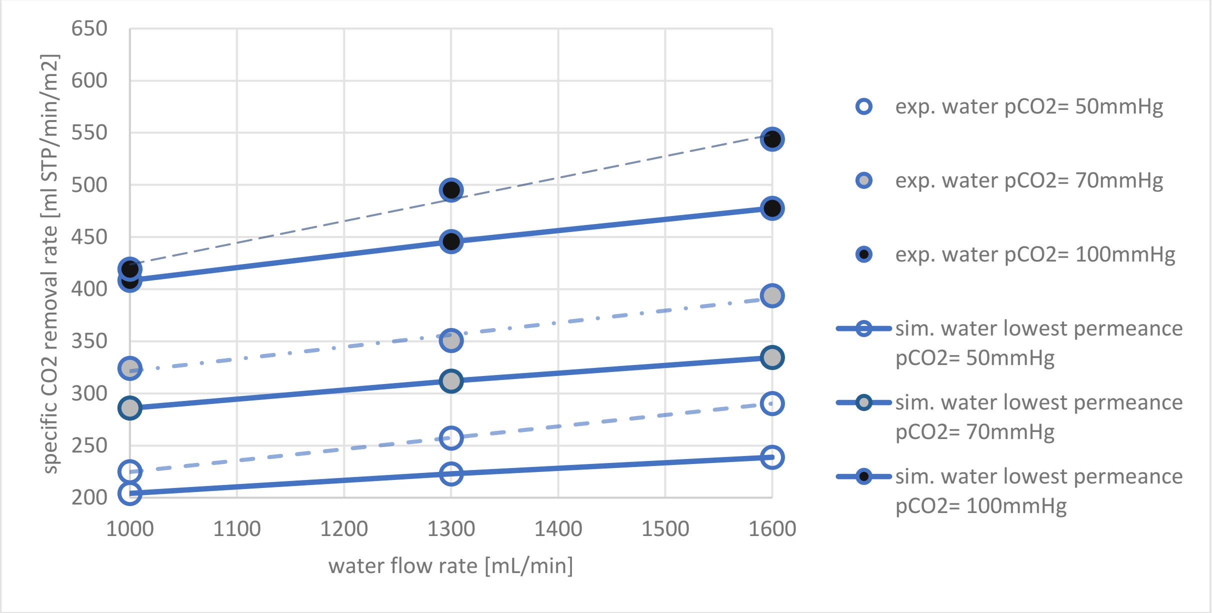

Figure 20: CO_2 removal predicted by water simulations using the same permeance as the blood simulations.

The mean deviation is 11.45 % and was deemed unsatisfactory. Therefore, a permeability study was carried out, based on the 1300 ml/min 70 mmHg point. Simulations with different permeances were carried out to find a linear correlation between the CO_2 removal rate and the permeance. The experimental result of the removal rate at 1300 ml/min 70 mmHg was then used to calculate the fitted permeance. Figure 21 shows the results of the permeance study. The x-axis is the permeance and the y-axis the CO_2

removal rate. The light blue dots indicate the simulation results, the narrow spaced smaller dots are the associated linear correlation with its formula. The grey line indicates the experimental result, the orange dot the calculated fitted permeance. The new permeance was transferred to all simulations with water and has the value of 275 GPU. The results with the fitted permeance are shown in Figure 22.

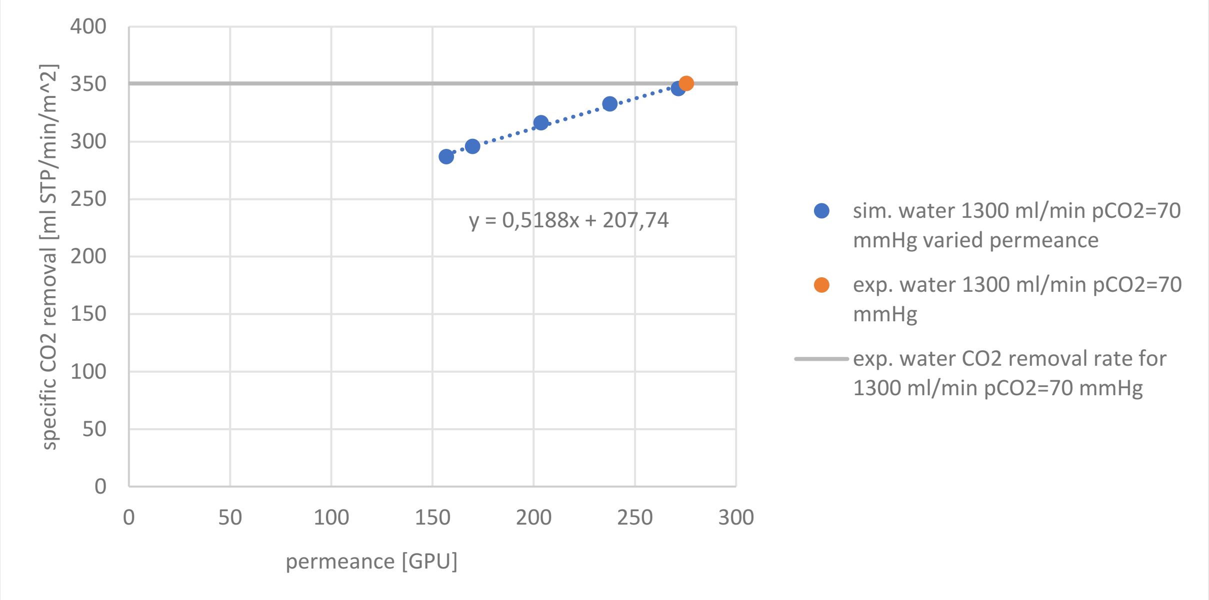

Figure 21: Dependency of CO_2 removal rate from the CO_2 permeance.

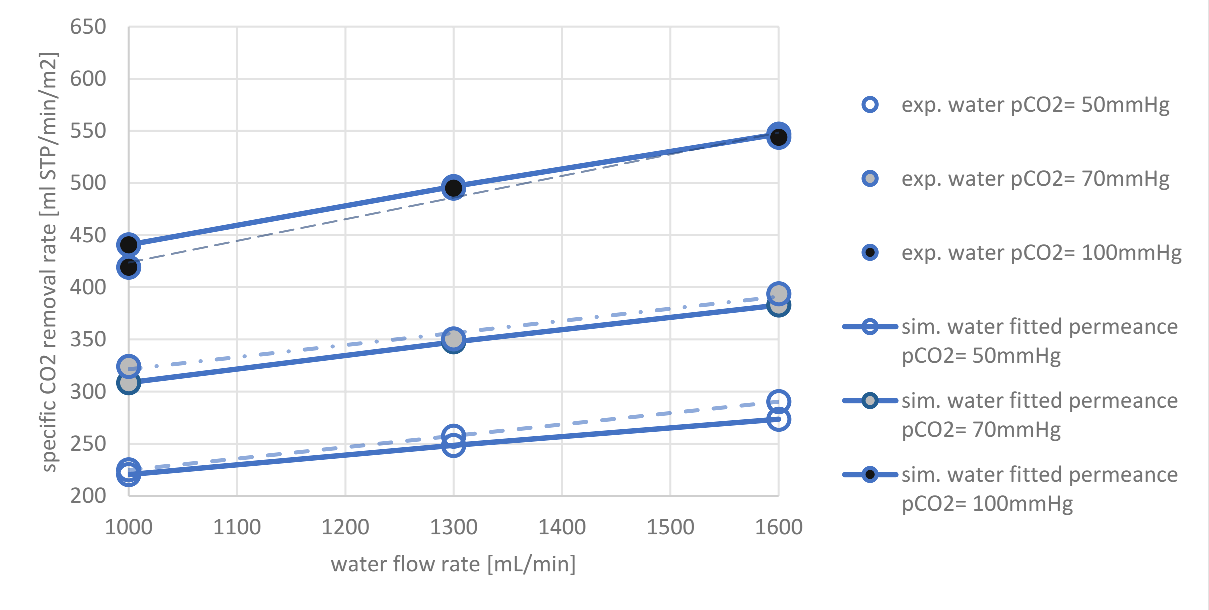

Figure 22: CO_2 removal predicted by water simulations using the fitted permeance.

The mean deviation from simulations to experiments is 2.87 %. The lowest deviation of 0.84 % is found at the point where the permeance has been fitted 1300 mL/min, 70 mmHg. The largest deviation of 5.82 % is found at 1600 mL/min 50 mmHg.

4.4 Discussion on the validation of the CFD simulations

The results of the simulations were judged as satisfactory. The average deviation of the blood simulations is 6.3 % and that of water is 2.8 %.

It is assumed that the permeance decreased during the experiments, because the permeance of the unused fibers (approx. 730 GPU) before the experiments was much higher than after the experiments (pure gas permeances, 50-150 GPU). Resistance increased probably due to wetting of membrane pores and blood residues. The true permeance could not be measured, we assume that it lies between the two permeances mentioned above. The fitted permeances for blood and water are also within this range, see chapter 4.1., therefore, it is assumed that they are representative.

The same fibers were used for the water and the blood experiments, but different permeances were obtained. Water permeances acquired from pure gas experiments were almost twice as high than the blood tests, except for one aborted blood test. Wetting of the fibers was seen with both fluids, therefore it is assumed that the lower blood permeance was due to blood residues. The significantly higher water permeance was also obtained with the fitted permeances. Therefore, it is assumed that the true permeance of water is also higher than that of blood.

In conclusion, the results of the simulation are satisfying. For both fluids the deviation of numerically and experimentally determined CO_2 removal rate lies within 10 %. The permeances used were within the range of the measured pure gas permeances and therefore considered plausible. Thus, the CFD CO_2 transport simulations were considered as validated. They can be used to study the differences between blood and water regarding the CO_2 transport.

4.5 Velocity and CO_2 partial pressure distribution in the simplified packing

In this chapter a brief look at the contour plots of the velocity and the CO_2 partial pressure are made. This allows better understanding of the graphs in the following chapters. Only one velocity and one partial pressure are compared, as the comparison are similar at all velocities and partial pressures. In Figure 23 the velocity distribution of water and blood are compared. The presented inlet velocity is 0.02 m/s and is independent of the CO_2 partial pressure. The blood velocity distributions indicate laminar flow. No wakes are seen. In the water velocity distribution, small wakes occur between the fibers. However, the areas between the fibers have low velocity (approx. 0.01 m/s). Blood and water also differ in that blood has higher maximum velocities and stronger velocity gradients.

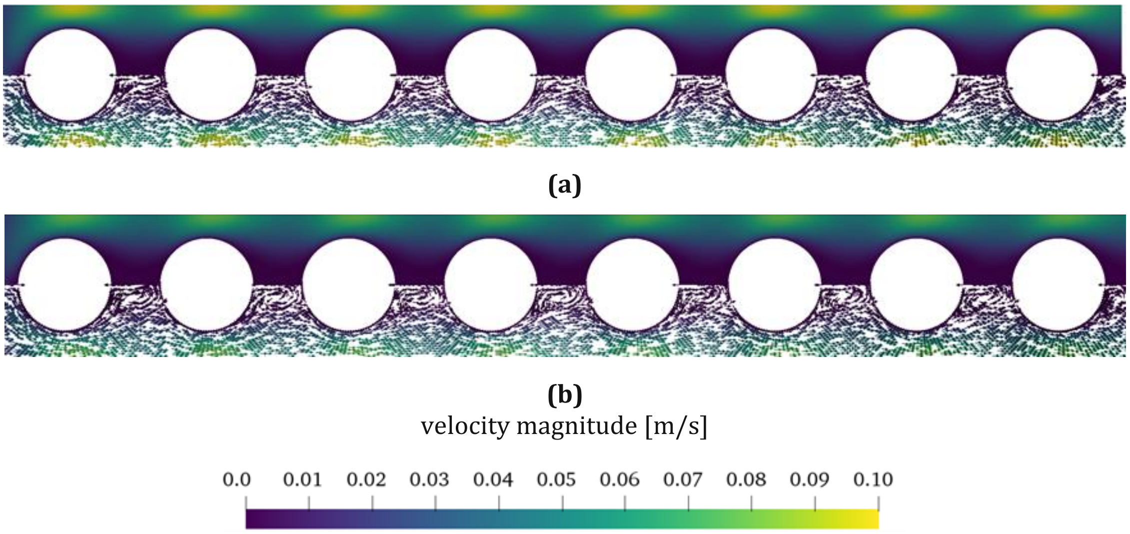

(a)

(b)

Figure 23: Flow distribution within the reduced geometry packing (a) porcine blood (b) water.(Lukitsch et al., 2021)

Figure 24 compares the CO_2 partial pressure contour plot of blood and water for a uniform inlet pCO_2 of 70 mmHg. The water pCO_2 distribution differs from blood in having a larger area of low pCO_2. The low pCO_2 areas can be found near the wakes in Figure 24. This indicates that these wakes contribute to additional mixing.

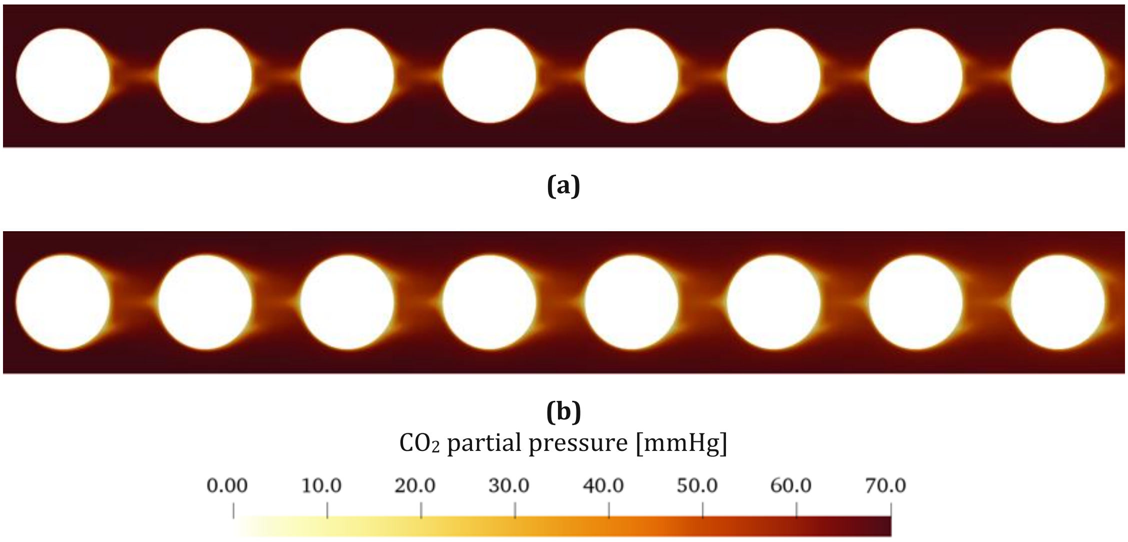

Figure 24: Distribution of CO_2 partial pressure within the reduced geometry packing (a) porcine blood (b) water.(Lukitsch et al., 2021)

4.6 Differences in velocity and pCO_2 distribution between fibers in the reduced geometry

In the chapter 4.7, the results of the boundary layer study are presented. For this purpose, velocities and pCO_2 profiles were calculated which represent the average of the profiles of all 8 fibers in the reduced geometry (see chapter 3.3.5). The following chapter presents the pCO_2 and velocity profiles of the individual fibers. Furthermore, it is shown that the average of the profiles of the 8 fibers is representative for all 8 fibers.

The presented graphs are for pCO_2 70 mmHg and 0.03 m/s. In the figures fiber 1 is the first fiber after the inlet and fiber 8 the last. First the velocity profiles of the individual fibers are compared. In Figure 25 the velocity profiles for blood can be seen and in Figure 26 the velocity profiles for water are presented. The results are similar for water and blood. The velocity profiles of the 8 fibers hardly differ and the average profile represents all 8 fibers. In Figure 25 and Figure 26 all profiles are on the same line.

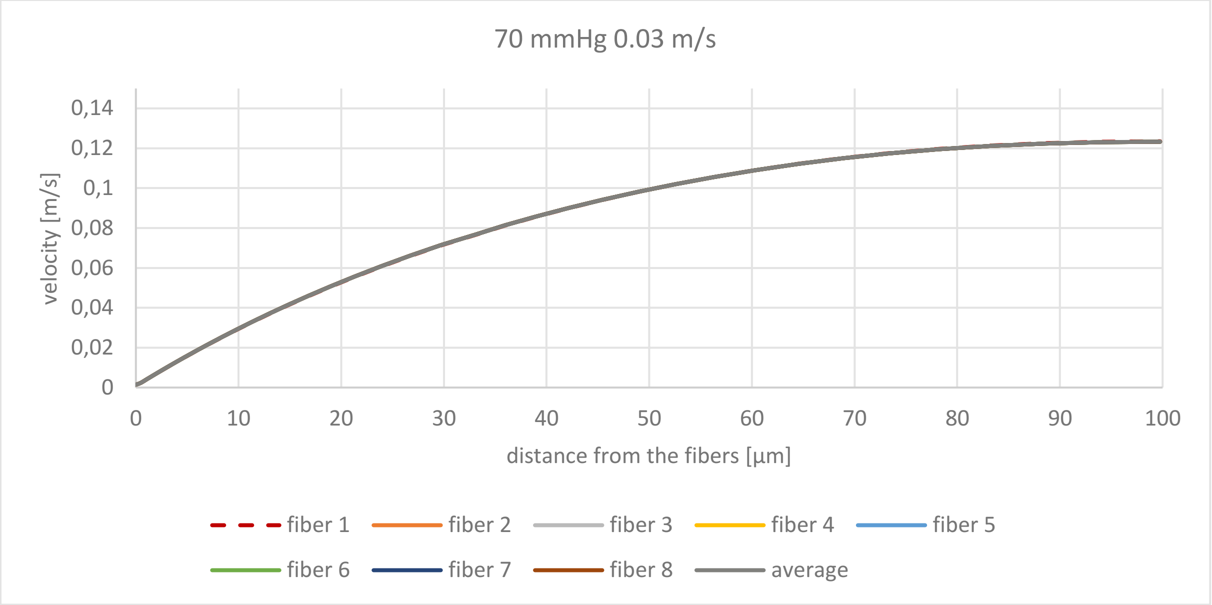

Figure 25: Velocity boundary profile for 70 mmHg 0.03 m/s at different fiber positions for blood.

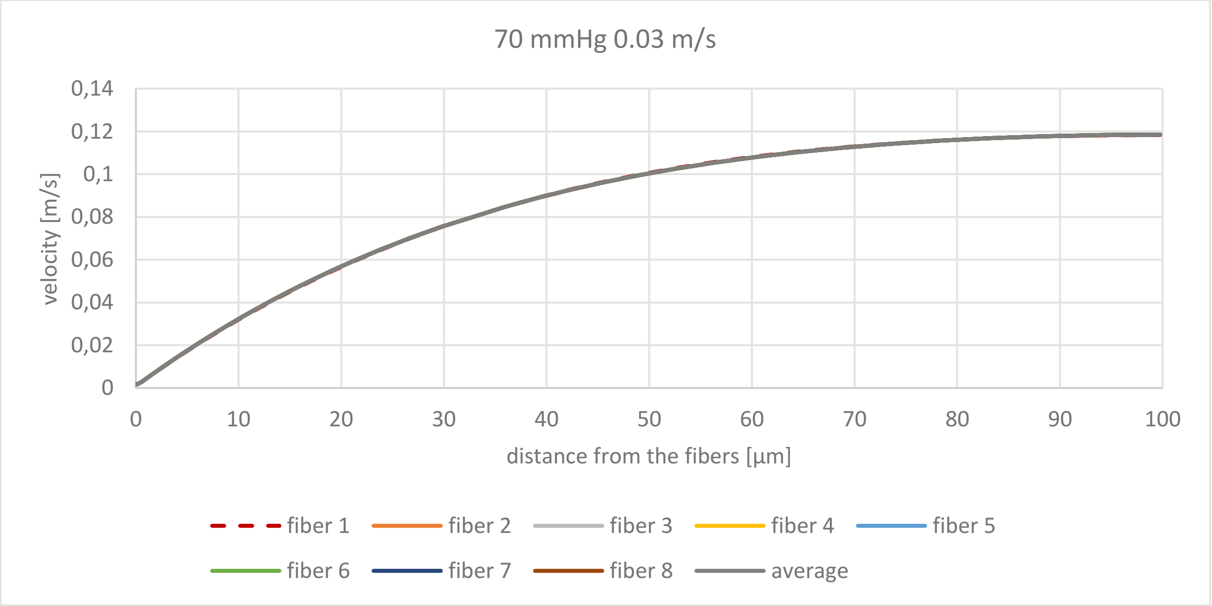

Figure 26: Velocity boundary profile for 70 mmHg 0.03 m/s at different fiber positions for water.

The pCO_2 profiles of the individual fiber profiles show differences. The profiles for blood are presented in Figure 27 and for water are shown in Figure 28. The results for the representability of the average pCO_2 profile are the same for water and blood. The average profile deviates the most for the first fiber, as it is the only fiber that is not in the slipstream of another fiber. All other fibers are well represented by the average value. The dimensionless pCO_2 profile results are not presented as they are very similar to the absolute value and the average dimensionless pCO_2 represents all 8 dimensionless pCO_2 fiber profiles.

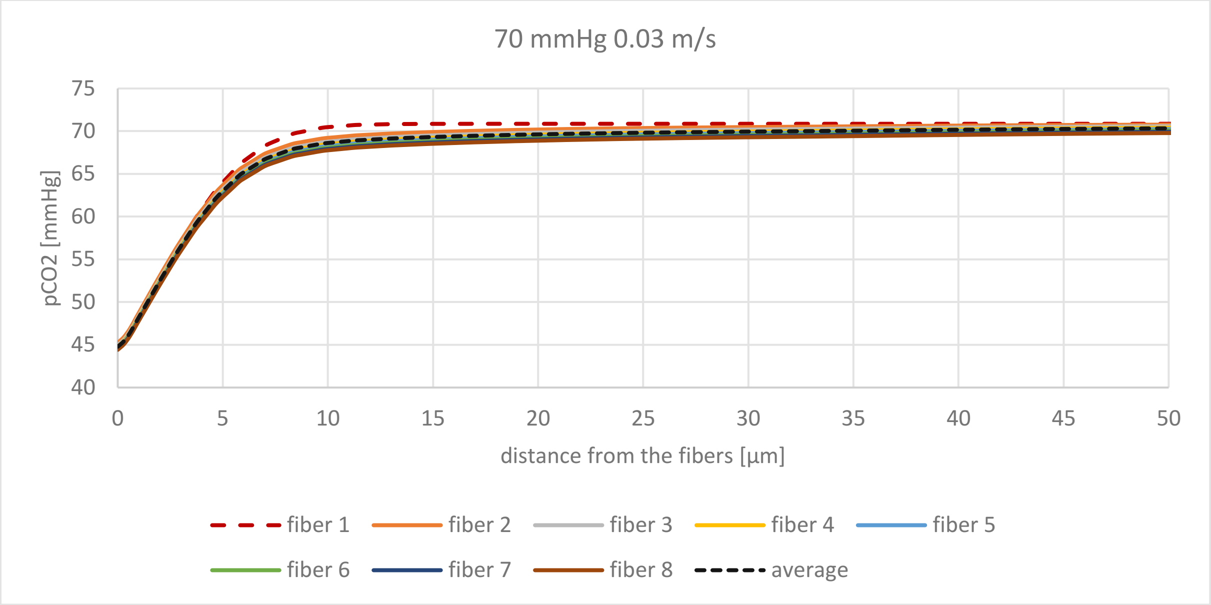

Figure 27: Partial pressure boundary profile for 70 mmHg 0.03 m/s at different fiber positions for blood.

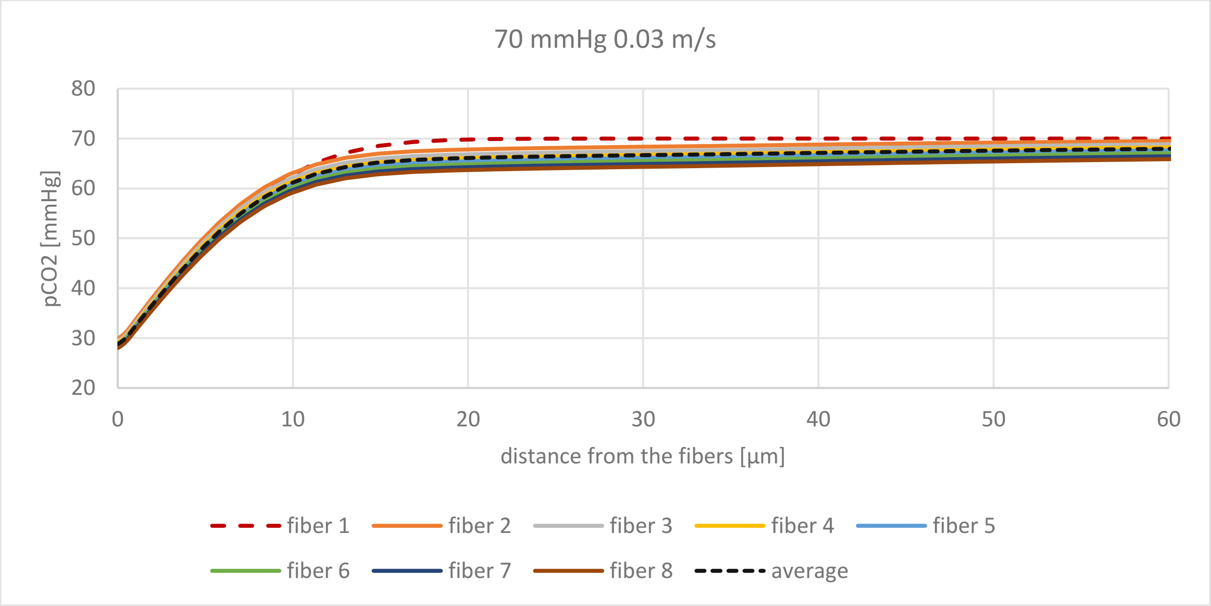

Figure 28: Partial pressure boundary profile for 70 mmHg 0.03 m/s at different fiber positions for water.

4.7 Boundary layer study

Various simulations were carried out for the boundary layer study. Analogue simulations were made for water and blood. For three CO_2 partial pressures (50, 70 and 100 mmHg), eight input velocities (0.005, 0.01, 0.02, 0.03, 0.04, 0.06, 0.08 and 0.1 m/s) were used. Therefore, we obtain 24 data sets per fluid. With these the concentration boundary layers were calculated as described in chapter 3.3.5. Furthermore, the velocity and shear rate profiles were calculated. As presumed with the boundary layer, the averaged shear stress or velocity profile of all 8 fibers was taken as representative for one inlet velocity. The data was plotted over the black lines seen in Figure 16. Focus was the difference between water and blood and their comparability. Furthermore, a dependency study was conducted based on the results. It was analyzed how the CO_2 removal rate and the pCO_2 boundary layer thickness depend on blood-specific parameters. Important to note is that the flow regime is independent of the mass transport. Therefore, the velocity distribution and shear rate distribution are not connected with the partial pressure of CO_2. For both fluids, the three partial pressure levels have the same velocity and shear rate profiles for one specific inlet velocity.

In this chapter, the results from the blood simulations are presented first, then from the water simulations and finally the comparison between the two.

4.7.1 Blood

First the results of blood are presented. The velocity profiles can be seen in Figure 29 and Figure 30. Where Figure 29 is the dimensional velocity. The dimensionless velocity is calculated by taking the outermost velocity on the individual lines of the fibers as a reference. The x-axis of both figures shows the distance from the fibers. The individual lines in the graphs show the different inlet velocities, which decrease with increasing color intensity. Velocity increases moving outwards from the fibers. The dimensionless velocity profiles (Figure 30) are similar for different inlet velocities.

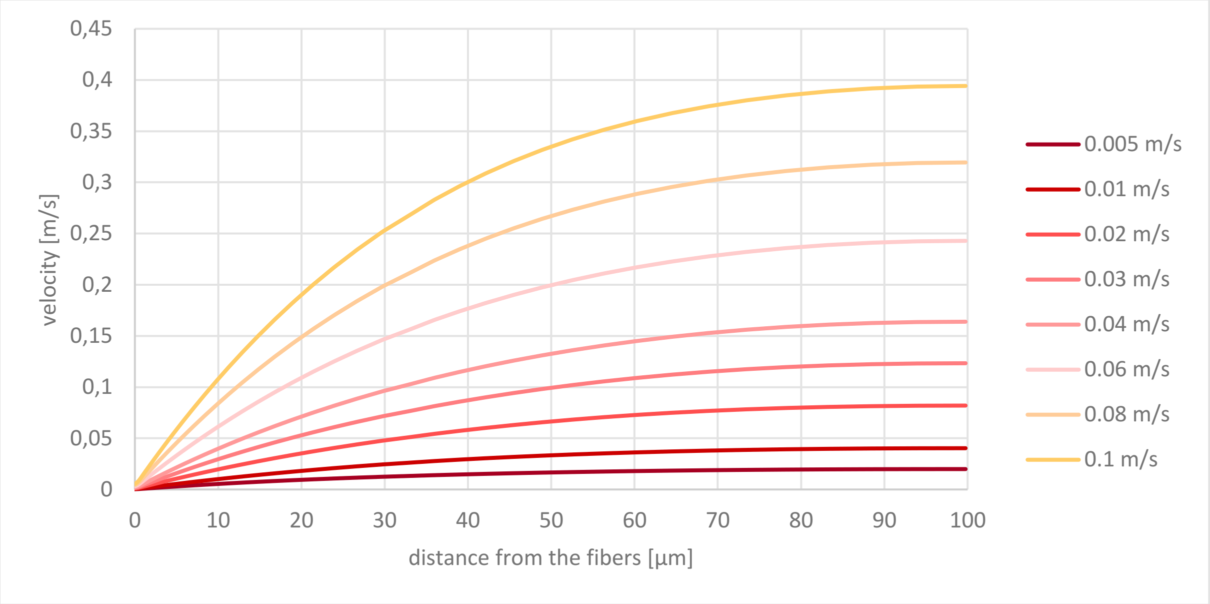

Figure 29: Velocity profiles at different inlet velocities for blood.

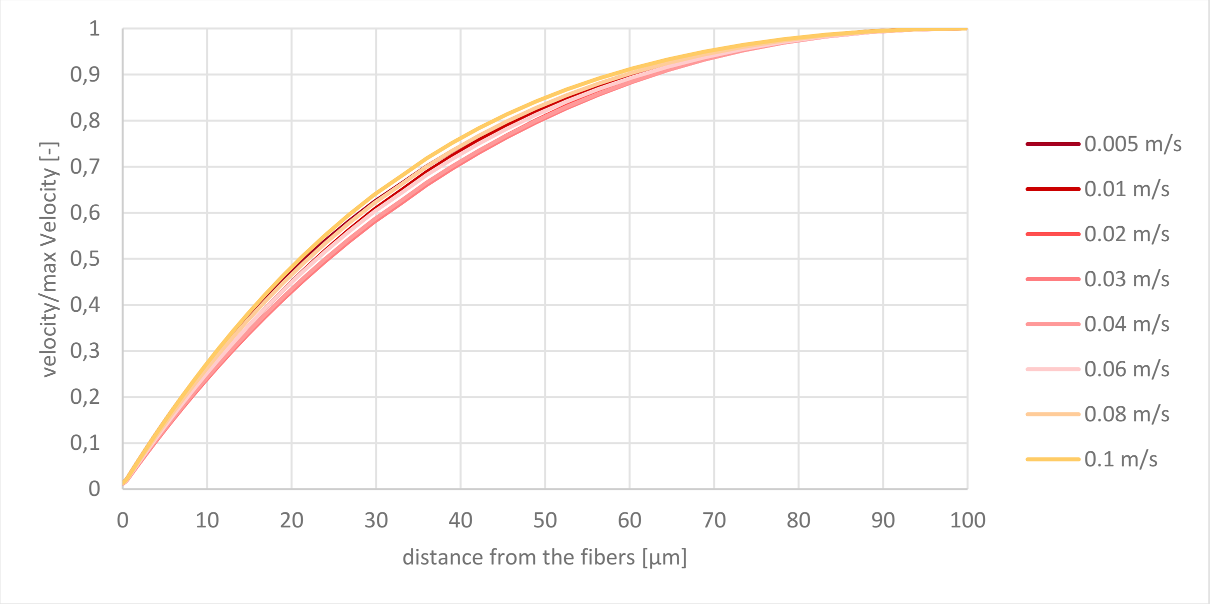

Figure 30: Dimensionless velocity profiles at different inlet velocities for blood.

This behavior is also seen in the results of the shear rate. Figure 31 shows the dimensional and Figure 32 the dimensionless shear rate profiles. The dimensionless shear rate was calculated by taking the highest shear rate near the fiber as a reference. The further away from the fiber the more the shear rate decreases. A short rise is seen at about a third of the distance from the fibers. The dimensionless share rates are comparable at different inlet velocities.

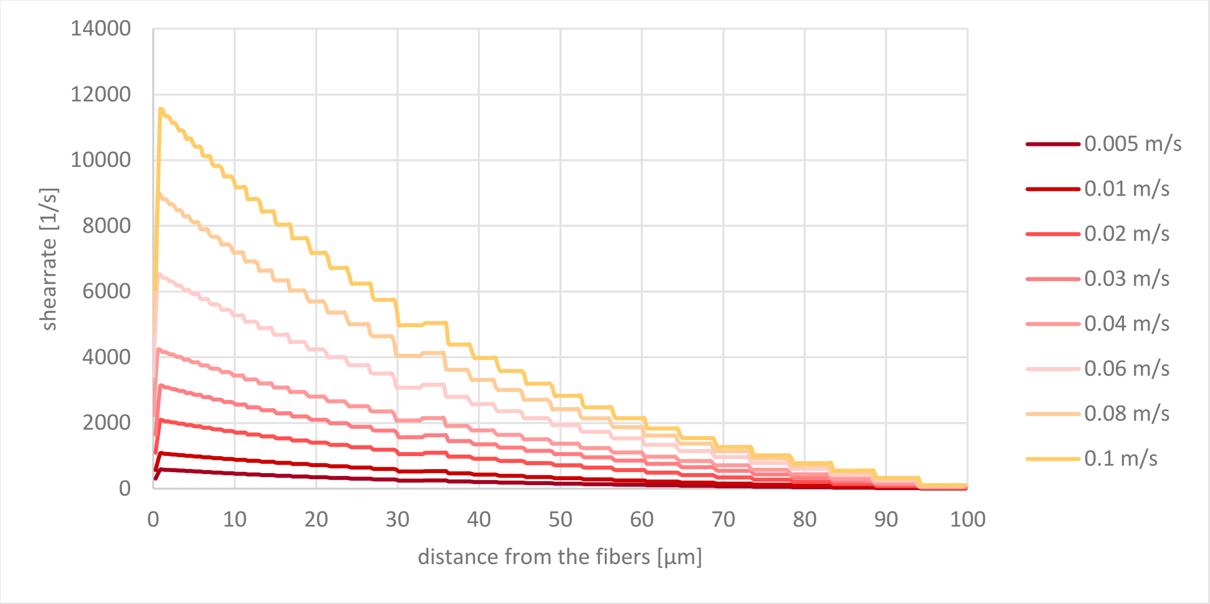

Figure 31: Shear rate profiles at different inlet velocities for blood.

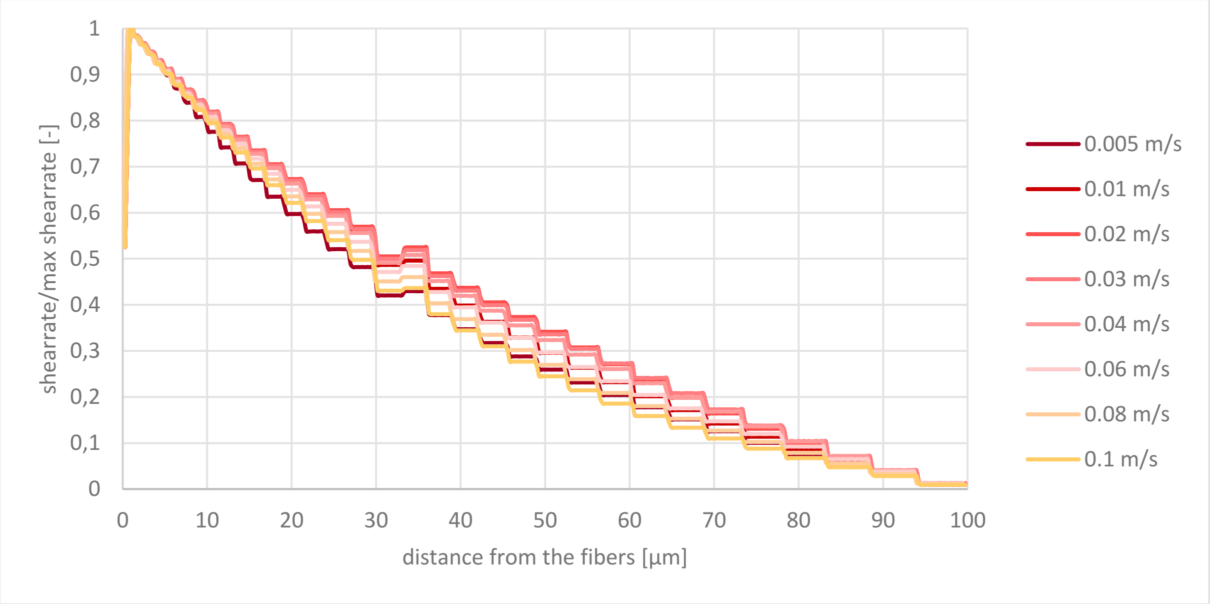

Figure 32: Dimensionless shear rate profiles at different inlet velocities for blood.

Absolute values of the partial pressure profiles of all velocities were not included as they are very similar to the dimensionless profile results. In Figure 33 the partial pressure profiles of all inlet partial pressure levels and 0.03 m/s inlet velocity are shown. This figure includes the corresponding dimensionless profiles. The partial pressure profiles behave differently at different partial pressure levels. The results for the dimensionless partial pressure boundary layer profiles at different partial pressure levels are shown in Figure 34, Figure 35 and Figure 36. The dimensionless partial pressure profile has its lowest values at the membrane, the highest are found at the outermost point. With increasing velocity, the dimensionless pCO₂ at the membrane increases. Furthermore, an increase in the gradient can be observed with increasing velocity. Comparing the profiles at different partial pressures, with increasing partial pressure the ratio of partial pressure to referenced partial pressure decreases. This is shown in Figure 37 for the 0.005 m/s inlet velocity.

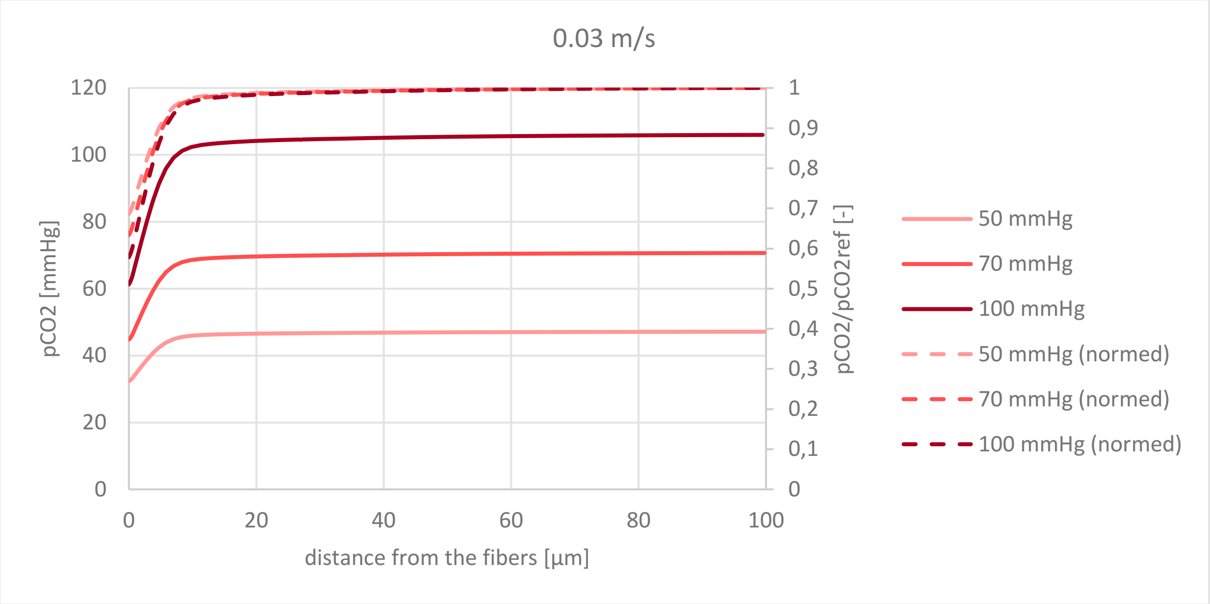

Figure 33: Partial pressure profiles at 0.03 m/s of blood and their corresponding dimensionless partial pressure profiles.

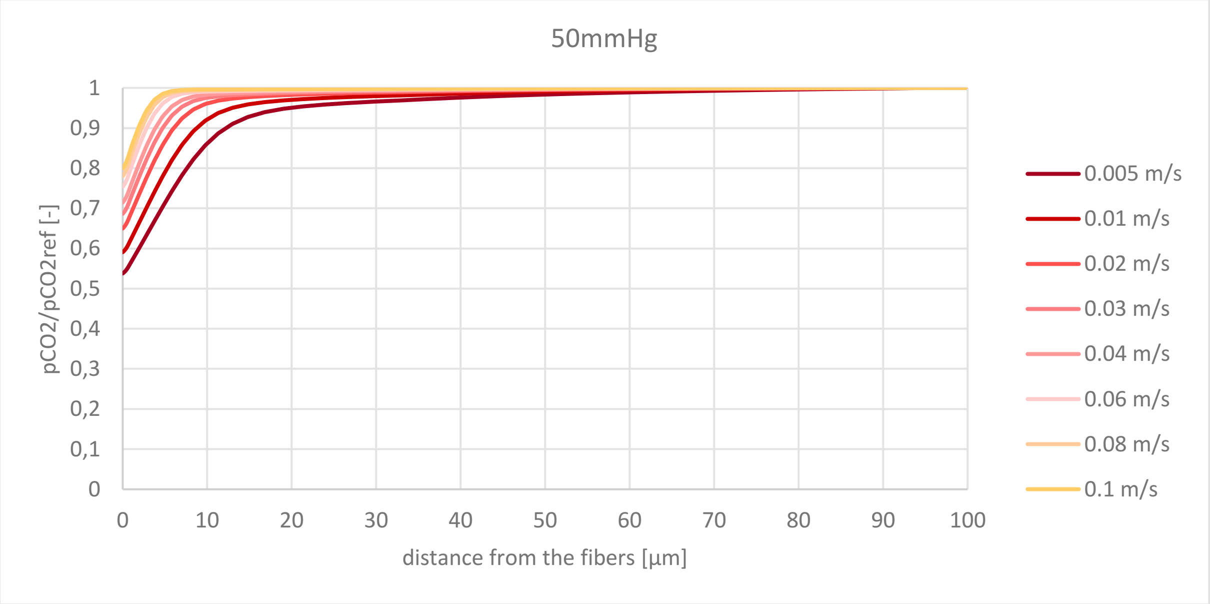

Figure 34: CO_2 partial pressure profiles of blood at 50 mmHg.

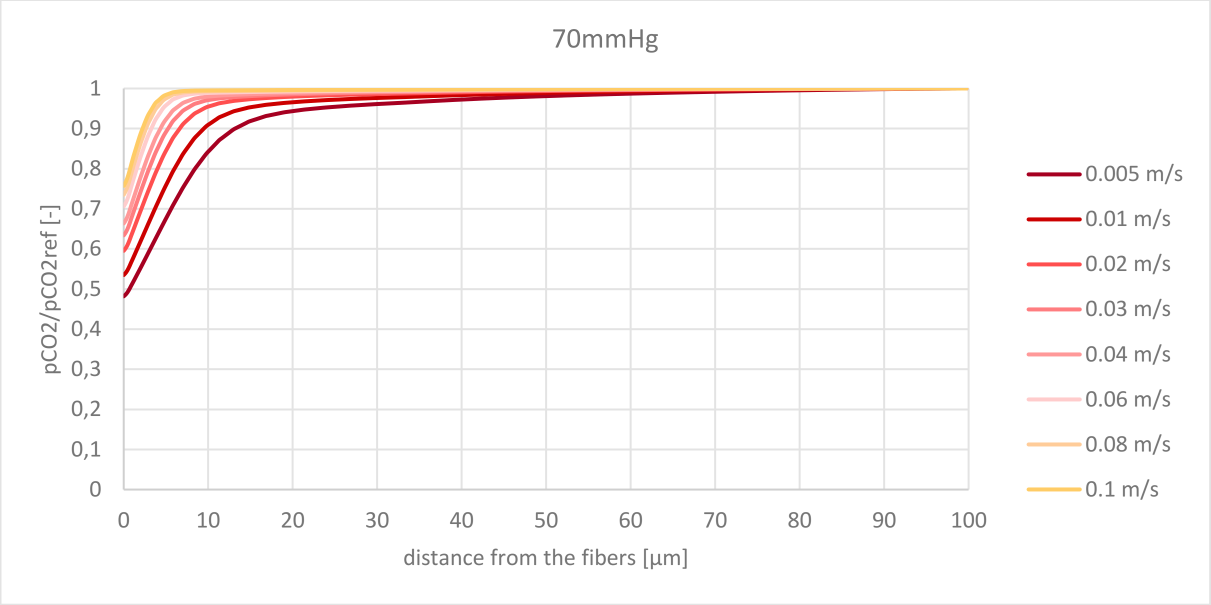

Figure 35: CO_2 partial pressure profiles of blood at 70 mmHg.

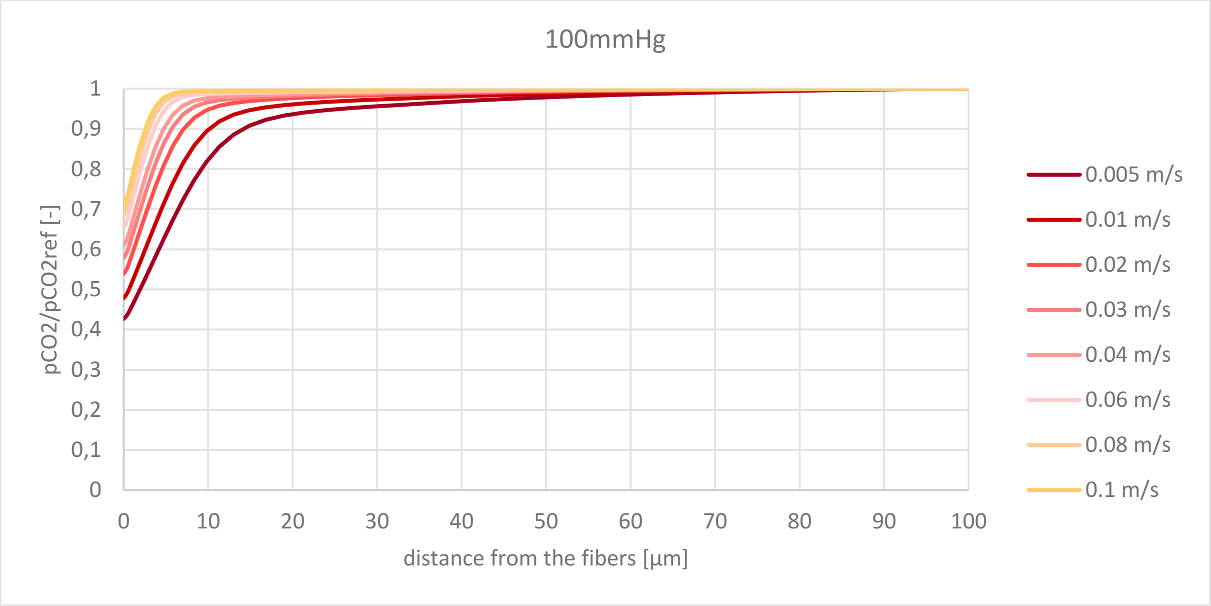

Figure 36: CO_2 partial pressure profile of blood at 100 mmHg.

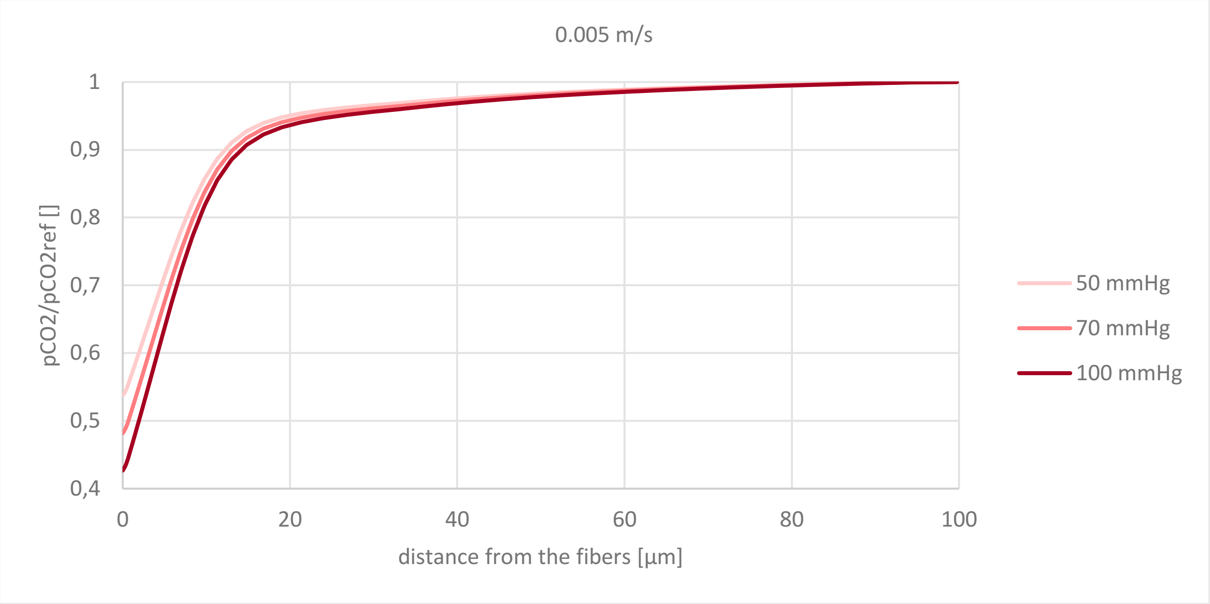

Figure 37: Comparison of dimensionless partial pressure blood profiles at different partial pressure levels for 0.005 m/s.

The concentration boundary layer length was calculated as described in chapter 3.3.5. In Figure 38 the results are presented. The x-axis shows the inlet velocity, and the y-axis represents the boundary layer length. The boundary layer length decreases with increasing inlet velocity. This is approximately logarithmic for all partial pressures. The difference in boundary layer length between the partial pressures increases comparing 50 to 100 mmHg until 0.06 m/s, where the deviation has its maximum. Deviation between 70 to 100 mmHg has its maximum at 0.08 m/s and for 50 to 70 mmHg it is at 0.06 m/s. In general, the concentration boundary layer decreases faster, up to about 0.06 m/s, at lower CO_2 partial pressure levels. In Figure 38 the deviations between partial pressure levels can be seen.

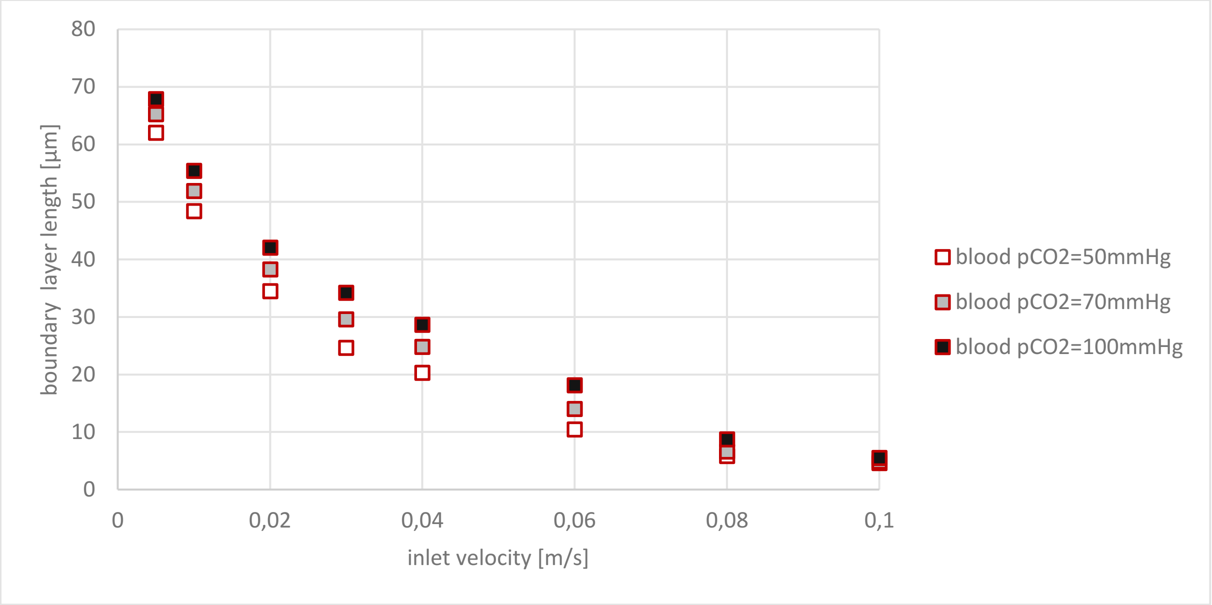

Figure 38: Partial pressure boundary layer thickness at different inlet velocities for blood.

Table 9: Deviation of boundary layer thickness between blood and water at different CO_2 partial pressure levels.

	boundary layer deviations between diffrent partial pressure levels [%]		
velocity[m/s]	**50/70**	**70/100**	**50/100**
0.005	4.89	3.85	8.55
0.01	6.70	6.28	12.57
0.02	9.85	8.97	17.93
0.03	16.67	13.56	27.97
0.04	17.98	13.42	28.99
0.06	25.32	22.60	42.20
0.08	12.02	24.07	33.20
0.1	5.88	10.53	15.79

4.7.2 Water

The dimensionless profiles were calculated analogous to blood. Figure 39 shows the dimensional velocity and Figure 40 the dimensionless velocity. With increasing inlet velocity, the slope of the velocity profile increases. This is true for the dimensionless and dimensional case. Figure 40 shows that with different inlet velocities different velocity profiles are created. With higher inlet velocity the velocity boundary layer length decreases.

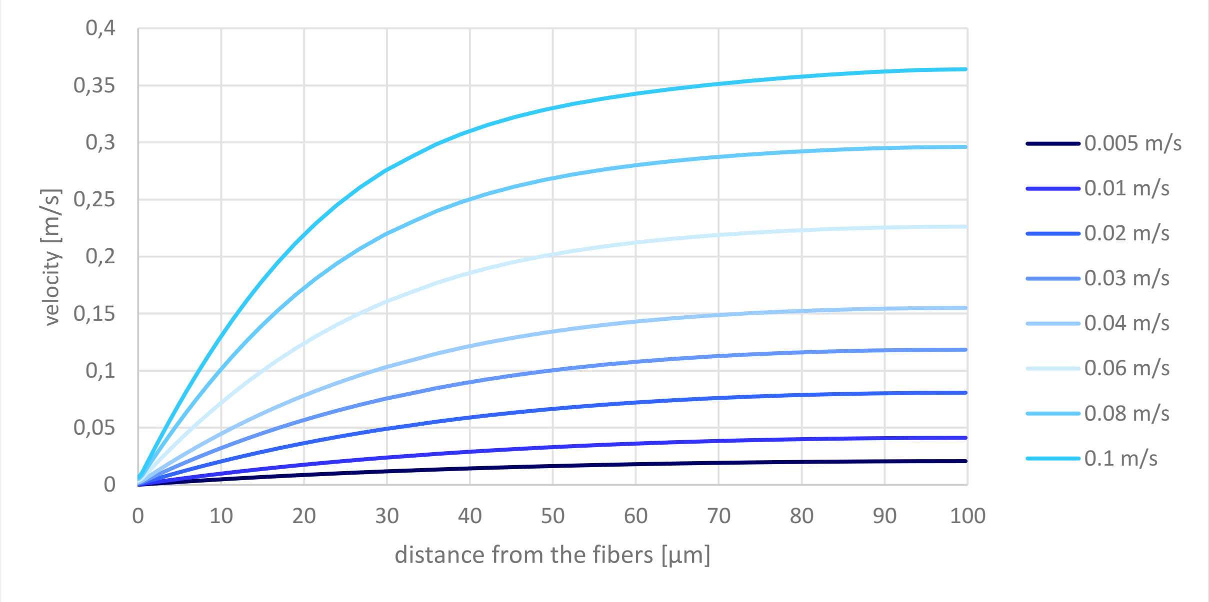

Figure 39: Velocity profiles at different inlet velocities for water.

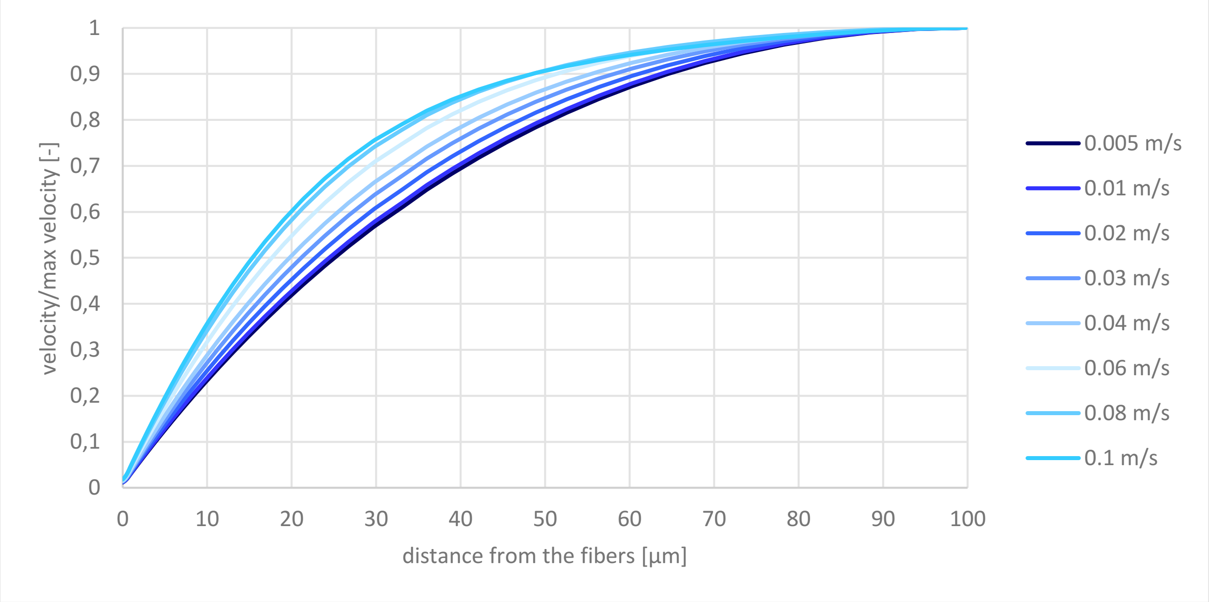

Figure 40: Dimensionless velocity profiles at different inlet velocities for water.

The results for the shear rate can be seen in Figure 41 and Figure 42, where Figure 41 shows the dimensional and Figure 42 the dimensionless shear rate. The maximum shear rate increases with increasing speed. At about a third of the distance from the fibers it is noticeable that the shear rate increases shortly. Furthermore, the shear rate gradient decreases more with increasing inlet velocity. The dimensionless shear rate profiles are not comparable at different velocities for water.

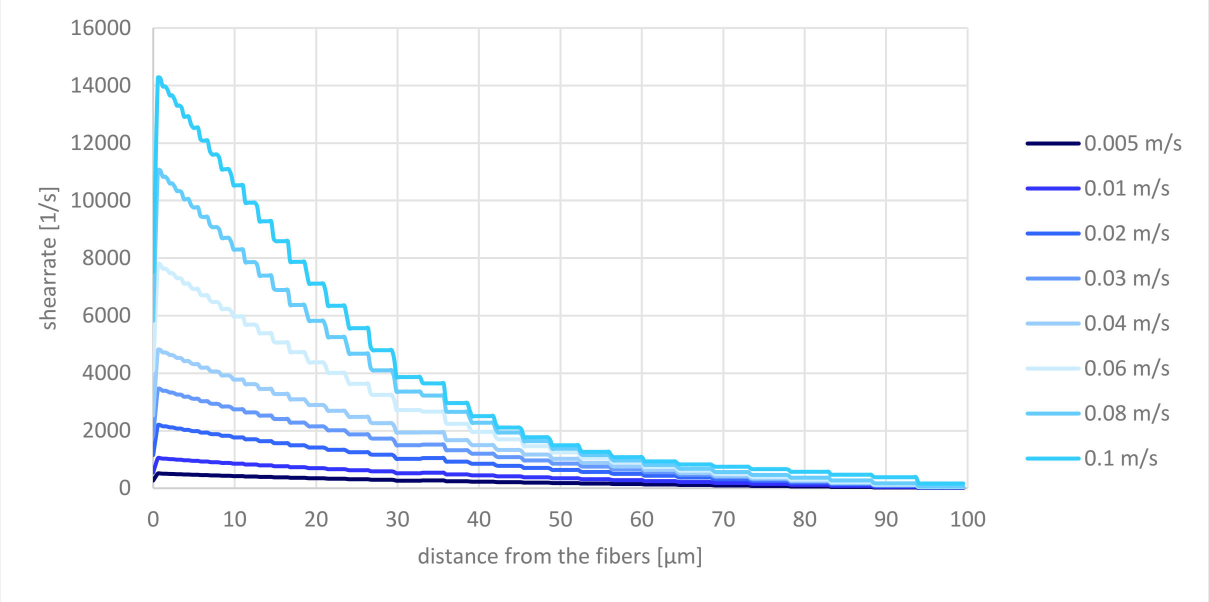

Figure 41: Shear rate profiles at different inlet velocities for water.

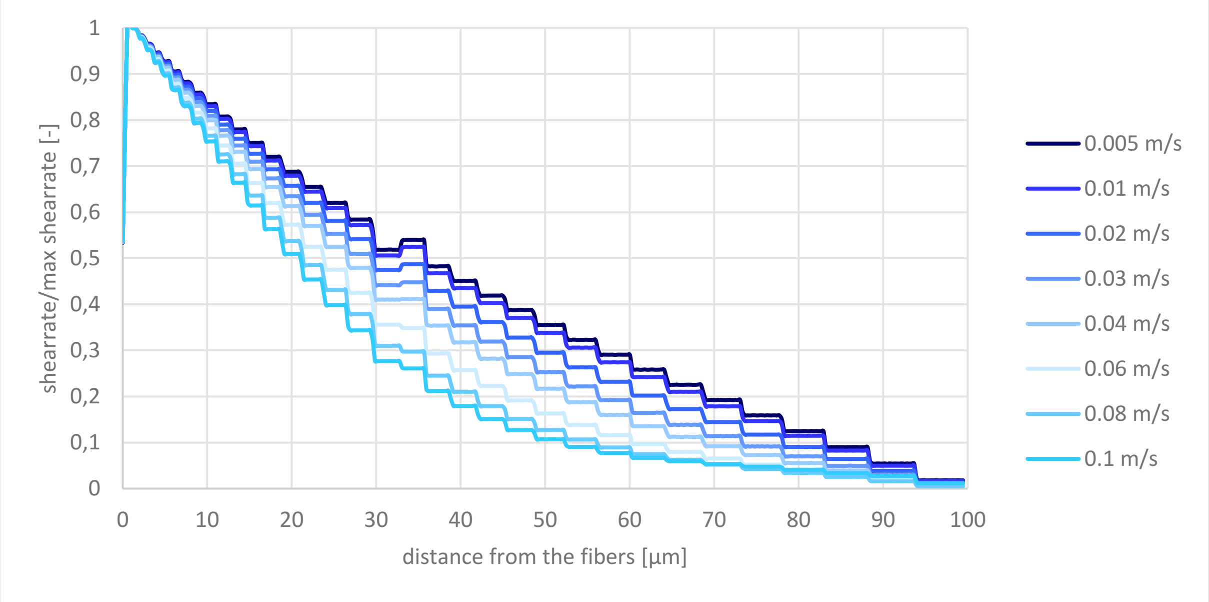

Figure 42: Dimensionless shear rate profiles at different inlet velocities for water.

The CO_2 partial pressure profile of water can be seen in Figure 43. The partial pressure level has no influence on the dimensionless concentration boundary layer, therefore the results shown are valid for all partial pressures studied. This can be seen in Figure 44. The lowest partial pressure values are found near the membrane, and the values increase with increasing distance from the membrane. With increasing velocity, an increasing gradient can be seen, furthermore, the dimensionless partial pressure at the membrane increases.

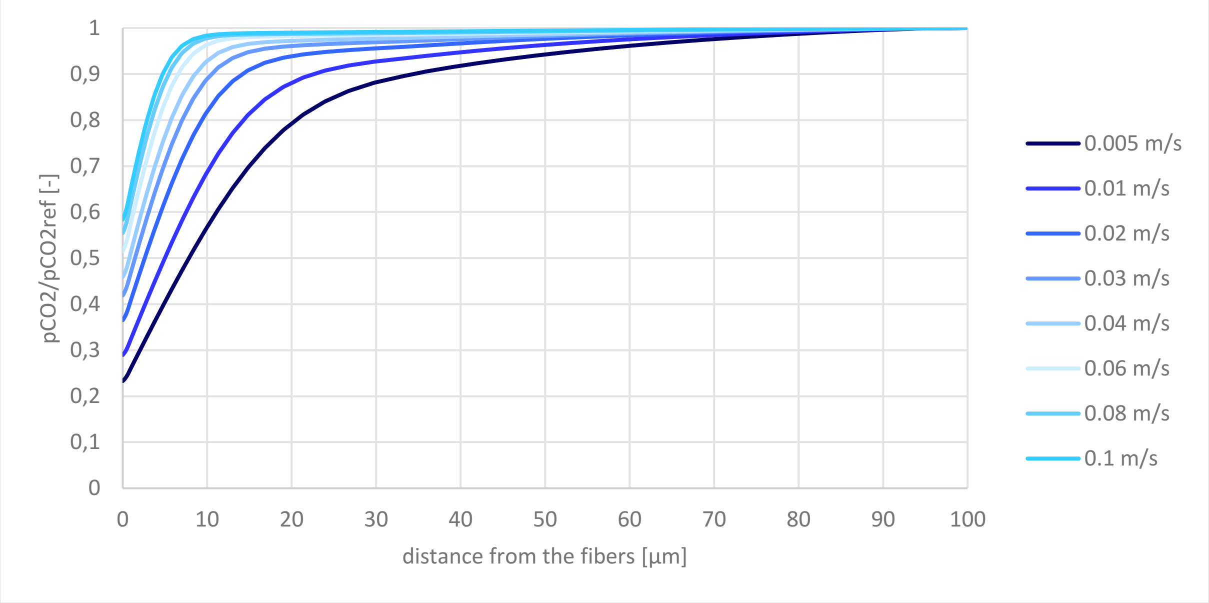

Figure 43: Dimensionless CO_2 partial pressure boundary layer profiles of water.

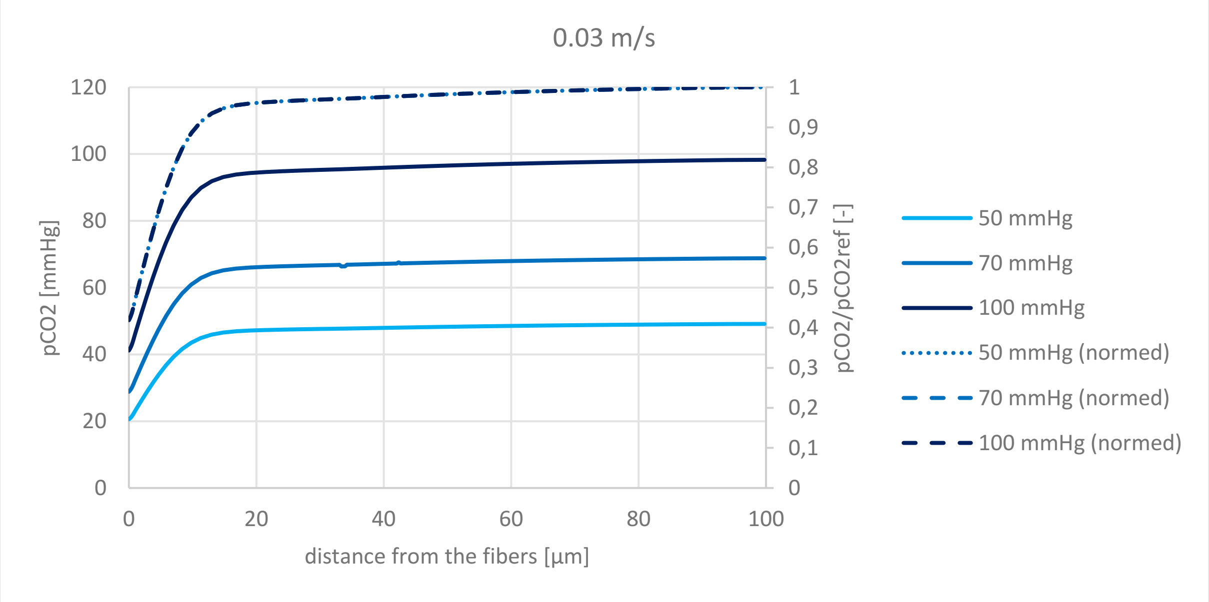

Figure 44: Partial pressure profiles at 0.03 m/s of water and their corresponding dimensionless CO_2 partial pressure profiles.

The results of the partial pressure boundary layer thickness are shown in Figure 45. In contrast to blood, the CO_2 partial pressure boundary layer thickness does not change with the partial pressure. With increasing velocity, the boundary layer length decreases approximately linearly.

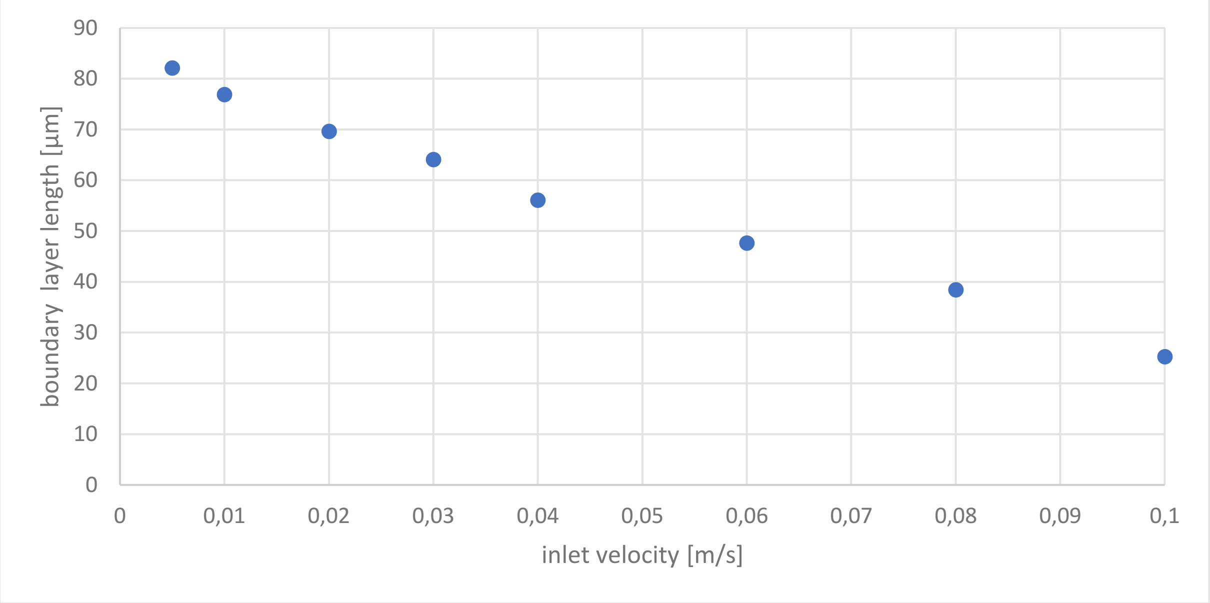

Figure 45: CO_2 partial pressure boundary layer thickness at different inlet velocities for water.

4.7.3 Comparison of blood and water

In the following chapter the results of the internal flow of the CFD simulation of water and blood are compared. The presented results are calculated in the same way as described in the previous chapters. In Figure 46 the comparison of the velocity profile is shown, and the dimensionless comparison can be found in Figure 47 (excluding some velocities to increase clarity of the figure). The fluids behave differently, at low inlet velocities < 0.03 m/s, blood shows a stronger increase in velocity. Beginning with 0.03 m/s this switches and the water velocity gradient is stronger over the distance from the fibers. Furthermore, with increasing inlet velocity the ratio of max velocity to inlet velocity, of water decreases. For blood it remains approximately constant. The dimensionless velocity profile in Figure 47 shows that the fluids are comparable for low velocities, especially for an inlet velocity range of 0.01-0.03 m/s. At inlet velocity of 0.02 m/s velocity profiles of blood and water show the closest similarity. At higher inlet velocities, an increased deviation can be seen. However, also with further decreased inlet velocities (< 0.01 m/s) the velocity profiles would deviate increasingly.

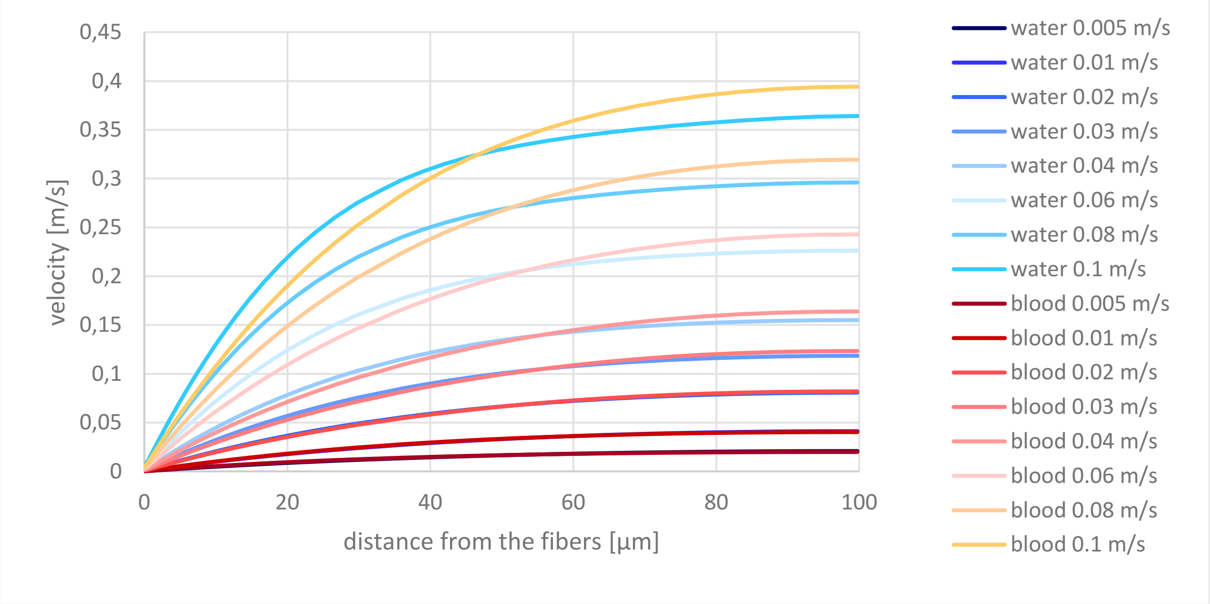

Figure 46: Comparison of blood and water velocity profiles.

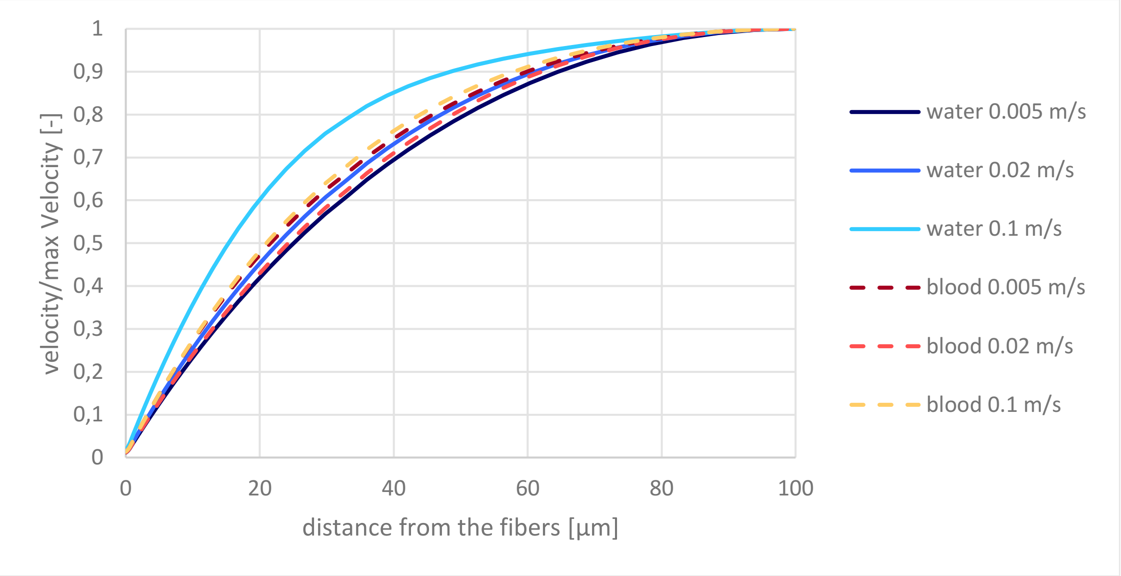

Figure 47: Comparison of dimensionless blood and water velocity profiles.

Since the shear rate is directly derived from the velocity over the distance from the fibers, it behaves like the velocity profiles. The dimensionless shear rate profiles can be seen in Figure 48. At low velocities, below 0.3 m/s, water represents the blood shear rate profiles adequately. Both fluids have a small local maximum in shear rate at about one third of the distance of the fibers. Comparison of maxima shear rate can be seen in Table 10. The inlet velocity 0.02 m/s shows the smallest deviation between blood and water.

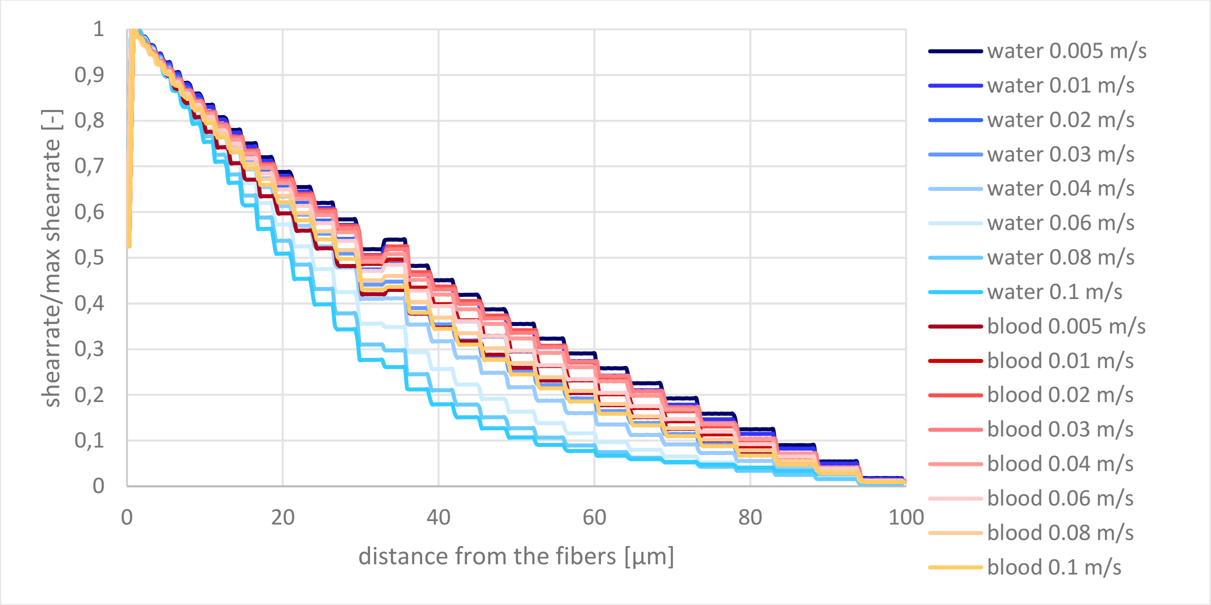

Figure 48: Comparison of dimensionless shear rate profiles between blood and water.

Table 10: Comparison of maximum shear rates between blood and water at different inlet velocities.

max shear rate [1/s]	**0.005 m/s**	**0.01 m/s**	**0.02 m/s**	**0.03 m/s**	**0.04 m/s**	**0.06 m/s**	**0.08 m/s**	**0.1 m/s**
water	505	1029	2155	3390	4723	7638	10835	13974
blood	582	1075	2081	3132	4227	6527	8972	11551
deviation [%]	13.18	4.28	3.53	8.25	11.76	17.01	20.76	20.98

For the comparison of the concentration boundary layer profiles. Only one velocity (0.03 m/s) was compared due to clarity of presentation. The comparison of the pCO_2 profiles can be seen in Figure 49 and the dimensionless pCO_2 comparison is presented in Figure 50. Furthermore, in order to help distinguishing the plots, pCO_2 profiles are only shown for fiber distances ranging from 0 to 30 µm. The comparison is the same for different velocities. Partial pressure and the dimensionless partial pressure of water at the membrane is significantly lower than that of blood. Furthermore, is it noticeable that the partial pressure boundary layer thickness of blood is smaller than that of water. The steep rise shortly after the membrane is greater for water at 50 and 70 mmHg. At 100 mmHg they are similar and hard to differentiate. The lower pCO_2 at the membrane and the greater rise after the membrane from water is especially pronounced at small velocities.

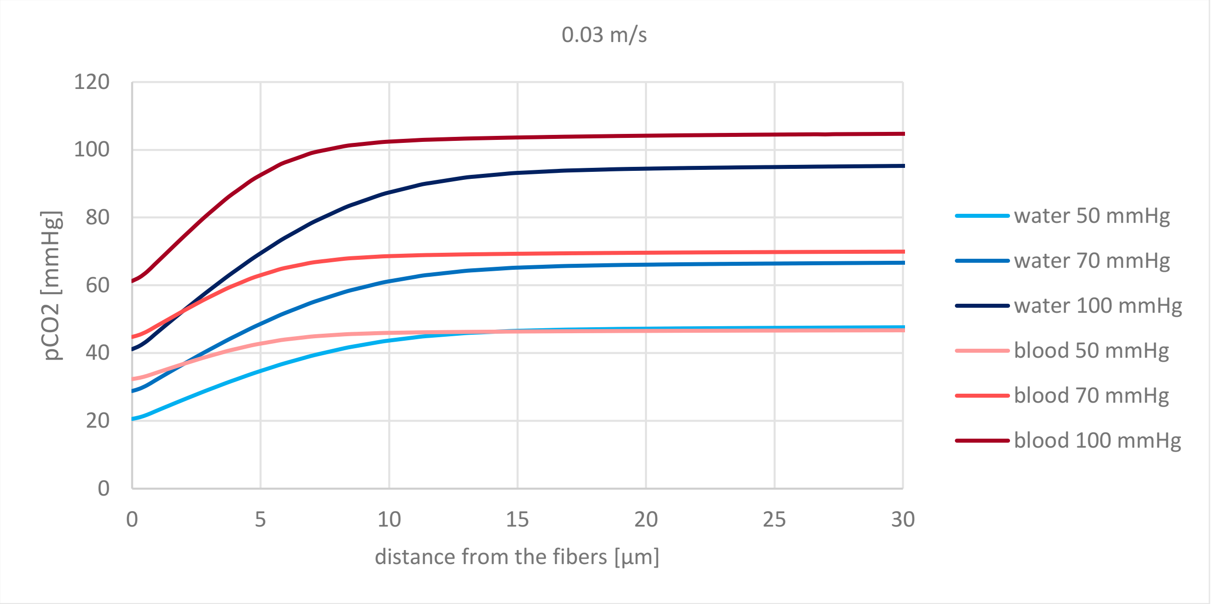

Figure 49: pCO_2 boundary layer profile comparison of blood and water at 0.03 m/s inlet velocity.

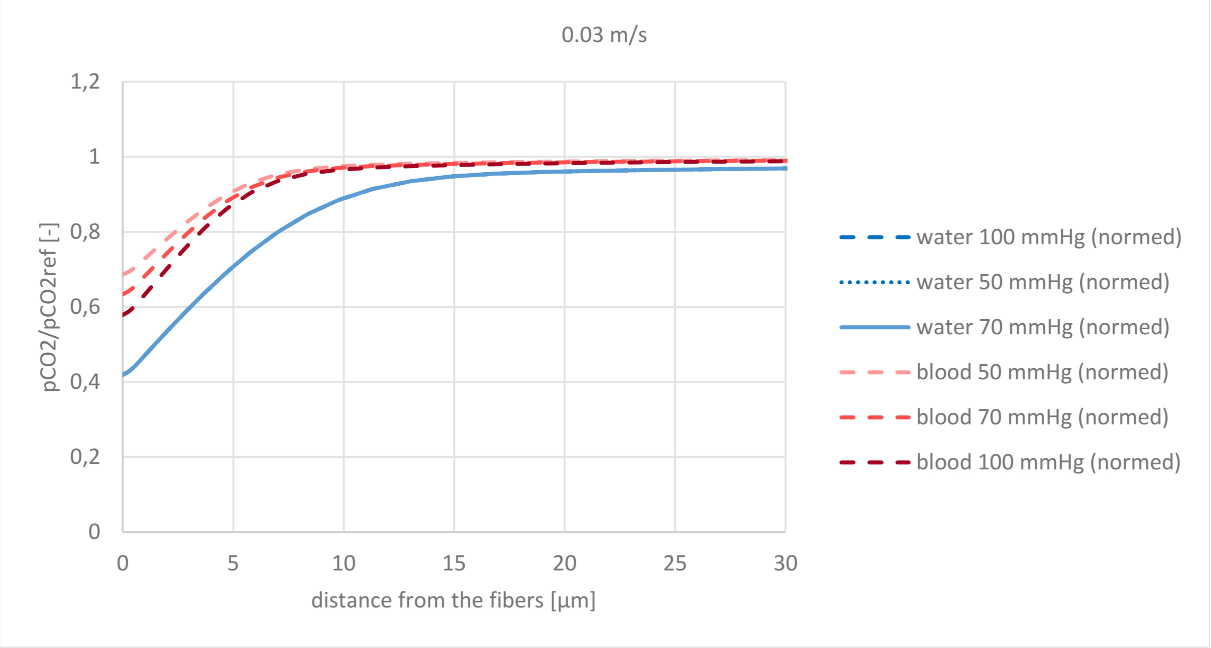

Figure 50: Dimensionless pCO2 boundary layer profile comparison of blood and water at 0.03 m/s inlet velocity.

Water does not represent the partial pressure boundary layer thickness of blood. With increasing velocity, the deviation increases. Furthermore, it increases with decreasing CO_2 partial pressure level. The highest deviation of the concentration boundary layer is found at the 50mmHg and 0.01 m/s, the lowest at 100 mmHg and 0.005 m/s. The differences are shown in Table 11. Because there is no dependency of boundary layer thickness of water from CO_2 partial pressure, the results are merged. The comparison of the concentration boundary lengths of water and blood are shown in Figure 51.

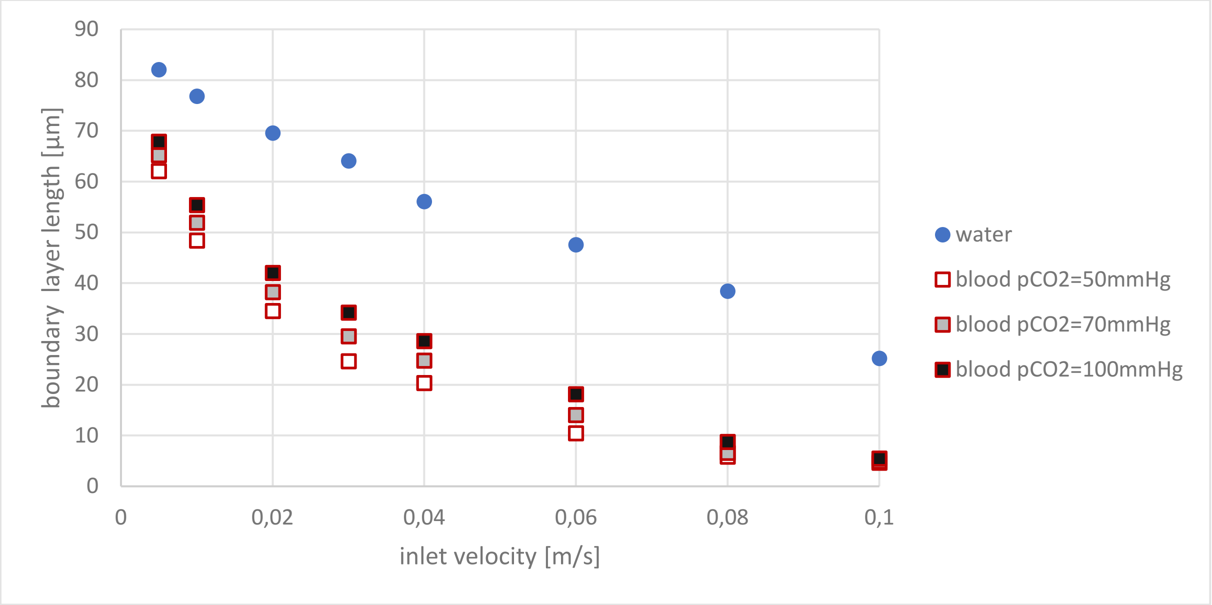

Figure 51: Comparison of boundary layer length of blood and water at different inlet velocities.

Table 11: Deviations of boundary layer thickness comparing blood to water.

velocity[m/s]	50mmHg	70mmHg	100mmHg
0.005	32 %	25 %	20 %
0.01	58 %	48 %	38 %
0.02	101 %	81 %	65 %
0.03	160 %	116 %	87 %
0.04	175 %	126 %	95 %
0.06	354 %	239 %	162 %
0.08	558 %	479 %	339 %
0.1	444 %	412 %	358 %

Since blood and water differ in viscosity it makes sense to apply the boundary length over the Reynolds number. For blood, the constant Newtonian viscosity was used. The results for this view are shown in Figure 52. The water and blood partial pressure boundary layers differ at similar Reynolds numbers more than at similar velocities. As the viscosity of blood is higher than that of water, the blood results are shifted to the left side of the graph. The results for water are shifted to the right because of the lower viscosity than for blood. This leads to low velocity results of water being compared to high velocity results of blood.

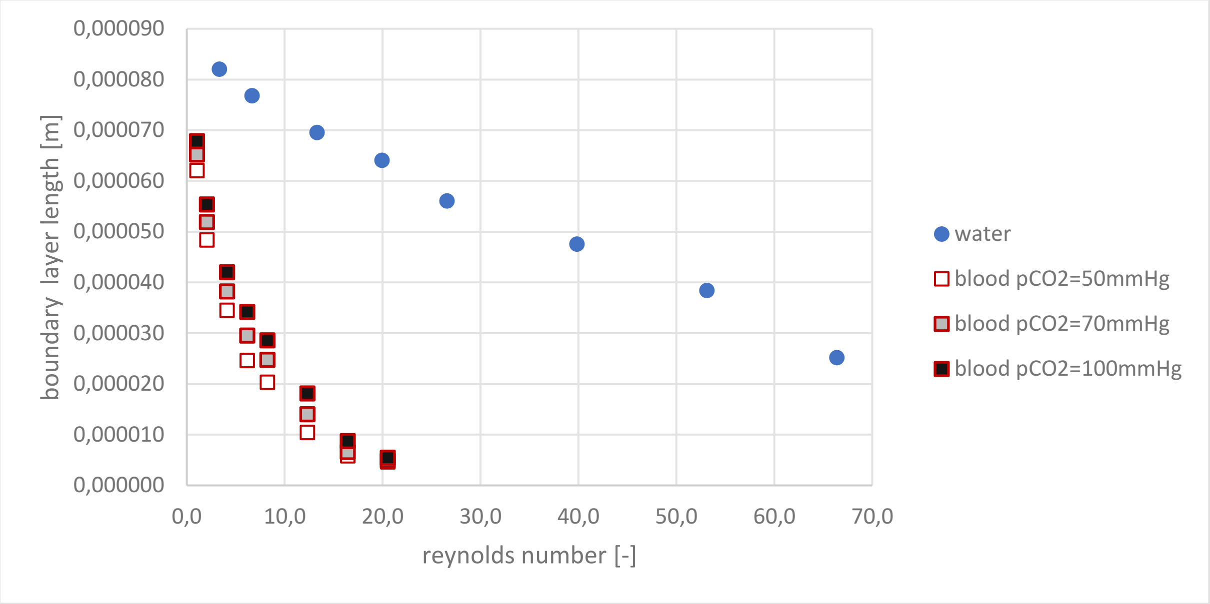

Figure 52: Comparison of the boundary layer thickness of blood and water in dependency of Reynolds number.

4.7.4 Dependency studies

A significant difference in the results is that for blood, the boundary layer thickness changes with partial pressure and for water, the boundary layer remains constant. Several simulations were carried out to determine where this difference comes from. Water simulation cases were modified for this purpose. A different blood-specific property was added to a water simulation case and then simulated at 50 and 100 mmHg. The partial pressure boundary layer was then calculated for each modification and partial pressure. This boundary layer dependency study was performed for 0.01 m/s. The blood-specific properties which were modified in the water simulations are CO_2 diffusion coefficient, the viscosity model, the CO_2 solubility model, and the CO_2 permeance. The result of this study can be seen in Figure 53. The boundary layer length is plotted on the y-axis. The individual columns indicate the different modifications of the simulation. Columns labelled “no model adapted” are the result of the water simulation without modification, results are the same for 50 mmHg and 100 mmHg. The results for blood without modification are the column labelled “as reference” for 50 mmHg and 100 mmHg. For the remaining columns, the grey columns are the results for 50 mmHg and the dark blue for 100 mmHg. Columns third from the left are results for the modified diffusion coefficient, which was changed from 2.38E-9 (water) to 4.6E-10 m2/s (blood). A change of about 5.1 times the coefficient leads to a reduction of 26 % of the boundary layer. In the columns third of the right the permeance of CO_2 through the membrane was changed from 275 GPU (water) to 157 GPU (blood). This reduces the boundary layer thickness by 11 %. The solubility model was converted from Henry to the dissociation curve of CO_2 in blood in the columns labelled "CO_2 solubility model". The dependence of the boundary layer length on the CO_2 partial pressure is induced by the solubility model. The columns labelled "viscosity model" have a changed viscosity, for which the power law model fitted by Lukitsch et al. (2020) was used. The change in viscosity leads to a 9 % shorter boundary layer length.

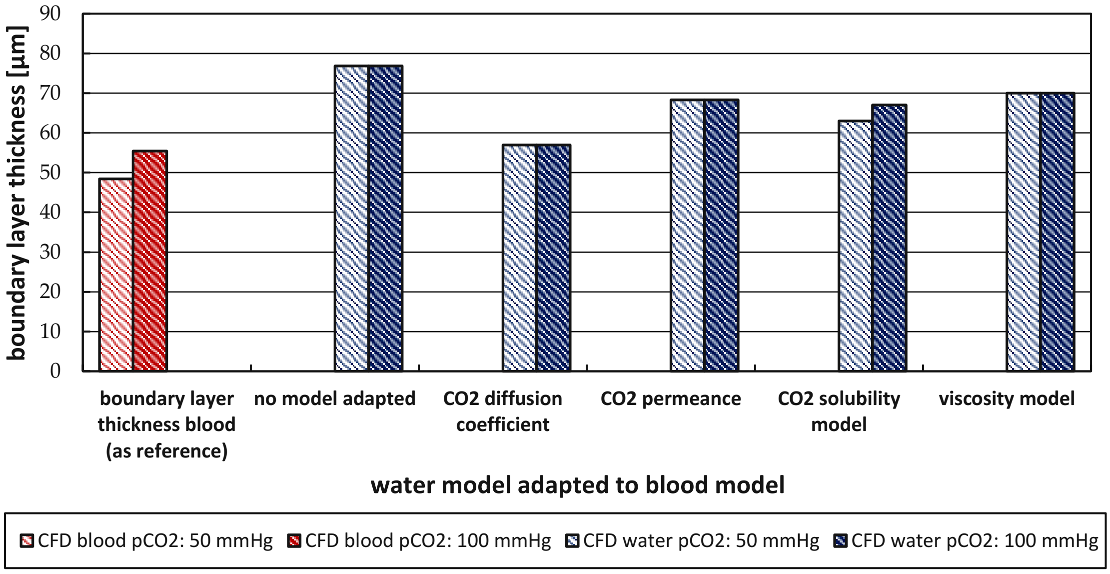

Figure 53: Influence of different blood specific attributes on the CO_2 partial pressure boundary layer, determined via modified water CFD simulations (0.01 m/s inlet velocity).(Lukitsch et al., 2021)

A similar study was performed a second time but with focus of the change of the CO_2 removal rate. Therefore, the second study modifications were only applied to the simulation case of 70 mmHg/ 1300 ml/min. The results of the dependency study of the CO_2 removal rate can be seen in Figure 54. Labelling is the same as in the boundary layer study graph, with the exception that the y axis represents the CO_2 removal rate. It can easily be seen that the solubility model has the biggest effect on the CO_2 removal rate and is the only parameter which increases the CO_2 removal rate. The change to the blood solubility model increased the removal rate by 120 %. All other modification led to a reduction in CO_2 removal rate. The change from the water CO_2 diffusion coefficient to the blood CO_2 diffusion coefficient leads to a decreased performance of 53 %. Adapting the membrane CO_2 permeance decreases the removal rate by 18 %. Changing the viscosity model has the least impact, the reduction is 10 %.

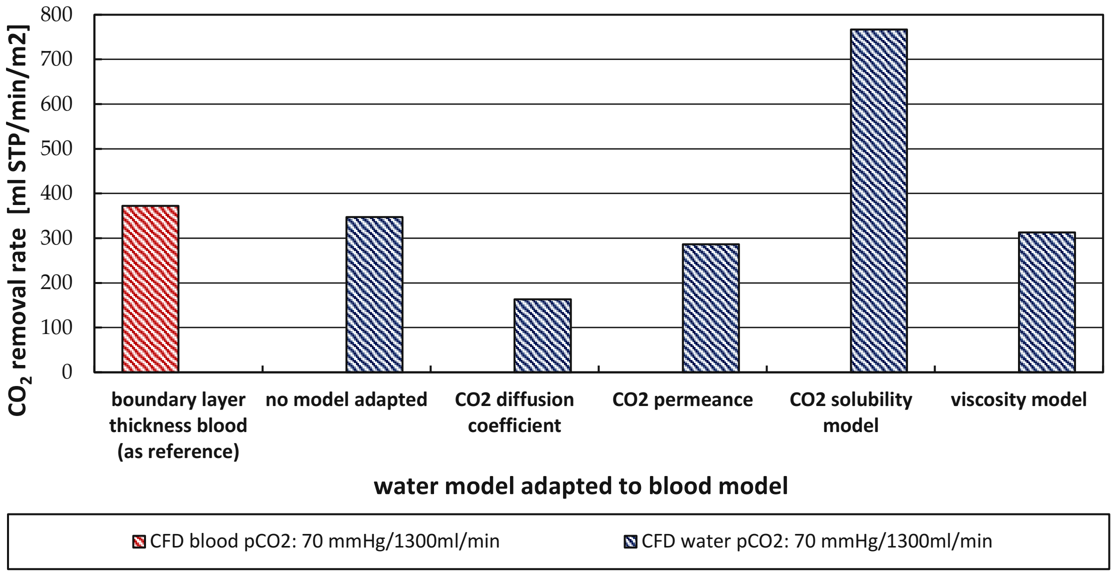

Figure 54: Influence of different blood specific attributes on CO_2 removal rate, determined via modified water CFD simulations (0.01 m/s inlet velocity).(Lukitsch et al., 2021)

4.8 Discussion of the boundary layer results

The discussion focuses on the comparability of water and blood. Of particular interest is whether water can model the internal flow of blood and if CO_2 removal rates are reasonably comparable (chapter 4.2). The velocity and shear rate profile of blood is best modelled at an inlet velocity of 0.02 m/s. At this velocity, the deviations of absolute values and profiles are small and water models blood satisfactorily. The deviation increases for both profiles deviating from this velocity. At high velocities, larger than 0.04 m/s, the absolute values and the profiles differ strongly. Typical blood oxygenator work at flow rates smaller than 2000 ml/min. The presented prototype is designed for flows between 1000-1600 ml/min, at which experiments were conducted. These flow rates have representative velocities between 0.015-0.031 m/s, at which the velocity profiles and shear rates of water and blood are comparable. However, concentration polarization layer thickness of blood and water is not comparable. In general, water has thicker layers, with smaller deviations in boundary layer thickness from blood at low velocities and high CO_2 partial pressures. Higher deviations were recorded at high velocities and low partial pressure. Furthermore, the boundary layer of water has no dependence on the CO_2 partial pressure. For blood, the boundary layer thickness is dependent on partial pressure. Based on follow up simulation's dependence of the boundary layer thickness on CO_2 partial pressure can be assigned to the nonlinear dissociation curve of CO_2 in blood. In addition, diffusivity, viscosity, membrane permeability and solubility of blood cause a smaller boundary layer compared to water.

Furthermore, dependence of the CO_2 removal rate on different blood-attributes was studied. The CO_2 solubility model of blood has a high impact on the removal rate. Simulations of water with the blood solubility model, lead to an almost twice as high removal rate. While the blood diffusion, viscosity, and membrane permeance lower the CO_2 removal rate when included in a water simulation. In summary, the comparable CO_2 removal rates of blood and water are achieved by the opposing effects of the properties of blood.

The results show that water predicts the CO_2 removal rate of blood satisfying. For the presented oxygenator, water is recommended as a blood substitute for the determination of the CO_2 removal rate. This recommendation is limited to the flow rates between 1000-1600 ml/min and CO_2 partial pressures between 50-100 mmHg. While it was not studied how a changed prototype geometry would impact the prediction rate, literature (Introduction) indicates a wide prediction capability of water for the CO_2 removal performance of oxygenators. While water shows good results for the removal rate, the boundary layer and velocity profiles of porcine blood and water behave different. Prediction capability in this regard is limited. Therefore, experimental research regarding the CO_2 concentration boundary layer, should be conducted with blood.

4.9 Sherwood correlation results

In contrast to direct comparison of CO_2 removal rates, Federspiel et al. propose a method using Sherwood correlations to determine the mass transfer coefficients of blood based on water experiments. This method was adapted for the prototype blood oxygenator and compared with the results of the blood experiments. Furthermore, the limitations and range of this method were discussed.

The results of the dimensionless numbers can be seen in Figure 55, Figure 56 and Figure 57. For the calculation of the dimensionless numbers, the individual results for the CO_2 removal rate of different flow rates and partial pressures were used. The data was modified so that the inlet partial pressure did not differ too much from 50, 70 and 100 mmHg, respectively. All experimental results with a deviation greater than 5 mmHg were discarded. The modified data was divided into the three partial pressure levels, as otherwise the coefficient of determination would have been too low. The calculation for the dimensionless numbers (Sh, Sc and Re) is different for water and blood and was carried out as described in Chapter 3.4, with the exception for the characteristic diameter. It was found that using the fiber diameter leads to better prediction results compared to the hydraulic diameter. In the result diagrams, the y axis describes the ratio of Sherwood to Schmidt to the power of 1/3. The Reynolds number is plotted on the x axis. Markings colored blue indicate the water results, blood results are colored red. The dotted lines in the graphs describe the power trend line, which was formed using Excel. The geometry parameters can be calculated from these trend line. Here a is the multiplier and b the exponent. The geometry parameters and the deviation of blood to water can be found in Table 12. The coefficient of determination can be found labelled as R^2 in the graphs. For inlet pCO_2 of 50 mmHg, the trend lines of water and blood show similarity only for the geometry parameter a, which deviates by 8 %. The parameter b deviates by 135 %. The two trend lines cross at Reynolds number 1 at a value of Sherwood divided by Schmidt to the power of three of approx. 1. A high deviation can be seen at higher Reynolds numbers.

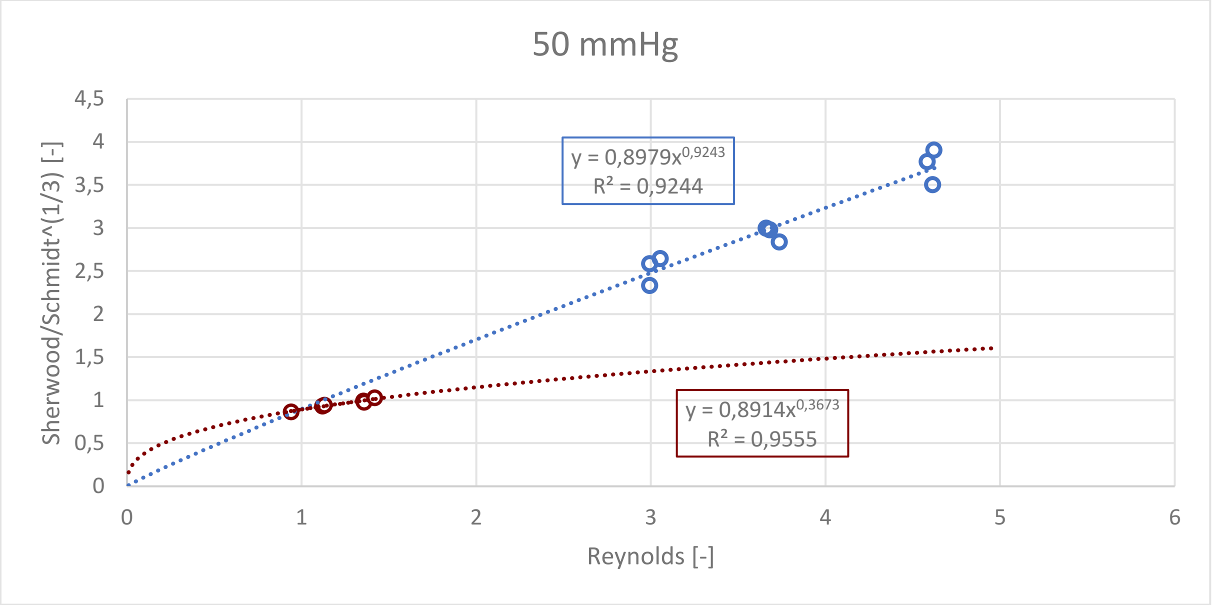

Figure 55: Sherwood correlation results for 50 mmHg.

The trend lines for inlet pCO_2 70 mmHg behave similarly to those for inlet pCO_2 50 mmHg. They cross at approximately the same point as at inlet pCO_2 50 mmHg. For water, parameter a increases, and parameter b decreases. The parameters show similar dependencies for blood. The deviation is 12 % for the a parameter and 121 % for the b parameter.

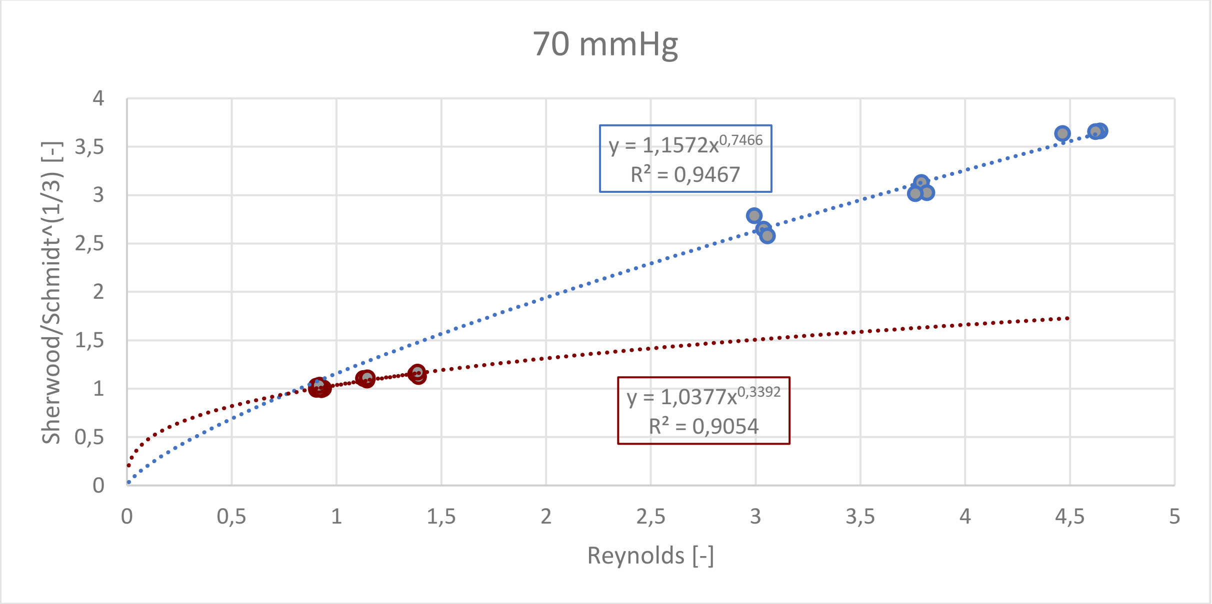

Figure 56: Sherwood correlation results for 70 mmHg.

At 100 mmHg the trend lines cross near 0/0. Furthermore, for blood both geometry factors increase, while for water a increases and b decreases. The deviation of water to blood for the a parameter is 37 % and for b 9 %.

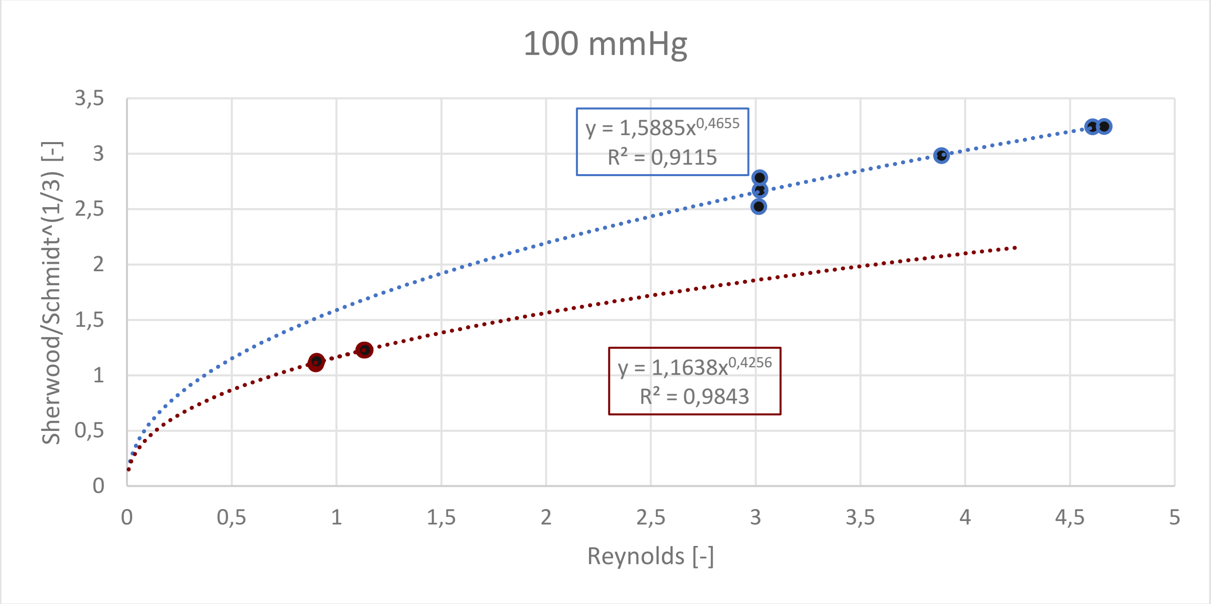

Figure 57: Sherwood correlation results for 100 mmHg.

Table 12: Sherwood correlation geometry parameters of blood and water, and their deviations from each other.

	inlet partial pressure [mmHg]	a [-]	b [-]
blood	50	0.89	0.37
	70	1.04	0.34
	100	1.16	0.43
water	50	0.96	0.87
	70	1.16	0.75
	100	1.59	0.47
deviations [%]	50	8	135
	70	12	121
	100	37	9

CO_2 removal prediction for blood calculated using the water geometry parameters can be found in Table 13. The calculations of the removal rate with the water geometry parameters lead to an average deviation of 22 %. Smaller deviations can be found at the inlet pCO_2 level of 70 mmHg and bigger deviations at inlet pCO_2 level 100 mmHg. At inlet

pCO_2 70 mmHg and flow rates of 1000 ml/min the smallest deviation of 3.6 % can be found. The largest deviation is recorded at inlet pCO_2 100 mmHg and flow rates of 1000 ml/min with 37.2 %. An improvement of the prediction capability in comparison to direct take-over of the experimental water CO_2 removal rates is only seen for 2 points. These are at inlet pCO_2 70 mmHg/ flow rate 1000mL/min and inlet pCO_2 50 mmHg/ flow rate1000mL/min.

Table 13: Results of the Sherwood model conversion from water to blood and the deviations to the experimental results.

inlet partial pressure [mmHg]	Q [ml/min]	J calculated for blood [ml/min*m^2]	J experimental blood [ml/min*m^2]	deviation [%]	J water experimental	deviation blood to water experiments
50	1000	255.9	287.5	11.0	224.8	21.8
50	1300	321.7	285.6	12.6	257.2	9.9
50	1600	385.5	296.6	30.0	290.4	2.1
70	1000	367.2	354.6	3.6	324.1	8.6
70	1300	447.1	392.2	14.0	350.6	10.6
70	1600	522.6	427.8	22.2	393.8	7.9
100	1000	632.7	461.2	37.2	419.3	9.1
100	1300	714.6	530.5	34.7	494.9	6.7
100	1600	786.6	601.9	30.7	543.9	9.6

4.10 Discussion of the Sherwood model results

While Federspiel et al. achieved good results with their prediction method, their method did not work well for the presented prototype. The method proposed by Federspiel shows an average deviation of 22 % for the removal rate, while the water experiments deviate only 9.6 % from the blood results.

A faulty prediction calculation was thought to have occurred, so calculations were also made with the blood factor parameters. The Sherwood model with the blood parameters lead to an average deviation of the CO_2 removal rate of 3.4%.

The partial pressure level with the most similar geometry factors between blood and water has the worst prediction results. This is because the blood Reynolds numbers have values of approx. one. Consequently, the geometry factor b as an exponent of Re has only a small impact. This increases sensitivity of factor a. For partial pressure levels of 50 and 70 mmHg the a parameter of water has an averaged deviation of 10 % from the blood a parameter. At 100 mmHg the a parameter deviation is 37 %. This is reflected in the prediction results of the Sherwood model, as the predictions at 50 and 70 mmHg are better than at 100 mmHg. But if predictions were needed at higher Reynolds numbers and therefore making the b parameter relevant again, 100 mmHg would obtain better prediction results. Concluding that the prediction results of 50 and 70 mmHg via the Sherwood model cannot fully be trusted, as their accuracy is only given at low Re numbers. Concluding that the experimental results of the CO_2 removal rates with water model the blood CO_2 removal rate better than the method presented by Federspiel et al.

5 Conclusion

In the context of this master thesis, the comparability of water and blood with regard to CO_2 removal was investigated in a hollow fiber membrane module prototype. The prototype was developed in-house. Several methods were used to analyze the comparability.

First, a comprehensive literature review on the use of water as a blood substitute was conducted. The literature review gives that water is a reasonable blood model for CO_2 removal, but the discourse on the comparability is missing.

CO_2 removal rates were compared between water and blood. Experimental data was used for this purpose. The experimental data shows CO_2 removal rates for water and blood for the same prototype oxygenator. Three flow rates (1000, 1300 and 1600 ml/min) were measured, each with three CO_2 partial pressures (50, 70 and 100 mmHg). The results show that water is an adequate blood model in the context of CO_2 removal in a blood oxygenator. However, further analysis is needed as to why blood and water have similar removal rates and to what extent water is suitable as a blood model.

Therefore, a series of CFD CO_2 transport simulations were performed. These were carried out using an in-house solver and an upscaling method. The previous experiments were used to validate the CFD simulations.

The good agreement of computational and experimental results allowed detailed studies of the boundary layer. CO_2 partial pressure boundary layer was studied for a range of inlet velocities and three levels of partial pressures (50, 70 and 100 mmHg). Shear rate, velocity and partial pressure profiles are compared between water and blood. Furthermore, the partial pressure boundary layer thicknesses were calculated and dependency studies on the CO_2 removal rate and the partial pressure boundary layer thickness were performed. The results show that the boundary layer of blood and water behave differently and cannot be compared. Therefore, it can be said that studies aimed at investigating the blood CO_2 boundary layer should be based on blood tests.

Another way to predict CO_2 removal rates are Sherwood models. A Sherwood model, presented by Federspiel et al., was adapted to the geometry of the prototypes. However, the model does not lead to satisfactory results for the prototype mentioned. The prediction of the CO_2 removal rate with the Sherwood model leads to worse results than using water CO_2 removal rates directly. Despite the bad prediction results the model leads to a categorization of the prototype by dimensionless metrics, which provides further insight into the difference between CO_2 removal rate in water and blood.

6 Outlook

Within the framework of this master's thesis, it was possible to determine how comparable the CO_2 removal from water in a hollow fiber module is to blood. The results show that water makes good predictions for the CO_2 removal rate of blood. However, this was only done for one specific prototype geometry. The influence of the module geometry was not considered and must be the aim of further studies. However, the literature presented suggests a reasonable suitability for water for adapted geometries.

Furthermore, there is no literature comparing the CO_2 partial pressure boundary layer between water and blood. Therefore, the gained boundary layer profiles cannot be compared to third party data. Therefore, future experimental studies with focus on the boundary layer would prove useful not only to further validate this work, but also to improve simulation models.

The results of the Sherwood model are unsatisfactory. In contrast to the findings of Federspiel, the geometry parameters of water and blood determined for the prototype device are not comparable. Here, additional experiments at wider ranges of Reynolds numbers would be helpful to further evaluate this method and assess its validity. With these experimental data, a more reliable determination of the geometric parameters could be conducted.

7 References

Baker, R.W., 2000. Membrane technology and applications, McGraw-Hill professional engineering. McGraw-Hill, New York.

Caretto, L.S., Gosman, A.D., Patankar, S.V., Spalding, D.B., 1973. Two calculation procedures for steady, three-dimensional flows with recirculation, in: Cabannes, H., Temam, R. (Eds.), Proceedings of the Third International Conference on Numerical Methods in Fluid Mechanics, Lecture Notes in Physics. Springer Berlin Heidelberg, Berlin, Heidelberg, pp. 60–68. https://doi.org/10.1007/BFb0112677

Federspiel, W., Henchir, K., 2008. Lung, Artificial: Basic Principles and Current Applications, in: Wnek, G., Bowlin, G. (Eds.), Encyclopedia of Biomaterials and Biomedical Engineering, Second Edition - Four Volume Set. CRC Press, pp. 1661–1672. https://doi.org/10.1201/b18990-161

Greenshields, C., 2019. OpenFOAM v7 User Guide: 4.6 Solution and algorithm control [WWW Document]. CFD Direct. URL https://cfd.direct/openfoam/user-guide/v7-fvsolution/ (accessed 3.16.21).

Haddadi, B., 2018. Membrane modeling using CFD_ Combined evaluation of mass transfer and geometrical influences in 1D and 3D. J. Membr. Sci. 11.

Harasek, M., Lukitsch, B., Ecker, P., Janeczek, C., Elenkov, M., Keck, T., Haddadi, B., Jordan, C., Krenn, C., Ullrich, R., Gfoehler, M., 2020. Fully resolved computational (CFD) and experimental analysis of pressure drop and blood gas transport in a hollow fiber membrane oxygenator module 6.

Hattler, B.G., Lund, L.W., Golob, J., Russian, H., Lann, M.F., Merrill, T.L., Frankowski, B., Federspiel, W.J., 2002. A respiratory gas exchange catheter: In vitro and in vivo tests in large animals. J. Thorac. Cardiovasc. Surg. 124, 520–530. https://doi.org/10.1067/mtc.2002.123811

Himmelblau, D.M., 1964. Diffusion of Dissolved Gases in Liquids. Chem. Rev. 64, 527–550. https://doi.org/10.1021/cr60231a002

Ho, W.S.W., Sirkar, K.K. (Eds.), 1992. Membrane Handbook. Springer US, Boston, MA. https://doi.org/10.1007/978-1-4615-3548-5

Hout, M.S., Hattler, B.G., Federspiel, W.J., 2000. Validation of a Model for Flow-Dependent Carbon Dioxide Exchange in Artificial Lungs. Artif. Organs 24, 114–118. https://doi.org/10.1046/j.1525-1594.2000.06465.x

J.A., L., Luft, U.C., Fletcher, E.R., 1983. Quantitative description of whole blood CO2 dissociation curve and Haldane effect. Respir. Physiol. 51, 167–181. https://doi.org/10.1016/0034-5687(83)90038-5

Jaffer, I.H., Reding, M.T., Key, N.S., Weitz, J.I., 2018. Hematologic Problems in the Surgical Patient, in: Hematology. Elsevier, pp. 2304-2312.e4. https://doi.org/10.1016/B978-0-323-35762-3.00159-1

Johnston, B.M., Johnston, P.R., Corney, S., Kilpatrick, D., 2004. Non-Newtonian blood flow in human right coronary arteries: steady state simulations. J. Biomech. 37, 709–720. https://doi.org/10.1016/j.jbiomech.2003.09.016

Kestin, J., Sengers, J.V., Kamgar-Parsi, B., Levelt Sengers, J.M.H., 1984. Thermophysical Properties of Fluid H2O. J. Phys. Chem. Ref. Data 13, 175–183.

Knoche, W., 1980. Chemical Reactions of CO2 in Water, in: Bauer, C., Gros, G., Bartels, H. (Eds.), Biophysics and Physiology of Carbon Dioxide. Springer Berlin Heidelberg, Berlin, Heidelberg, pp. 3–11.

Lawson, D., Holt, D., 2007. Insensible water loss from the Jostra Quadrox D oxygenator: an in vitro study. Perfusion 22, 407–410. https://doi.org/10.1177/0267659108091337

Lukitsch, B., Ecker, P., Elenkov, M., Janeczek, C., Haddadi, B., Jordan, C., Krenn, C., Ullrich, R., Gfoehler, M., Harasek, M., 2020. Computation of Global and Local Mass Transfer in Hollow Fiber Membrane Modules. Sustainability 12, 2207. https://doi.org/10.3390/su12062207

Lukitsch, B., Koller, R., Ecker, P., Elenkov, M., Janeczek, C., Haddadi, B., Jordan, C., Gfoehler, M., Harasek, M., 2021. Water as a Blood Model for Determination of CO2 Removal Performance of Membrane Oxygenators, to be published on 30.04.2021.

Marriott, J., Sørensen, E., 2003. A general approach to modelling membrane modules. Chem. Eng. Sci. 58, 4975–4990. https://doi.org/10.1016/j.ces.2003.07.005

Melin, T., Rautenbach, R., 2007. Membranverfahren: Grundlagen der Modul- und Anlagenauslegung, 3., aktualisierte und erw. Aufl. ed, Chemische Technik/Verfahrenstechnik. Springer, Berlin ; New York.

Pentair - Membrane separation allows passage based on particle size | X-Flow [WWW Document], 2021. URL https://xflow.pentair.com/en/spectrum/membrane-technology-in-general/membrane-separation (accessed 2.14.21).

Rackley, S.A., 2017. Membrane separation systems, in: Carbon Capture and Storage. Elsevier, pp. 187–225. https://doi.org/10.1016/B978-0-12-812041-5.00008-8

Sander, R., 2015. Compilation of Henry's law constants (version 4.0) for water as solvent. Atmospheric Chem. Phys. 15, 4399–4981. https://doi.org/10.5194/acp-15-4399-2015

Svitek, R.G., Federspiel, W.J., 2008a. A Mathematical Model to Predict CO2 Removal in Hollow Fiber Membrane Oxygenators. Ann. Biomed. Eng. 36, 992–1003. https://doi.org/10.1007/s10439-008-9482-3

Svitek, R.G., Federspiel, W.J., 2008b. A Mathematical Model to Predict CO2 Removal in Hollow Fiber Membrane Oxygenators. Ann. Biomed. Eng. 36, 992–1003. https://doi.org/10.1007/s10439-008-9482-3

Tabesh, H., Gholami, M.H., Torabi, D., Mottaghy, K., 2019. A pH-based experimental method for carbon dioxide exchange evaluation in cylindrical hollow fiber membrane oxygenators. Asia-Pac. J. Chem. Eng. 14. https://doi.org/10.1002/apj.2337

Versteeg, H.K., Malalasekera, W., 2007. An introduction to computational fluid dynamics: the finite volume method, 2nd ed. ed. Pearson Education Ltd, Harlow, England ; New York.

Wagner, W., Pruss, A., 2002. The IAPWS formulation 1995 for the thermodynamic properties of ordinary water substance for general and scientific use. J. Phys. Chem. Ref. Data 31, 387–535.

Wärme- und Stoffübertragung, 2009. . Springer Berlin Heidelberg, Berlin, Heidelberg. https://doi.org/10.1007/978-3-540-87689-2

Wolf Dynamics - Customer-driven flow solutions [WWW Document], 2021. URL http://www.wolfdynamics.com/index.php (accessed 3.16.21).

8 Appendix

8.1 Table of figures

8.2 List of tables